VOLCANIC FRAMEWORK, GEOCHRONOLOGY AND GEOCHEMICAL EVOLUTION OF THE EL DORADO GOLD DISTRICT, EL SALVADOR, CENTRAL AMERICA

by

MATHIEU RICHER

B.Sc. Honors, McGill University, Montréal, 2002

A THESIS SUBMITTED IN PARTIAL FULFILMENT OF
THE REQUIREMENTS FOR THE DEGREE OF
MASTER OF SCIENCE
in
THE FACULTY OF GRADUATE STUDIES
(Geological Science)

THE UNIVERSITY OF BRITISH COLUMBIA

October 2006

ABSTRACT

The Pliocene El Dorado epithermal Au-Ag vein system, located in northern El Salvador, is hosted in Tertiary volcanic rocks that accumulated along the Caribbean plate margin in response to the subduction of the Farallon/Cocos plate. The volcanic basement rocks in the district form a >400-meters-thick sequence of basaltic to andesitic lava flows and sedimentary rocks that were intruded by porphyritic basaltic to andesitic domes and dikes during the late Miocene. These rocks petrologically correlate with the Eocene to Miocene Morazan Formation of El Salvador. Mineralization in the district is constrained between ~4.7 and 4.0 Ma, and likely occurred closer to the lower limit according to field relationships and ^{40}Ar-^{39}Ar ages of bracketing volcanic rocks. The waning stage of hydrothermal activity coincides with the onset of a period of extensive Pliocene felsic volcanism (~4.0 to ~3.3 Ma) based on field relationships and ^{40}Ar-^{39}Ar geochronology of hornblende-biotite-phyric dacitic to rhyolitic lava flows, domes and related pyroclastic and sedimentary rocks. Pliocene and possibly younger post-mineral basaltic to andesitic lava flows cap the volcanic sequence.

The sub-arc mantle source that generated primary magmas during the Miocene and Pliocene is compositionally constrained between a depleted- and an enriched-MORB. Selected trace element ratios (e.g., Ba/Th) suggest that subducted sediments and/or slab-derived fluids account for some of the geochemical variation in volcanic rocks at El Dorado. The Sr, Nd and Pb initial (and measured) isotopic ratios of all volcanic rocks are remarkably uniform, independent of age or rock type, likely indicating that the isotopic composition of Tertiary magmas was buffered by the mantle, and possibly, by a constant input of hemipelagic sediments during the Miocene and Pliocene. Short mixing trends in Pb isotopes further suggest that Pliocene felsic magmas were generated from partial melting of previously emplaced sub-arc igneous rocks, isotopically equivalent to the high $^{206}Pb/^{204}Pb$ volcanic basement rocks in the district, by introducing low $^{206}Pb/^{204}Pb$ mantle-derived basaltic magmas in deep crustal hot zones (Annen et al., 2006).

The current exposures from north to south at El Dorado appear to represent an oblique cross-section through the volcanic and hydrothermal system associated with the low-sulfidation epithermal vein system. North and Central El Dorado, being dominated by the mafic basement rocks, represent the deeper parts of the system. South El Dorado is

clearly the shallow level of the epithermal vein system, preserving the surface and shallow sub-surface environments, including the sinters and contemporaneous to post-mineral felsic volcanic rocks. The distribution of volcanic facies along Titihuappa River, a regional fault zone on the extreme south of the district, appears to define the northwestern margin of the Pliocene Rio Titihuappa basin, potentially representing a volcano-tectonic depression that formed during and/or shortly following vein formation.

The Miocene to Pliocene transition in Central America is marked by a trenchward shift in subduction and associated magmatic activity (Weyl, 1980). The volcanic record preserved at El Dorado suggests that the Pliocene magmatic event led to the formation of compositionally evolved hydrous magmas that likely ponded in mid- to upper-crustal magma chamber(s). These magma chambers potentially represented the critical heat engine to the once active hydrothermal system and a possible source of precious metals. Extensive felsic volcanism associated with the Pliocene magmatic system, possibly in conjunction with caldera formation, may have suppressed the heat engine to hydrothermal activity.

References

Annen, C., Blundy, J.D., and Sparks, S.J., 2006, The genesis of intermediate and silicic magmas in deep crustal hot zones, Journal of Petrology, vol. 47, p. 505-539.

Weyl, R., 1980, Geology of Central America: Berlin-Stuttgart, Gebruder Borntraeger, 371 pp.

TABLE OF CONTENTS

LIST OF TABLES

CHAPTER 2

CHAPTER 3

LIST OF FIGURES

CHAPTER 1

CHAPTER 2

CHAPTER 3

PREFACE

Recent exploration by Pacific Rim El Salvador raised many controversial opinions about the negative impacts mining development may have on the environment. Indeed, ignorance in the past has caused natural disasters, leaving future generations with the burden of cleaning. This thesis was made possible with the support of Pacific Rim Mining Corp., and one of our goals is to help guiding future gold exploration in the region. My interests are also academic, and this work now contributes valuable scientific data, and promotes the advancement of knowledge, which will benefit to many researchers seeking to unravel the fascinating volcanic history of Central America.

I believe that mining development, despite the environmental impact it may have on a local scale, will be greatly beneficial to the local population by providing a sustainable economic potential which would otherwise not exist. If the wealth buried under the soil of Cabañas can be equitably redistributed to its inhabitants, not only under the form of individual salaries, but also in promoting development of local business, improving schools and education, recreational areas and sporting events, and water access…etc; these contributions will serve to future generations, and will have a much longer-lasting impact. We should combine our efforts to make sure that we mine in an environmentally conscious way, and that everyone can grow, especially the local population, from the wealth created by gold mining at El Dorado.

ACKNOWLEDGMENTS

I am indebted to the geologists of Pacific Rim Mining Corp. (D. R. Ernst, W.T. Gehlen, J.C. Olivares Dicic, J.C. Varela, R. Chavarria, L. Coto, R. Cortez, and E. Alvarado) who have provided invaluable efforts into building the geological map of the district and understanding the volcanic stratigraphy. Many thanks to the sponsors Pacific Rim Mining Corp., the National Science and Engineering Research Council, and the Society of Economic Geologists, who have provided funding for the project. Thanks to Thomas Ullrich who dedicated his time and efforts to produce excellent geochronological data, and to Bruno Kieffer who produced the isotopic analyses. Thanks to Richard Tosdal, Dominique Weis, and James Mortensen for their scientific input and the help with the editing process.

CHAPTER 1

GENERAL INTRODUCTION

1.1 Introduction

The Caribbean region has long been recognized for its wealth of mineral resources and potential for mining development (e.g., Kesler, 1978). Several genetic types of mineral deposits of different ages, including precious and base metals, occur in contrasting geological settings. Some of the key factors in the metallogenic evolution of the Caribbean region are the presence or absence of a pre-existing continental crust and the nature and evolution of volcanism (Kesler et al., 1990). Sub-aerially emplaced Tertiary volcanic rocks represent a major host to many low-sulfidation epithermal gold-silver deposits in northern Central America, the region defined by Guatemala, Honduras, El Salvador and Nicaragua (Figure 1.1), which is characterized by the presence of a Precambrian (?) to Paleozoic continental basement. The El Dorado gold-silver deposit located in northern El Salvador is a low-sulfidation epithermal vein system similar to other deposits found in the region, all of which developed in conjunction with Tertiary volcanism. The literature offers limited data on the age and volcanic setting of these precious metal deposits (e.g., Malone and Stoiber, 1987), and none that would make it possible to link the period of volcanism to mineralization. In many cases inferences about the age of district scale volcanic rock units are made by extending regionally correlative groups of rocks. Understanding the regional and district-scale volcanic history and the relationship to vein formation is thus a key factor to help elucidate part of the magmatic and metallogenic evolution of the Caribbean region and help guiding exploration.

The volcanic stratigraphy in El Salvador was established by the German Bundesanstalt für Bodenforschung in the early-1970's, and their 1:500,000 geological map (B.f.B., 1974) was the foundation to all assumptions concerning the volcanic framework of the El Dorado gold district. The ages assigned to volcanic rocks and associated epithermal veins were based on correlating the El Dorado district rocks to rocks in Guatemala, Honduras, and Nicaragua for which some scattered ages were reported (e.g., Reynolds, 1977; Weyl, 1980).

New field mapping, ^{40}Ar-^{39}Ar geochronology and lithogeochemistry of the volcanic rocks presented herein provide a new volcanic framework to the El Dorado epithermal vein system, constrain the timing of ore formation, and provide constraints on the temporal and geochemical evolution of the volcanic arc during the late Tertiary.

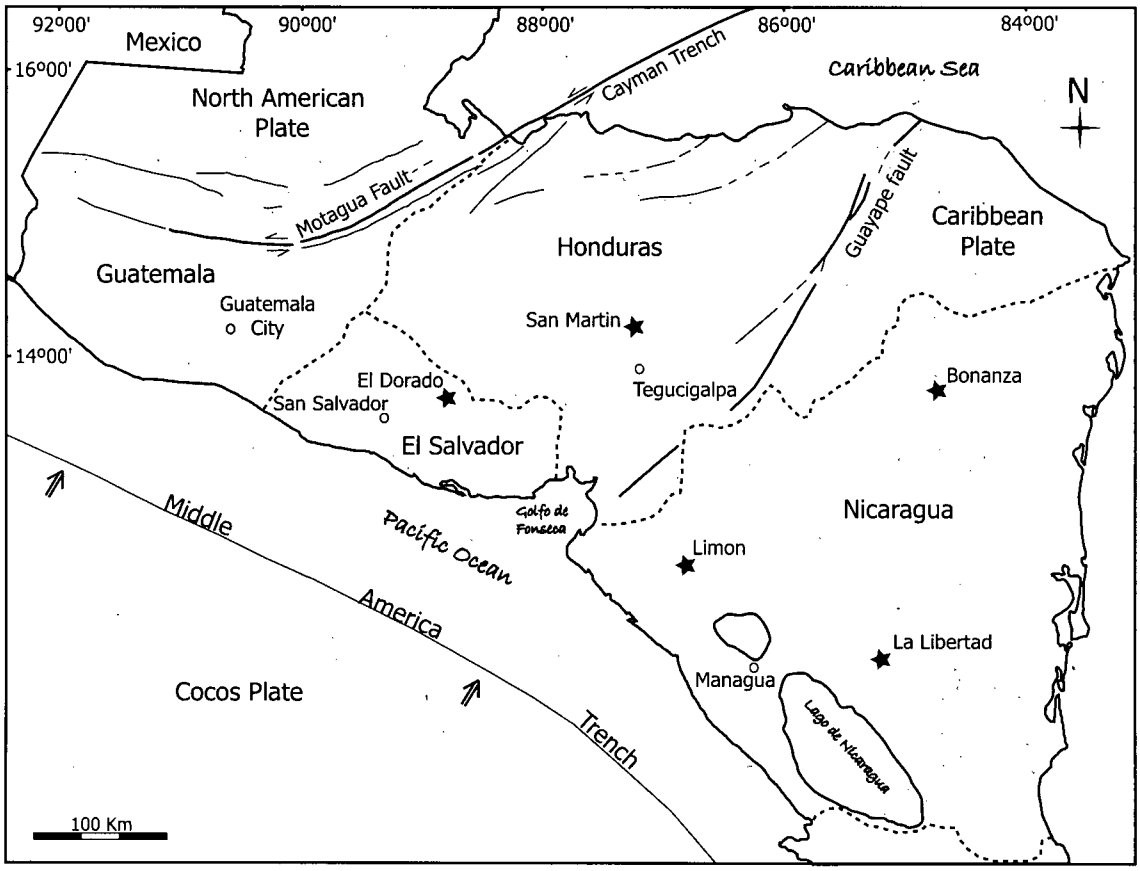

Figure 1.1. Geographical location of the El Dorado gold district and selected epithermal precious metal deposits in northern Central America.

1.2 Scope of Study

The age and volcanic framework of many precious metal deposits found in Central America are poorly understood. This was the case of the El Dorado gold district in El Salvador prior to this research project. In order to guide exploration work at the district and regional scale, the need to understand the district volcanic history and its relationship to mineralization is essential. Many fundamental questions were raised: What is the link between volcanic activity and mineralization at El Dorado? Which rock unit(s) was/were responsible for driving the once active hydrothermal system? How did tectonic movements affect the nature of magmatism and metallogenesis in El Salvador? In the Central American region?

This Masters of Science project, partly funded by Pacific Rim Mining Corp., the National Science and Engineering Research Council, and the Society of Economic Geologists, includes two main topics of research that aim to answer some of the above questions: 1) field geology and geochronology and 2) lithogeochemistry. The first objective of the study was to establish the volcanic framework of the El Dorado epithermal vein system, and draw parallels between district and regional scale volcanic stratigraphy. The second objective was to constrain the geochemical evolution of the volcanic rocks at El Dorado according to the established volcanic stratigraphy and geochronology. Ultimately, the goal is to link volcanic stratigraphy, geochemical evolution and mineralization into an evolving tectonic framework at the Caribbean plate margin. This study provides valuable information to guide future mineral exploration projects and contributes to the general scientific knowledge in the region.

1.3 Methodology

Field mapping of the El Dorado District has been an ongoing process since the early days of exploration on the property. The geological staff of Pacific Rim started mapping in 2002, after acquiring the mining concession, and the program was expanded at the beginning of 2003. To this date, the entire property has been mapped at a 1:1000 scale. This map was complemented by 1:10,000 and 1:20,000 scale mapping by the current study focusing on areas adjacent to the mining concession. Mapping by the author took place during two trips to El Salvador in May and June 2004 and from April to

August 2005. Vein and rock samples of major stratigraphic units were collected for geochronological study in order to constrain the absolute age(s) of volcanism and vein formation. Forty-six polished standard thin sections of selected samples were prepared by Vancouver Petrographics Ltd., and were examined by transmitted light microscopy. Petrographic work made it possible to identify the primary mineral assemblage of volcanic rocks, and although not a primary objective of the thesis, the main alteration minerals.

Major and trace elements geochemistry of volcanic rocks were obtained by whole rock XRF and ICP-MS at the ALS/Chemex Laboratories, North Vancouver. A suite of rocks representing the major stratigraphic units in the district were analyzed for selected high precision trace elements and Sr, Nd and Pb isotopic ratios at the Pacific Center for Isotopic and Geochemical Research at the University of British Columbia.

1.4 Presentation

This thesis is presented in the manuscript format with Chapters 2 and 3 each representing an article that will be reviewed for publication in scientific journals. For that reason, duplication of information between the two papers was inevitable. Chapter 2 will be sent for publication in Economic Geology. This publication will include an additional section by Richard M. Tosdal on the structural geology of the El Dorado district. Chapter 3 will be submitted as a Nature article.

1.5 References

B.f.B. (Bundesanstalt für Bodenforschung), 1974, Mapa geologico de la Republica de El Salvador (1:500,000): Hannover, B.D.R.

Kesler, S.E., 1978, Metallogenesis of the Caribbean region, Journal of the Geological Society of London, vol. 135, p. 429-441.

Kesler, S.E., Levy, E., and Martin F., C., 1990, Metallogenic evolution of the Caribbean region, *in* Dengo, G. and Case, J.E., eds., The Caribbean Region: Boulder, Colorado, Geology of North America, The Geology of North America, vol. H, p. 459-482.

Malone, G.B. and Soiber, R.B., 1987, Caldera-related gold mineralization of the El Limon mining district, western Nicaragua, Journal of Volcanology and Geothermal Research, vol.33, p. 217-222.

Reynolds, J.H., 1977, Tertiary Volcanic Stratigraphy of Northern Central America, Master's Thesis, Dartmouth College, Hanover, N.H., 89 pp.

Weyl, R., 1980, Geology of Central America: Berlin-Stuttgart, Gebruder Borntraeger, 371 pp.

CHAPTER 2

VOLCANIC FRAMEWORK OF THE EL DORADO GOLD DISTRICT, EL SALVADOR: CONSTRAINTS FROM RECENT FIELD MAPPING AND DETAILED ARGON GEOCHRONOLOGY

2.1 Introduction

The Caribbean region has long been recognized for its wealth of mineral resources and potential for mining development (e.g., Kesler, 1978). Tertiary volcanic rocks represent a major host to many low-sulfidation epithermal gold-silver deposits in northern Central America including the El Dorado district located in northern El Salvador (Figure 2.1). Despite the spatial association, there is little field and geochronology data that links periods of volcanism to the mineralization. Kesler (1978) suggested a genetic link between Tertiary ignimbrites and precious metal epithermal vein deposits in several mining districts of Central America. For instance, the El Limon and Cerro Mojon low-sulfidation epithermal gold deposits in Nicaragua are hosted by mafic to intermediate Miocene volcanic rocks, and overlain by extensive late Miocene to Pliocene rhyolitic ignimbrites and domes (Malone and Stoiber, 1987; Johnson et al., 2001). At both mining district, it is not clear whether the felsic rock sequence post-dates or pre-dates mineralization due to the lack of geochronology data and reported field observations. Nonetheless, veins at El Limon are inferred to have formed in a caldera setting, potentially in conjunction with felsic volcanism (Malone and Stoiber, 1987), as has been demonstrated in other mining districts (e.g., Henry, 1997). Understanding the volcanic history and its relationships to the formation of precious-metal epithermal vein deposits thus appears a key factor to elucidate part of the metallogenic evolution of northern Central America and hopefully guide exploration work. This manuscript addresses this issue at the El Dorado gold district in El Salvador.

Significant contributions to understanding the volcanic history of Central America was conducted by various geologists, and their valuable work remains the basis for today's stratigraphic framework (e.g., McBirney and Williams, 1965; Reynolds, 1977). The volcanic stratigraphy in El Salvador was established by the German Bundesanstalt für Bodenforschung and their map "Geologisch Ubersichtskarte der Republik El Salvador 1:500,000" (B.f.B., 1974) was the foundation for understanding the volcanic framework and estimating the age of the El Dorado low-sulfidation epithermal vein system.

Prior to this study, the mafic to intermediate volcanic rocks that form the volcanic basement and main host rocks to mineralization in the district were assigned an Oligocene age. Gold-bearing veins had been interpreted to have formed during the

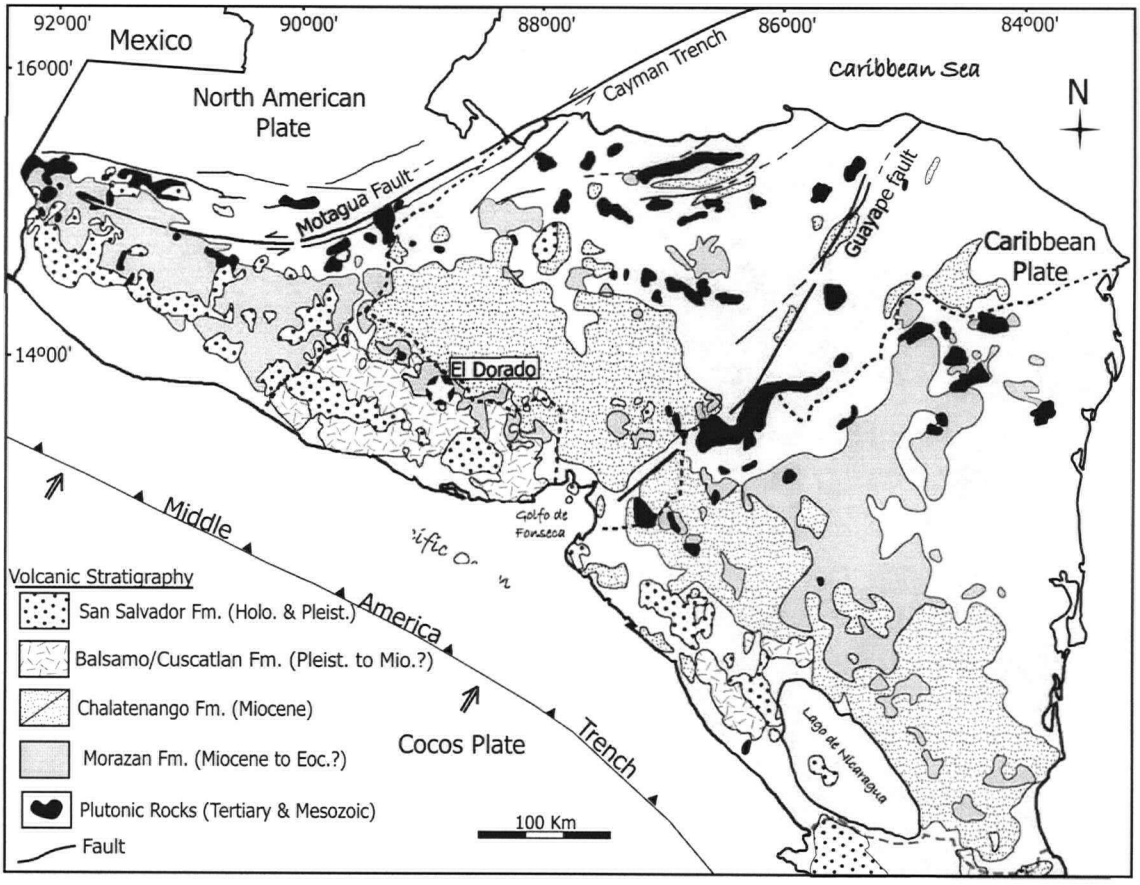

Figure 2.1. Distribution of Cenozoic volcanic and Mesozoic to Cenozoic intrusive rocks in northern Central America (modified from Weyl, 1980). Volcanic rock formations are named after the El Salvador nomenclature (Wisemann, 1975). Tertiary volcanic rocks in Guatemala include deposits of the Morazan and Chalatenango Formations, but are not differentiated on the map of Weyl (1980). They have been grouped as one single unit here under the Morazan Formation for illustration purposes.

Miocene, in close association with felsic intrusive and extrusive volcanic rocks, which unconformably overlie the mafic to intermediate volcanic basement rocks (Dayton Mining Corp. Feasibility Study, 2001). It was observed early in this study and by earlier workers (e.g., Dayton Mining Corp. Feasibility Study, 2001) that rocks at the base of the felsic volcanic sequence are widely silicified, veined and brecciated in the southern parts of the district, where the shallow level of the epithermal vein system are preserved. Post-mineral basaltic lava flows were assumed to be of Miocene to Pliocene age. The age assignments of the volcanic rocks and associated epithermal veins were based on correlating the El Dorado district rocks to rocks in Guatemala, Honduras, and Nicaragua where some limited ages were reported (e.g., Reynolds, 1977; Weyl, 1980). Field mapping and ^{40}Ar-^{39}Ar geochronology of the volcanic rocks at El Dorado presented herein provide a new volcanic framework of the district, constrain the timing of ore formation, and provide constraints on the temporal and spatial evolution of the volcanic arc during the late Tertiary.

2.2 El Dorado District Mining and Exploration History

The El Dorado Gold District was discovered during colonial times by the Spaniards, who first conducted surface trenching and pitting operations in the area (Dayton Mining Corp. Feasibility Study, 2001). In the late 19th and early 20th century, limited excavation in the central and southern areas of the District was carried by local miners (Eng. Carlos Serrano, pers. comm., 2005). In the late 19th century, mining operations of gold-bearing gravel and hydrothermal breccias took place in the southeastern parts of the district. The milling technique proved to be inadequate and gold recovery was very low due to the highly oxidized nature of the rock (Curran, 1975). The project ceased two and a half years later. Vestiges of the machinery are still in place today.

It was in 1948 that the New York and El Salvador Mining Company, a subsidiary of New York and Honduras Rosario Mining Company, acquired the property and initiated larger-scale underground mining and milling operations at El Dorado. Six main veins were mined, to a maximum depth of 130 meters, all found in close proximity: the El Dorado, Zancudo, Minita, Minita-3, Portillo and Moreno veins. Mining operations

ceased in 1953, apparently due to a combination of factors including low gold prices, limited resource and high demands by the workers union (Dayton Mining Corp. Feasibility Study, 2001). During the five years of operation, the mine produced a total of 270,197 tones of ore at an average grade of 9.59 g/t Au and 52.61 g/t Ag resulting in the recovery of 72,495 Troy ounces of gold and 355,163 Troy ounces of silver (Malouf, 1992).

In 2002, after several years of exploration work under different ownerships, the El Dorado gold district was acquired by Pacific Rim Mining Corporation. Diamond drilling started in May 2002, focusing on defining ore shoots on veins of the Central district. By mid-2005, Pacific Rim had drilled 177 holes throughout the El Dorado District, totaling 67,613.60 meters, and the program is an ongoing process to this date with many more untested vein targets. As of July 25 2006, total measured and indicated resources are calculated at 1,115,500 gold ounces (Pacific Rim News Release, July 25th 2006). The company is currently undergoing an environmental impact study, as the preliminary phase to start mining development.

2.3 Regional geology

Northern Central America, the region defined by Guatemala, El Salvador, Honduras and Nicaragua, is covered by extensive Tertiary and Quaternary volcanic rocks (Figure 2.1), unconformably overlying Mesozoic volcanic, marine carbonate and clastic sedimentary rock successions and Precambrian (?) to Paleozoic metamorphic and plutonic cratonic basement (Weyl, 1980), which are not shown on the map. The volcanic rock sequences accumulated in response to the east to northeast subduction of the Farallon/Pacific and Cocos plates beneath the Caribbean plate along the Middle America Trench. At the regional scale, the volcanic rocks form continuous belts extending from Guatemala to central Costa Rica, with a general southwestward younging of the volcanic and intrusive rock package. In El Salvador, Miocene and older volcanic rocks are only found in the northern part of the country, in a belt roughly parallel to the active volcanic arc. Pliocene and younger volcanic rocks are found to the south, following the Pacific coastline. This pattern has been interpreted to reflect a trenchward shift in subduction and magmatic activity during the late Tertiary (Weyl, 1980), possibly as a consequence of

slab roll-back and/or due to the relative eastward migration of the Caribbean plate with respect to the subducting Cocos/Farallon plates (Meschede and Frisch, 1998).

The volcanic stratigraphy of El Salvador (Figure 2.2) was first compiled by Wiesemann (1975) after a 1:500,000 geological map of the entire country (B.f.B., 1974). The Tertiary volcanic rock formations identified in El Salvador extend into adjacent countries, forming regionally correlative groups of rocks (e.g. Reynolds, 1980), and their relative age is constrained by few radiometric dating results from Guatemala, Nicaragua and Honduras, and by contact relationships.

The oldest Tertiary volcanic rocks belong to the Eocene (?) to Miocene Morazan Formation, which is composed of mafic to intermediate lava flows and autobreccias, volcanogenic sedimentary rocks with intermediate to felsic pyroclastic rocks in the basal section. Rocks of the Morazan Formation are confined to the northern parts of El Salvador, and are widespread in the highlands of Nicaragua and Honduras where they have been described more extensively (Weyl, 1980). The Morazan Formation of El Salvador is considered stratigraphically equivalent to the Matagalpa Formation in Honduras. Rocks of the Matagalpa Formation have been dated at 28 Ma (Everett and Fakundiny, 1976), and in Nicaragua, the upper beds of the Formation were dated at 19.1 Ma and 17.2 Ma (McBirney and Williams, 1965) as reported by Weyl (1980), although the minerals and dating techniques were not reported. In Guatemala, the exact age of rocks equivalent to the Morazan Formation is unknown; however Reynolds (1977) reports a K/Ar age of 15.7 ± 0.6 Ma on biotite from a granite that intrudes the sequence.

The Miocene Chalatenango Formation in El Salvador is characterized by extensive felsic ignimbrites, lava flows, and domes. The Formation is equivalent to the lower Padre Miguel Group in Honduras and the Coyol Group in Nicaragua (Weyl, 1980). In El Salvador, the Formation is confined to the northern part of the country, and in Honduras and Nicaragua, it forms the greater part of the central highlands (Figure 2.1). The Padre Miguel Group discordantly overlies the Matagalpa Group in parts of central Honduras (McBirney & Weill, 1966), whereas in other regions a gradational contact separates the two Formations (Weyl, 1980). In Nicaragua, mafic to intermediate lava flows are found at the base of the Coyol Group. Nine samples from this stratigraphic horizon at the El Limon mining district span the period 14.9 ± 0.3 Ma to 12.0 ± 1.2 Ma as

Volcanic stratigraphy of El Salvador

Age	Formations	Facies descriptions	Av. silica (wt%)
Holocene	San Salvador Fm	Lavas and tephras of the Quaternary volcanoes along the volcanic front and back-arc regions;	52.4-65.7
Pleistocene to Pliocene	Cuscatlan Fm	Felsic pyroclastic and epiclastic rocks at the base grading into felsic to intermediate lava flows and domes;	–
4.0±0.2 Ma			
4.1±0.4 Ma			
Pliocene to Miocene?	Balsamo Fm	Mafic to intermediate lava flows and associated autobreccias intercalated with epiclastic to pyroclastic rocks ;	–
9.4±0.4 Ma			
Miocene	Chalatenango Fm	Extensive felsic pyroclastic and epiclastic rocks locally interbedded with felsic lava flows;	70.8
15.7±0.6 Ma			
Miocene to Eocene?	Morazan Fm	Felsic to intermediate intrusive rocks;	–
		Mafic to intermediate lava flows and autobreccias, volcanogenic sedimentary rocks and intermediate to felsic epiclastic and pyroclastic rocks;	57.7

Figure 2.2. Volcanic stratigraphy of El Salvador based on the regional mapping conducted by German geologists in the 1970's (B.f.B., 1974). Age limits are from Catastro (1972) and Reynolds (1977, 1980). The average composition of volcanic rock Formations are from Pichler and Weyl (1973).

reported by Malone and Stoiber (1987), although the minerals and dating technique are not mentioned. Three K/Ar ages of 13.1 ± 0.8 Ma, 12.5 ± 0.3 Ma, and 12.0 ± 1.2 Ma were obtained on biotite from rhyolite ignimbrites in Nicaragua (Catastro, 1972). In western Guatemala, two rhyolite tuffs yielded K/Ar ages on biotite of 11.6 ± 0.5 Ma and 9.4 ± 0.4 Ma (Reynolds, 1977).

The late Miocene (?) to Pliocene Balsamo and the Pliocene to Pleistocene Cuscatlan Formations consist of extensive mafic to intermediate lava flows and of intermediate to felsic lavas and pyroclastic rocks respectively (Baxter, 1984). The base of the Balsamo Formation is locally intercalated with felsic ignimbrites of the Chalatenango Formation (Weyl, 1980). Lava flows in Nicaragua with whole rock K/Ar ages of 6.65 ± 0.3 Ma and 4.1 ± 0.4 Ma (Catastro, 1972) have been included in the Balsamo Formation. In Guatemala, the lower limit of the Cuscatlan Formation is constrained by a K/Ar age of 4.0 ± 0.2 Ma on biotite from a rhyolite lava flow at the base of the section (Reynolds, 1980). The Quaternary San Salvador Formation consists of the mafic to felsic eruption products of active volcanoes of the Central American volcanic arc.

2.4 Geochronology methods

The geochronology of volcanic rocks building the framework of the El Dorado epithermal veins system is provided by ^{40}Ar-^{39}Ar plateau ages of nine rock samples representing different stratigraphic levels, and one sample of vein adularia. Additional K-Ar ages from two rocks and two veins samples were produced at the University of Texas at Austin (F. McDowell, written comm., 2006).

All analyses were performed by T.D. Ullrich at the Noble Gas Laboratory, Pacific Centre for Isotopic and Geochemical Research at the University of British Columbia. The rock samples were first crushed, then concentrated by Wilfey table, and furthermore by Frantz or hand magnetic separation. Mineral separates were hand-picked, wrapped in aluminum foil and stacked in an irradiation capsule with similar-aged samples and neutron flux monitors (Fish Canyon Tuff sanidine, 28.02 Ma (Renne et al., 1998)). The samples were first irradiated at the McMaster Nuclear Reactor in Hamilton, Ontario, for 24 MWH, with a neutron flux of approximately $3x10^{16}$ neutrons/cm^2. Then the mineral separates were step-heated at incrementally higher powers in the defocused beam of a

10W CO_2 laser (New Wave Research MIR10) until fused. The gas evolved from each step was analyzed by a VG5400 mass spectrometer equipped with an ion-counting electron multiplier. All measurements were corrected for total system blank, mass spectrometer sensitivity, mass discrimination, radioactive decay during and subsequent to irradiation, as well as interfering Ar from atmospheric contamination and the irradiation of Ca, Cl and K (Isotope production ratios: $(^{40}Ar/^{39}Ar)_K = 0.0302 \pm 0.00006$, $(^{37}Ar/^{39}Ar)_{Ca} = 1416.4 \pm 0.5$, $(^{36}Ar/^{39}Ar)_{Ca} = 0.3952 \pm 0.0004$, $Ca/K = 1.83 \pm 0.01(^{37}Ar_{Ca}/^{39}Ar_K)$.

The ages were determined by plateau (spectrum) and inverse correlation plots using Isoplot ver.3.09 (Ludwig, 2003). Errors are quoted at the 2-sigma (95% confidence) level and are propagated from all sources except mass spectrometer sensitivity and age of the flux monitor. The results are summarized in Table 2.1, and the full data set is included in appendix A. The plateau ages plots are shown in Figure 2.3. All ages produced on biotite separates were analyzed twice to ensure age reproducibility. Plagioclase separates were only analyzed once, and the adularia vein sample three times. Where applicable, the mean weighted ages of replicate analyses were taken as the representative age for the respective rock unit.

Table 2.1
Summary of ^{40}Ar-^{39}Ar plateau ages.

Sample	Description	Plateau age	Mean weighted age	Mineral separate
MR05-74	Central El Dorado andesite porphyry	10.7±1.9 Ma	-	plagioclase
MR05-55	La Tablita platy andesite	4.52±0.86	-	plagioclase
MR05-58	South El Dorado platy andesite	4.57±0.74 Ma	-	plagioclase
MR04-37	Cerro Alto rhyolite dome	3.415±0.050 Ma	3.43±0.04 Ma	biotite
MR04-37 run #2	Cerro Alto rhyolite dome	3.438±0.054 Ma		biotite
MR04-24	Cerro Avila dacite dome	3.62±0.11 Ma	3.62±0.08 Ma	biotite
MR04-24 run 2	Cerro Avila dacite dome	3.61±0.11 Ma		biotite
MR04-50	Cerro La Tabla rhyolite flow	3.56±0.15 Ma	3.6±1.3 Ma	biotite
MR04-50 run 2	Cerro La Tabla rhyolite flow	3.78±0.21 Ma		biotite
MR04-58	Cerro Alto summit rhyolite	3.343±0.046 Ma	3.36±0.49 Ma	biotite
MR04-58 run 2	Cerro Alto summit rhyolite	3.440±0.094 Ma		biotite
MR04-73	Pyroclastic breccia El Gallardo area	3.93±0.21 Ma	3.93±0.17 Ma	biotite
MR04-73 run 2	Pyroclastic breccia El Gallardo area	3.94±0.29 Ma		biotite
MR05-54	Titihuappa River basalt lava flow	<10.8 ± 1.9 Ma	-	plagioclase
MR04-75 run 1	South Minita Vein	4.06±0.29 Ma	-	Adularia
MR04-75 poor run	South Minita Vein	3.6±2.5 Ma	-	Adularia
MR04-75 run 3	South Minita Vein	4.31±0.19 Ma	-	Adularia

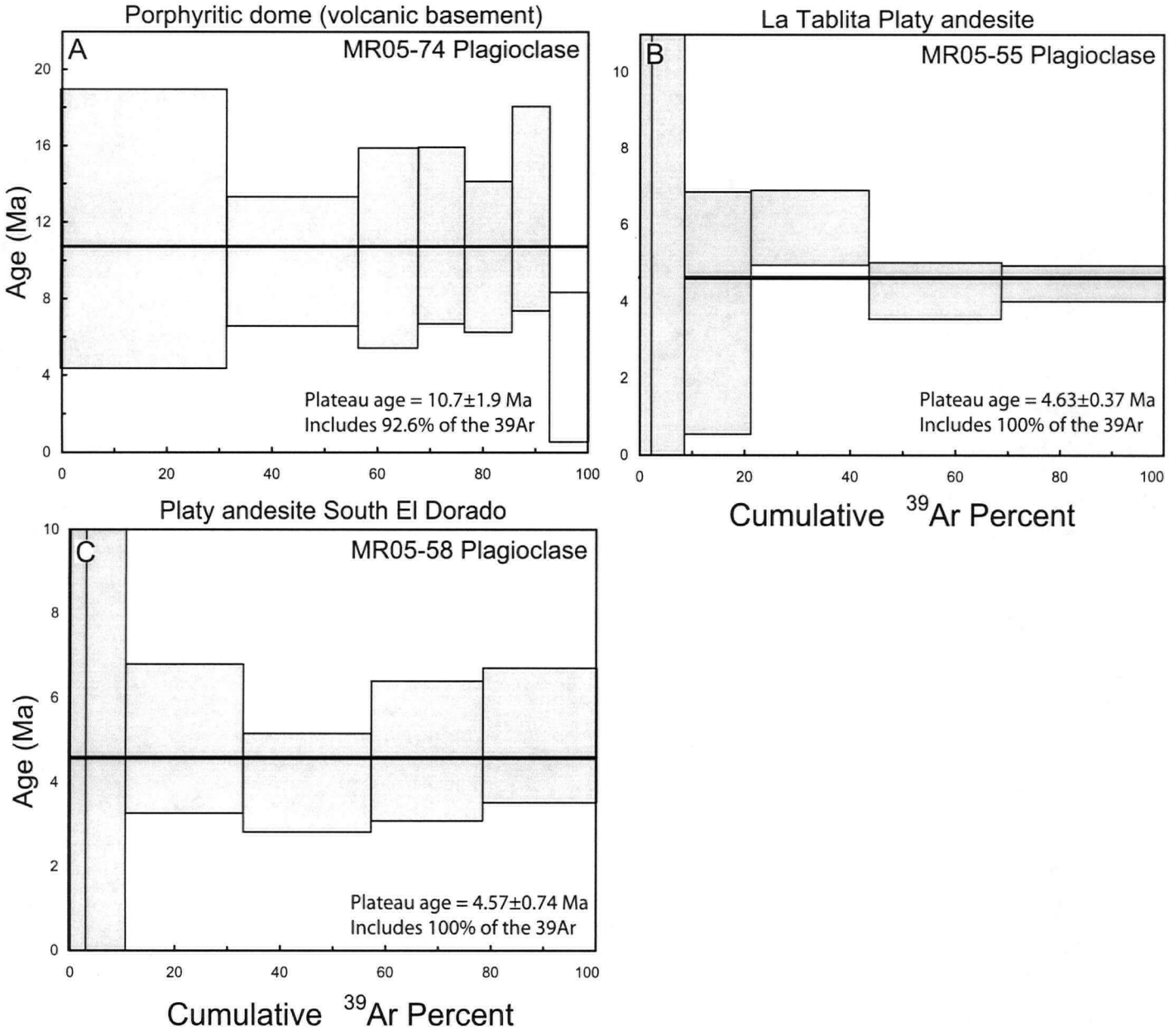

Figure 2.3. A) to Q) Argon plateau ages of nine rock units of the El Dorado district and one vein sample. The grey shaded box are included in the age calculation while the white boxes are rejected steps. See text for analytical description and appendix A for complete data set.

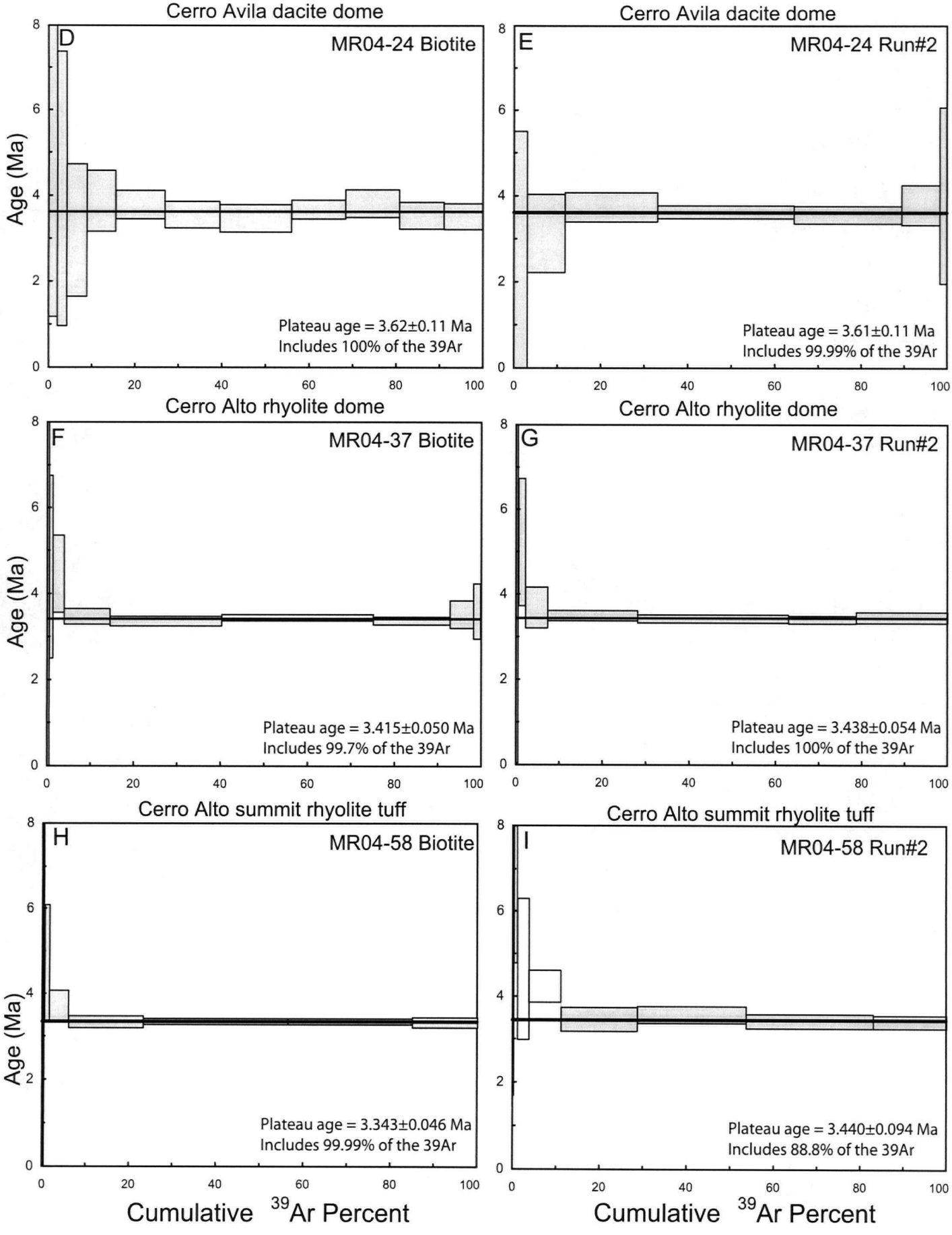

Figure 2.3. Cont'd.

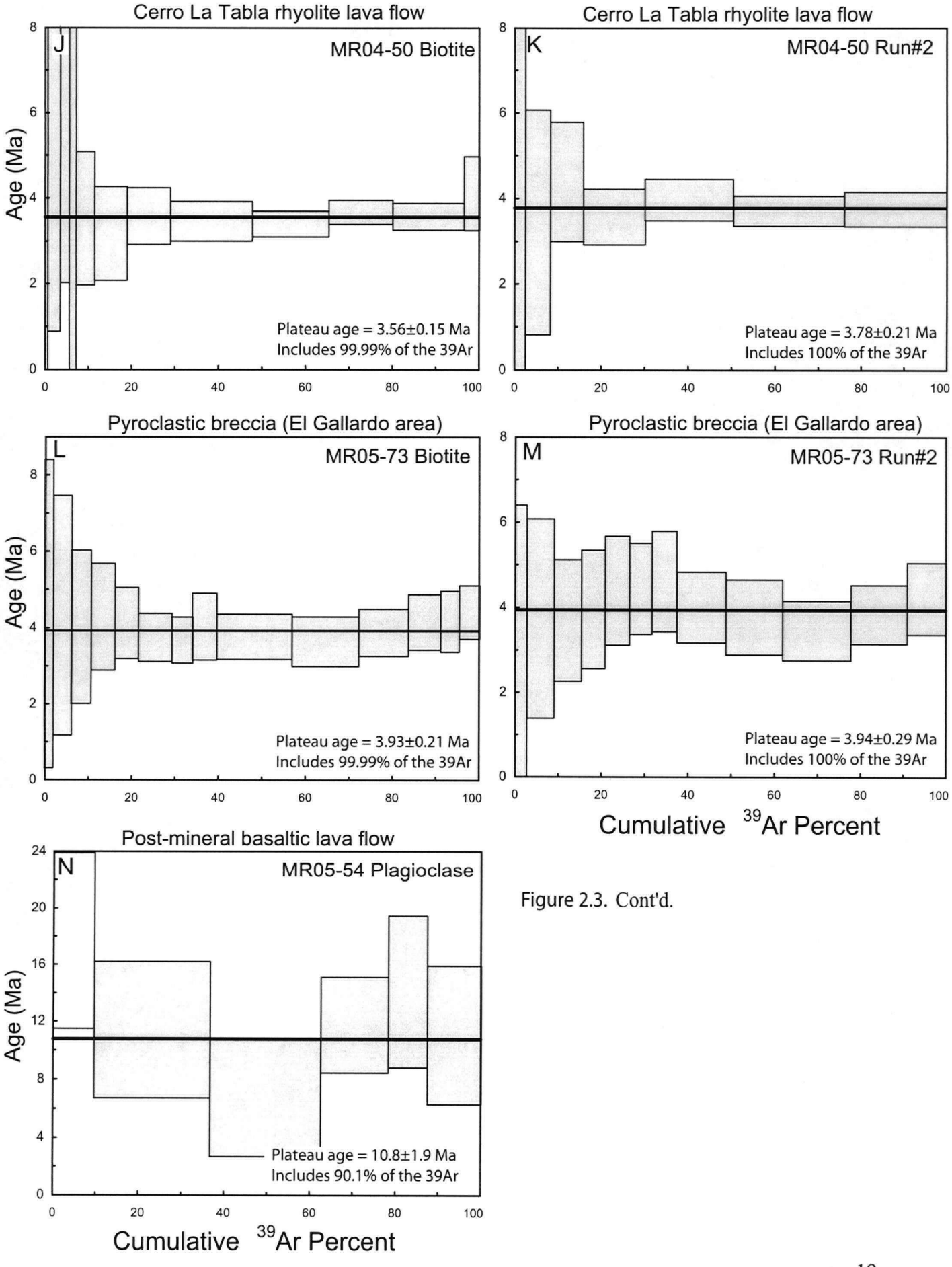

Figure 2.3. Cont'd.

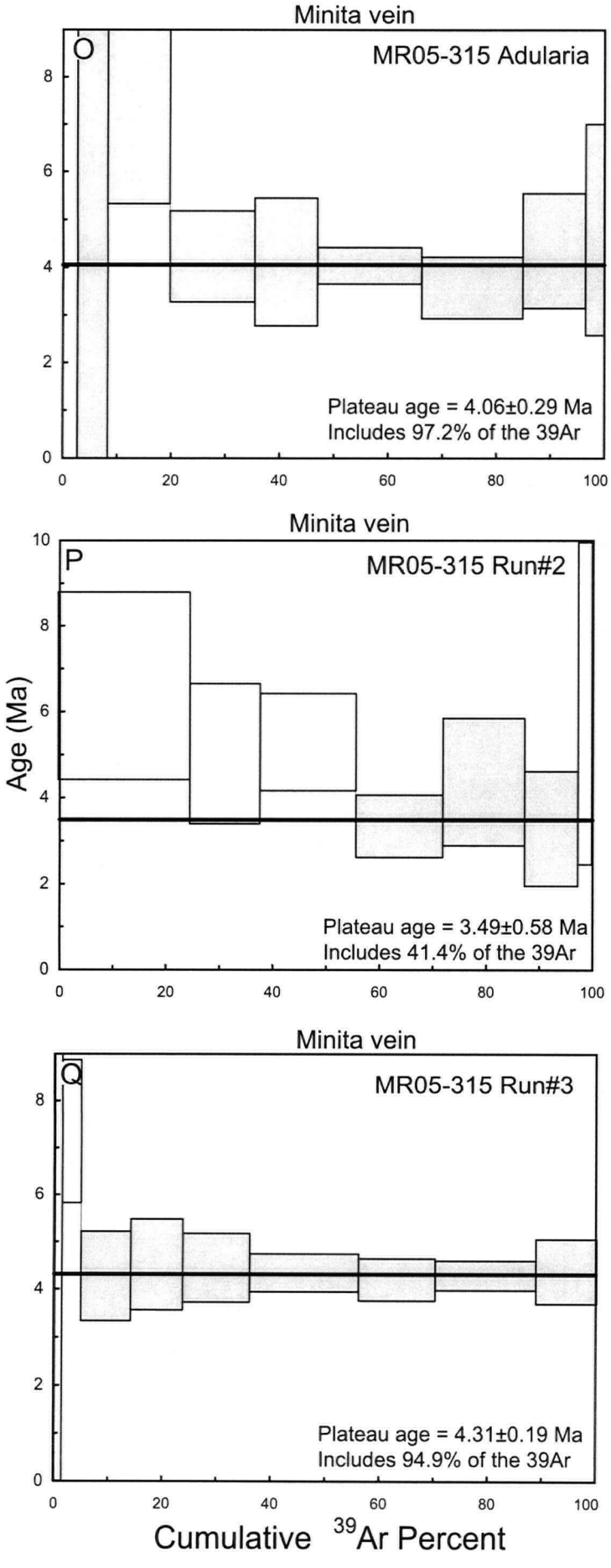

Figure 2.3. Cont'd.

2.5 District Volcanic Stratigraphy

The geology of the El Dorado district has been investigated since the early days of exploration (e.g., Curran, 1975). Various maps of specific areas of the El Dorado district were produced by the geological staff of the different companies owning the concession over the years but none had covered the entire district in detail. In July 2005, the geological staff of Pacific Rim El Salvador recompiled the map of the entire district from nearly three years of mapping at a 1:1,000 scale. This map was further complemented by 1:10,000 and 1:20,000 scale mapping by the author of areas adjacent to the concession limit. The detailed geological map is attached as a separate plate. A simplified version of the district geology is shown in Figure 2.4, and a schematic version of the district stratigraphy broadly describing the volcanic facies of major rock units, their relative ages, and compositional range in terms of silica content is illustrated in Figure 2.5. This figure draws a parallel between the district and regional scale stratigraphic sequences (see Figure 2.2).

2.5.1 The volcanic basement rock sequence

The oldest rocks and effective basement in the El Dorado district is a >400 meters-thick sequence of mafic to intermediate volcanic rocks found extensively in the central and northern parts of the district (Figure 2.4), where they outcrop at elevations between 400-650 meters above sea level. Two main packages of rocks are identified: 1) a lower sequence of Miocene and/or older (?) basaltic to andesitic lava flows interbedded with volcanogenic sedimentary rocks that was intruded by 2) basaltic to andesitic porphyritic domes and dikes during the late Miocene. The lower lava flow and sedimentary rocks sequence is the principal host to epithermal veins in Central and North El Dorado, although the two rock packages are hydrothermally altered and cut by veins. The stratigraphic base of the sequence is unknown as even deep exploration drilling to elevations below sea level has not encountered it.

In North El Dorado, the lower volcanic rock sequence consists of poorly to well sorted, fragment supported, mafic volcanic conglomerates intercalated with thin andesitic lava flows (generally less than 5 meters thick). In the northwest area of the district, the conglomerate sequence reaches a thickness in excess of 300 meters and bedding generally dips to the south and west between 4° and 30°. Individual conglomerate beds

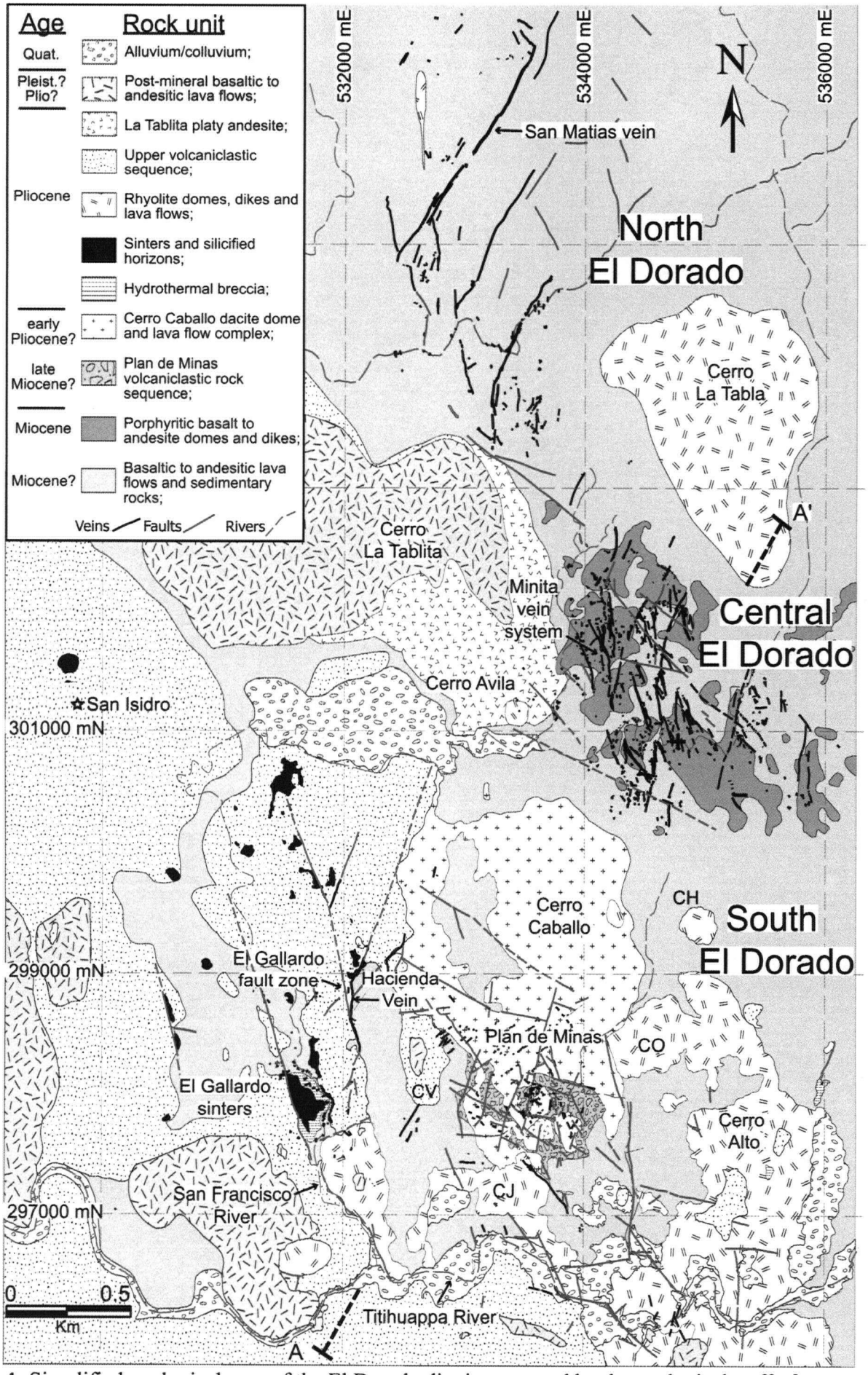

Figure 2.4. Simplified geological map of the El Dorado district prepared by the geological staff of Pacific Rim El Salvador (2005). CV: Cerro Volcancillo; CO: Cerro Oloton; CH: Cerro Humeras; CJ: Cerro de los Jesuses.

Volcanic stratigraphy of the El Dorado district

Age	District Unit Name	Facies descriptions	Silica (wt %)
Pleist.? Pliocene?	Post-mineral lava flows	-Mafic to intermediate lava flows;	51 to 60
3.36±0.49 Ma to 3.93±0.17 Ma	Pliocene felsic rock sequences	-Coeval felsic pyroclastic to tuffaceous sedimentary rocks and rhyolitic to dacitic domes/plugs/dikes and lava flows;	66 to 76
4.06±0.29 Ma to 4.7±0.2 Ma (?)	Epithermal veins and sinters	-Sinter deposits and silica replacement horizons associated with hydrothermal breccias;	
Pliocene	Cerro Caballo dome complex	-Dacite dome complex associated with flow banded, spherulite/lithophysae-rich lava flows;	63 to 69
	Plan de Minas volcaniclastics	-Intermediate to felsic, interbedded epiclastic and pyroclasitc rock sequence;	
4.57±0.74 Ma to 4.63 ± 0.37 Ma	Platy andesites	-Andesite lava flows (post-mineral?);	57 to 60
10.7±1.9 Ma Miocene Oligocene?	Volcanic basement rock sequence	-Porphyritic basalt to andesite domes and dikes; -Basaltic to andesitic lava flows and autobreccias, interbedded with volcanogenic sedimentary rocks ;	50 to 60

Figure 2.5. Volcanic stratigraphy of the El Dorado district with timeline constrained by current geochronology results and those of McDowell (written comm., 2006). Compositional range of different rock units in terms of silica content from current study.

reach up to about 10 meters in thickness and may be very chaotic, including sub-angular clasts up to 1 meter across in a sub-meter to centimeter-size clastic matrix. Locally, the conglomerates are interbedded with finely laminated sandstone and pebblestone. In the San Matias vein area, the volcanic conglomerates are unconformably overlain by at least 150 meters of mafic lava flows with minor intercalated volcaniclastic sedimentary rocks (sample MR04-92 in Appendix B). Exploration drilling at the southern end of the San Matias vein has shown felsic pyroclastic rocks and a flow banded biotite-bearing dacite lava flow interbedded with the mafic lavas. The flow banded dacite is pervasively silicified and hosts barren hydrothermal breccias cemented by chalcedony and quartz. These rock units are the only occurrence of felsic volcanic rocks as part of the dominantly mafic to intermediate volcanic basement rock sequence at the district scale.

The lower stratigraphic sequence in Central El Dorado consists of interbedded, fine- to medium-grained, pyroxene-plagioclase-phyric, basaltic to andesitic lava flows, with minor interbedded mafic volcanogenic sedimentary rocks. Bodies of coarse- to medium-grained plagioclase-pyroxene-phyric basaltic to andesitic porphyry intruded the lava sequence during the late Miocene (^{40}Ar-^{39}Ar plateau age of 10.7 ± 1.9 Ma on plagioclase; Figure 2.3a; Table 2.1; sample MR05-74). See sample MR04-06 and MR04-03 in Appendix B for petrographic descriptions of the rock unit. Coarse-grained porphyritic lava flows and agglomerates with dominant clasts of porphyritic andesite have also been observed to alternate with fine-grained mafic lavas in the upper sections of some drill holes. The porphyries appear to form lava domes in the upper parts of the section with dikes commonly extending laterally from larger bodies.

In South El Dorado, the volcanic basement rocks include similar rock types to those in Central and North El Dorado, and are widely overlain by younger stratigraphic units. East of Cerro Alto, mafic lava flows are interbedded with conglomerates in an at least 300 meters-thick section (sample MR04-53 in Appendix B). Dikes of medium-grained plagioclase-pyroxene-phyric andesite porphyry cross-cut the sequence. In the Cerro Volcancillo area, andesite basement rocks host the Volcancillo vein as well as vein stockworks below the sinters of the El Gallardo area.

The volcanic basement rocks represent different parts of a complex volcanic sequence that potentially was composed of multiple coalescing and superimposed

volcanic centers. Only broad scale petrologic types or volcanic facies were extended throughout the district.

A general south-southwest younging of rock units, associated with a southward topographic decline, is observed at the district scale. The highest stratigraphic units and erosional levels are mainly preserved in South El Dorado at elevations between 250-450 meters above sea level (Figure 2.4). The following section describes, in stratigraphic order, the volcanic rock units that unconformably overlie the volcanic basement rocks in the district, with emphasis on specific sections or genetically related groups of rocks. All these rock units yielded Pliocene ^{40}Ar-^{39}Ar ages (see Table 2.1 and Figure 2.3).

2.5.2 La Tablita platy andesite

The oldest Pliocene volcanic rocks, according to geochronology results, consist of plagioclase-pyroxene-phyric andesitic lava flows with a gently dipping fracture pattern, and are informally referred to as "platy andesite" (sample MR04-19 and MM13 in Appendix B). The base of Cerro La Tablita is composed of platy andesite, where it appears to form the toe of an up to 100-m-thick lava flow that unconformably overlies the intrusive Miocene basement rocks of Central El Dorado (Figure 2.4). The age of the La Tablita platy andesite is constrained by one ^{40}Ar-^{39}Ar plateau age on plagioclase phenocrysts at 4.63 ± 0.37 Ma (Figure 2.3b; Table 2.1; sample MR05-55). The andesite lava flow does not host any veins at the surface, and thus appears to post-date vein formation (see below). An outcrop of fresh platy andesite found in the Plan de Minas area in South El Dorado yielded a ^{40}Ar-^{39}Ar plateau age of 4.57 ± 0.74 Ma on plagioclase (Figure 2.3c; Table 2.1; sample MR05-58). The rock was interpreted to represent the roof of an intrusive body (D. Ersnt, pers. comm., 2004). Petrographic work would suggest an intrusive origin given the crystal rich nature of the rock (sample MR04-19 in Appendix B).

2.5.3 Plan de Minas volcaniclastic rock sequence

An up to 140-meters-thick sequence of volcaniclastic rocks overlie the volcanic basement rocks in the Plan de Minas area. The sub-horizontally bedded rocks are composed of well- to poorly-sorted volcanogenic conglomerates and breccias, and well-sorted, clast-supported, parallel- to cross-laminated, pumice-bearing sandstone and pebblestone. The absence of biotite crystals associated with the pumice fragments

distinguishes this volcaniclastic rock sequence from younger volcaniclastic deposits where biotite is ubiquitous (see below).

This volcaniclastic rock sequence is strongly affected by hydrothermal alteration and hosts numerous mineralized veins at the surface and at depth based upon exploration drilling (sample MR04-96 in Appendix B). Due to the lack of datable minerals, the age of the Plan de Minas epiclastic rock sequence is not constrained by geochronology, but the sequence is cross-cut and overlain by the Cerro Caballo dacite dome and lava flow complex.

2.5.4 Cerro Caballo Dome Complex

Central and South El Dorado are separated, in part, by a hornblende-pyroxene-phyric dacitic dome and lava flow complex which represents the bulk of Cerro Caballo and the Plan de Minas areas. The age of the Cerro Caballo dome complex remains unknown at this point, although it predates epithermal vein formation, since parts of the dome and associated lava flows host mineralized veins at the surface. Attempts to date the rock by U-Pb method on zircons yielded very large uncertainties likely due to lead-loss, low uranium concentrations and the presence of inherited cores (R. Friedmann, pers. comm., 2005). Hornblende phenocrysts proved to be too altered for argon geochronology. Due to similarities in mineralogy (i.e., the presence of hornblende in the mineral assemblage) and geochemistry with Pliocene felsic rocks (see Chapter 3), the dome is assumed to have been emplaced during the early Pliocene, possibly a few hundred thousand years prior to mineralization (see below for age constraints on veins). Nonetheless, the dome complex may have been emplaced during the late Miocene. Dating of additional zircons and/or hornblende will be attempted in the fall of 2006.

The dome complex comprises two main facies with associated breccias: a sub-vertically flow banded, medium-grained, coherent intrusive dacite, and a sub-horizontally flow-banded, finer-grained, spherulite-lithophysae-rich dacite. Both facies are shown as part of the same unit on the simplified map (Figure 2.4). On the detailed map (see attached plate), the intrusive facies are represented by the dark orange whereas the lava flows are shown in a lighter shade.

The bulk of Cerro Caballo represents the core of the dome rock, and the fresh dacite does not host any veins at the surface (samples MR04-42 and MM29 in Appendix

B). In the Plan de Minas area, the dome rock becomes strongly vertically flow banded, oxidized and silicified (sample MR04-43 in Appendix B), where it hosts the Cerro Flor vein (see detailed geological map plate).

In the Plan de Minas area, the dome rock grades southward into strongly flow banded to flow folded, spherulite-lithophysae-rich dacite. Flow foliations generally dip less than 30°, and the dacite is found in depositional contact over the Plan de Minas volcaniclastic rock sequence (see above). Petrographic work on these rock samples revealed euhedral to subhedral phenocrysts in a finely flow-banded groundmass (samples MR04-79 and MR04-75 in Appendix B). The dacite likely represents lava flow facies associated with the Cerro Caballo dome. Monolithologic autobreccias are commonly found in association with the flows (Appendix A, sample MR04-94). The breccia matrix is locally replaced and cemented by goethite-hematite-rich fine-grained quartz, suggesting a hydrothermal overprint. The lava flows are strongly hydrothermally altered, and host numerous veins at the surface.

Due south of the western portion of Cerro Oloton, a breccia unit forms a 500 meters long by 200 meters wide ridge. The breccia is found in depositional contact with the underlying Plan de Minas volcaniclastic rock unit and the volcanic basement rocks. The fragment-supported breccia is chaotic, principally contains fragments of flow banded dome rock ranging in size from sub-centimeter to 2 meters across, with less than 5% andesite fragments up to a few centimeters across (Figure 2.6a; sample MR04-23 in Appendix B). The dark-red hematized matrix, composed of moderately silicified ash-size particles, represents less than 10% of the rock. The breccia fragments share identical mineralogy and texture to the dome rock found due north, and may thus be the result of dome collapse.

2.5.5 Pliocene felsic rock sequences

The El Dorado district includes abundant felsic intrusive and extrusive rocks of Pliocene age. These rocks widely outcrop in South El Dorado (Figure 2.4), at elevations that vary between 250-450 meters above sea level. Two main groups compose the felsic sequence. These are: 1) coherent, biotite ± hornblende-bearing rhyolites and dacites, including domes, dikes and lava flows; and 2) volcaniclastic rocks, including tuffs, lapilli-tuffs, pyroclastic/tuff breccias and tuffaceous sedimentary rocks derived from

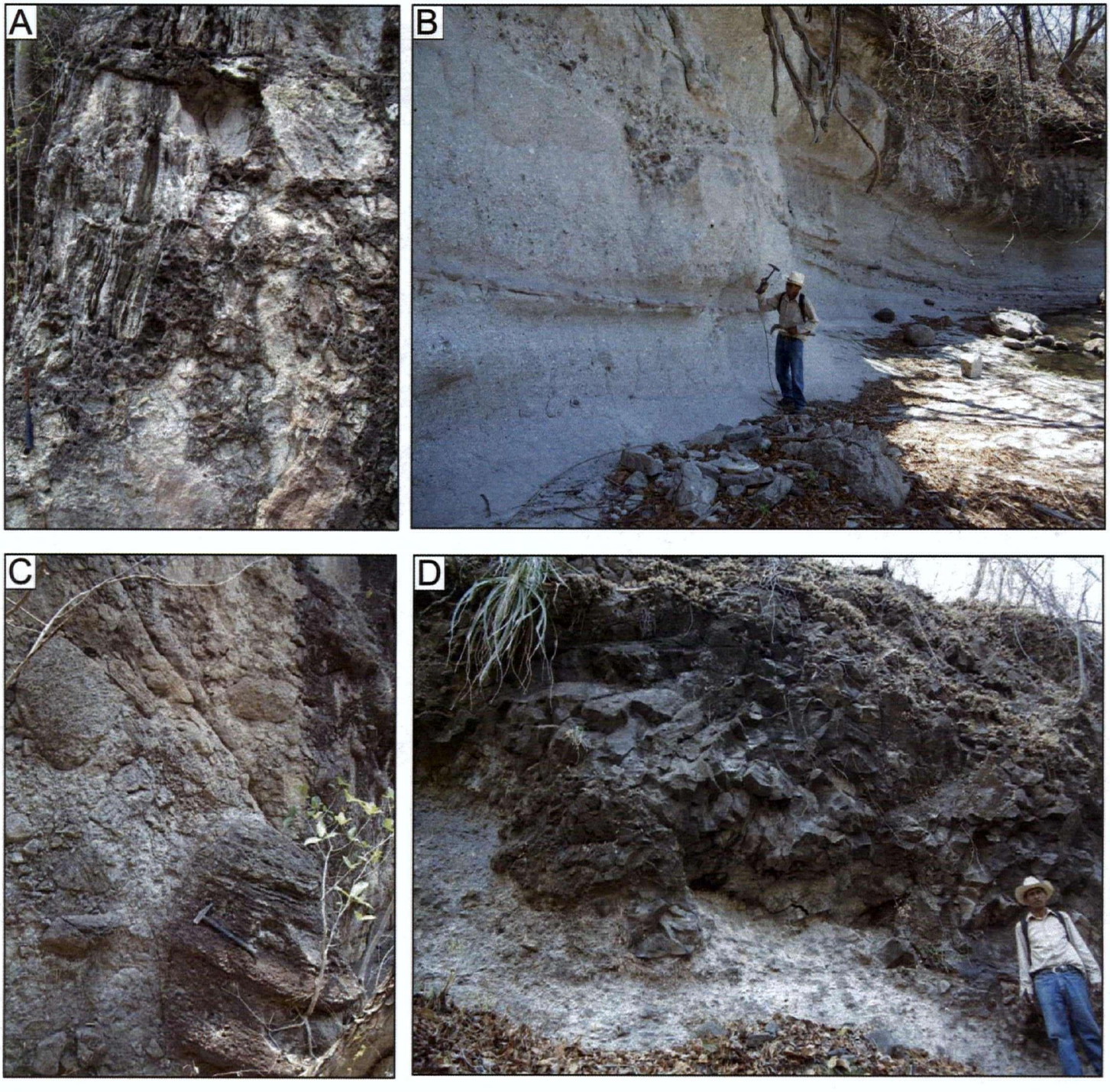

Figure 2.6. A) Chaotic, monolithologic breccia south of Cerro Oloton in South El Dorado. The breccia is composed almost entirely of flow banded Cerro Caballo dacite dome rock set in a silicified hematite-rich ash size matrix. B) Sub-horizontally bedded tuffaceous sedimentary deposits characteristic of the upper volcaniclastic sequence. C) Pyroclastic breccia unit found along the San Francisco River. Fragments of flow banded rhyolite represent 50% to over 75% of the rock. D) Columnar jointed basalt overlying tuffaceous sedimentary deposits of the upper volcaniclastic sequence south of the Titihuappa River. Lobes of radially jointed basalt are found in the sedimentary deposits suggesting load deformation as the lava flow was emplaced on top of wet sediments.

pyroclastic material. Rhyolite domes and plugs are mainly distributed along the Titihuappa River and the southeast margins of Cerro Caballo (Figure 2.4). The volcaniclastic rocks are mainly found to the south of the Titihuappa River and to the west of the Cerro Caballo dome complex.

The following section describes the nature and distribution of both types of felsic volcanic rocks (coherent and volcaniclastic), focusing on specific sections of South El Dorado.

2.5.5.1 North and Central El Dorado

In Central and North El Dorado, uncommon felsic intrusive bodies include a small dacite dome, Cerro Avila, that yielded a mean weighted ^{40}Ar-^{39}Ar plateau age of 3.62 ± 0.08 Ma on biotite (Figure 2.3d and e; Table 2.1; sample MR04-24 in Appendix B). The dome cross-cuts the platy andesite of Cerro La Tablita and thus provides a minimum age for the lava flow (see below). A biotite-phyric rhyolite dike is also mapped in North El Dorado (sample LC19 in Appendix B). In Central El Dorado, deep exploration drilling revealed a glassy hornblende-biotite-phyric rhyolite dike (sample MR04-01 in Appendix B), with similar mineralogy and texture to the Cerro La Tabla rhyolite lava flow (see below). Both dikes remain undated but likely were emplaced in conjunction with the Pliocene felsic rock sequences at the district scale.

2.5.5.2 Cerro Alto section

On the south side of the Cerro Alto summit, the stratigraphic section includes an unwelded lapilli-tuff. The unit outcrops in a type stratigraphic section, where the lapilli-tuff was intruded by a hornblende-biotite-phyric rhyolite dome and subsequently overlain by a biotite-rich rhyolite crystal tuff. The lapilli-tuff is approximately 20 meters thick, dips 14-18° to the southeast, and contains coarse-grained hornblende-biotite-rich rhyolite lithic fragments similar to most rhyolite domes found in South El Dorado. Due to the small size and distribution of outcrops, this rock unit was not included on the simplified geological map (Figure 2.4), but is shown on the detailed map (see attached plate).

The bulk of Cerro Alto is composed of flow banded biotite-hornblende-phyric rhyolite domes. One dome sample southwest of the Cerro Alto summit yielded a mean weighted ^{40}Ar-^{39}Ar plateau age of 3.43 ± 0.04 Ma on biotite (Figure 2.3f and g; Table 2.1; sample MR04-37 in Appendix B). A wide range of textures characterizes the rhyolite

in this area. South and southeast of the Cerro Alto summit, the rock is sub-vertically flow banded and brecciated close to the contacts with the volcanic basement rocks. Southwest of Cerro Alto, flow banded dome rock is cross-cut by stockworks and swarms of discontinuous tuff to lapilli-tuff dikelets up to 10 cm wide of similar mineralogy to the host rhyolite. In the same section, the flow banded rhyolite grades laterally into a matrix to fragment supported monolithologic breccia. The rhyolite-breccia contains 50% to 90%, lapilli to block size angular rhyolite fragments set in a reddish-brown, moderately silicified ash- to lapilli-size matrix. The rhyolite breccia fragments are identical in mineralogy to the coherent, flow-banded rhyolite. The change from coherent flow-banded to the brecciated facies is gradual and occurs over a distance of less than 100 meter.

Late plugs of crystal-rich flow banded hornblende-biotite-phyric rhyolite are found to the southwest of the Cerro Alto summit, cross-cutting the lapilli-tuff described previously, and early rhyolite dome rock (brecciated type). The plugs are similar in mineralogy to the flow banded and brecciated rhyolite, but are slightly coarser-grained and have a greater crystal content. Next to the Las Lavras River (see detailed map), the rhyolite plug is locally strongly silicified and hydrothermally brecciated with quartz cement. Zones of stronger silicification occur along flow bands, locally contain sub-millimeter disseminated pyrite, and anomalous gold. Rhyolite plugs with locally similar alteration are found directly south of the Plan de Minas area (Cerros de los Jesuses; sample MR04-16 in Appendix B).

The Cerro Alto summit is capped by a finely foliated rhyolite tuff that yielded a mean weighted ^{40}Ar-^{39}Ar plateau age of 3.36 ± 0.49 Ma on biotite (Figure 2.3h and i; Table 2.1). The 15-20 meters-thick tuff dips moderately (40° to 50°) to the north, locally contains up to 10% lithophysal cavities up to 3 mm across, and contains abundant ash shards and welded pumices (sample MR04-58 in Appendix B). The tuff is locally silicified, but does not host any veins.

2.5.5.3 South Gallardo rhyolite domes

Hornblende-biotite phyric rhyolite domes are found bordering the San Francisco Rivers south of the El Gallardo sinters. The dome yielded a K-Ar age of 3.5 ± 0.4 Ma on biotite (F. McDowell, written comm., 2006). The entire edifice is roughly 1340 meters long by 100 to 500 meters wide, and is limited by the north-northwest-striking El

Gallardo fault zone (see below) on the western margin. Flow banding commonly strikes between 170° and 190°, roughly parallel to the fault orientation. The rhyolite contains abundant barren chalcedony veins and veinlets (up to 10-15 cm wide), often sub-parallel or orthogonal to the flow banding orientation. These veins are discontinuous (rarely up to 25 meters in length) and locally form weak stockworks or dissipate into zones of moderate to strong silicification. Clay alteration (illite-smectite?) locally replaces the groundmass and phenocrysts, and is associated with goethite/hematite along fractures. Pyrite is very rarely found in association with the veinlets and none is found in the host rock.

A fresh hornblende-biotite-phyric rhyolite dome is found west of the San Francisco River in the same area. The dome rock shares mineralogical and textural characteristics with fragments composing a pyroclastic breccia found along the San Francisco River (see below) and could potentially represent the source of the breccia.

2.5.5.4 Rhyolite lava flows

The bulk of Cerro La Tabla consists of an approximately 50 meters-thick hornblende-biotite-phyric rhyolite lava flow that unconformably overlies mafic conglomerates that form part of the volcanic basement rocks. The rhyolite yielded a mean weighted ^{40}Ar-^{39}Ar plateau age of 3.6 ± 1.3 Ma on biotite (Figure 2.3j and k; Table 2.1). The glassy lava flow shows no sign of hydrothermal alteration or veining (sample MR04-50 in Appendix B). The age thus confirms the post-mineral nature of the rhyolite.

A similar rhyolite lava flow is found to the south of Cerro Humeras. The rhyolite is vitrophyric with the flow banding striking north. The northern margin, is vertically flow banded and the contact is sharp against volcanic basement rocks, which could possibly represent the feeder dike. The lava flow unconformably overlies a 2 meters-thick sedimentary rock unit with very fine, parallel-laminated mudstone in the upper 30 centimeters of the section. Soft-sediment deformation textures are observed at the contact with the lava flow, and beds are locally tilted by as much as 90°. This sedimentary rock section correlates with volcaniclastic rocks that widely outcrop in South El Dorado.

2.5.5.5 Upper volcaniclastic sequence

The second main group of Pliocene felsic volcanic rocks in the El Dorado district consists of pyroclastic and volcanogenic sedimentary rocks, referred to as the upper

volcaniclastic sequence. These rocks are found extensively to the south of the Titihuappa River where they form a section in excess of 100 meters, and to the west of the Cerro Caballo lava dome and flow complex, where they reach up to about 70 meters in thickness. The sequence is characterized by welded and unwelded tuffs to lapilli-tuffs of felsic composition interbedded with parallel- to cross-laminated tuffaceous sandstone, siltstone and mudstone. Conglomerates containing abundant mafic clasts are locally found within the dominantly felsic sedimentary rock sequence (Figure 2.6b). Rocks of the upper volcaniclastic sequence are distinguished by the ubiquitous presence of biotite.

The base of the upper volcaniclastic sequence locally includes a fragment supported pyroclastic breccia that yielded a mean weighted ^{40}Ar-^{39}Ar plateau age of 3.93 ± 0.17 Ma on biotite phenocrysts (Figure 2.3, l and m; Table 2.1). The breccia unit is included on the detailed geological map, but is not shown on the simplified map where it forms part of the broad upper volcaniclastic sequence. The breccia contains 50% to over 75% flow-banded, poorly vesicular rhyolite clasts that range in size from less than 1 cm to slightly over 1 meter across (Figure 2.6c). Sub-rounded andesite fragments up to ~5 cm across represent less than 2% of the breccia, and the matrix is a mixture of ash with quartz and biotite crystal fragments. The breccia unit is mainly distributed along the San Francisco River, where it forms steep walls up to 35 meters high. In the El Gallardo sinters area, it is locally found in direct depositional contact with sinters, and appears to thin and disappear to the north. South of the Titihuappa River, the breccia is found in isolated outcrops at the base of the stratigraphic section, roughly 100 meters below the base of the unit in the El Gallardo area. This offset is possibly associated with southward dip-slip along the east-striking Titihuappa fault zone (see below). The bottom of the unit does not crop out south of the River where the thickness of the unit may only be estimated to at least 35 meters (San Francisco River section). South of the Titihuappa River, the top of the breccia is normally graded, sub-horizontally laminated and contains abundant petrified wood fragments. The breccia fragments display a radial fracture pattern that appear similar to those described by Mann et al. (2004) at Ilopango Caldera, where the unit was emplaced and cooled in a sub-aqueous environment. Directly overlying this outcrop is a 1-2 meter thick bed of finely laminated siltstone and mudstone, very similar to the section found south of Cerro Humeras where it is overlain

by a rhyolite lava flow (see previous section). A 115 meters elevation difference separates these two sedimentary rocks sections. Assuming the two sections correlate, this elevation difference provides a minimum estimate of displacement along the Titihuappa fault zone (see below). It also provides a constraint on the timing of displacement along the fault, which must post-date the age of the pyroclastic breccia (3.93 ± 0.17 Ma).

South of the Titihuappa River, the upper volcaniclastic sequence is in excess of 100 meters-thick and is capped by a welded hornblende-phyric dacite tuff that contains approximately 5% fiamme with aspect ratio of 2:1 to 5:1. The welded tuff forms a scarp in excess of 20 meters that roughly follows the orientation of the Titihuappa River. The plains south of the River are widely covered by felsic pyroclastic and sedimentary rocks where they appear to have accumulated in the Pliocene Rio Titihuappa basin, which could potentially represent a volcano-tectonic depression (see below). The Miocene volcanic basement rocks are presumed to be present at depth, beneath the Pliocene cover.

In the El Gallardo sinters and Cerro Volcancillo areas (Figure 2.4), pyroclastic and sedimentary rocks at the base of the upper volcaniclastic sequence are locally veined, silicified and intercalated with sinters providing constraints on the timing of hydrothermal activity in the district (see below).

2.5.6 Post-mineral lava flows

At the district scale, the uppermost stratigraphic unit consists of basaltic to andesitic lava flows that are mainly found to the north and south of the town of San Isidro (Figure 2.4). Next to the Titihuappa River, deposits of the upper volcaniclastic sequence are locally overlain by columnar jointed basaltic lava flows. Soft-sediment load deformation textures are found in the underlying sedimentary rocks, suggesting that the volcaniclastic deposits were poorly consolidated and possibly water-saturated at the time the lava flow was emplaced (Figure 2.6d). The lava flow in this area was dated using plagioclase, yielding a geologically impossible ^{40}Ar-^{39}Ar plateau age of 10.8 ± 1.9 Ma (Figure 2.3n; table 2.1), possibly due to excess argon (T. Ullrich, pers. comm., 2006). The lava flows must be younger than the underlying volcaniclastic rocks, but likely has a similar age (Pliocene) since the sedimentary deposits were poorly consolidated at the time the lava flow was emplaced.

2.6 Structural Geology

Two predominant regional fault systems characterize the structural geology of El Salvador. One system strikes northwest and is associated with subsidiary northeast striking faults. The other set is east-striking with subsidiary north-striking faults. Northwest striking faults are the prominent faults and may be traced for distances up to 180 km across the country, cutting the east-striking set of faults. The east-striking faults commonly form *en echelon* grabens offset by 20-30 kms along northwest striking faults (Wiesemann, 1975). Such grabens form the interior valley of El Salvador characterized by heterogeneous basins hosting extinct volcanic edifices of Pliocene to Pleistocene age. The El Dorado district is located on the northeastern edge of the Rio Titihuappa basin (Weyl, 1980), where its north bounding normal fault strikes almost due east. The Rio Titihuappa basin is one of four major Pliocene basins in El Salvador (Olomega, Rio Titihuappa, Rio Lempa, and Metapan basins), that align in a northwest orientation following the prominent NW-striking fault system mentioned above (Figure 2.7). The Pliocene basins are generally larger but comparable in size to Quaternary calderas (Coatepeque and Ilopango) that formed along the modern volcanic arc (Figure 2.7).

A complex pattern of faults, fractures and veins are observed in the El Dorado district, following the regional trends. Three main structural domains are observed, represented by North, Central and South El Dorado. In North El Dorado, the dominant veins (San Matias, Coyotera) strike between N20°E and N35°E. In Central El Dorado, most veins strike between N25°W and N25°E, with the principal resource veins (Minita vein system) striking due-north. In South El Dorado, the main structural domain is defined by northwest striking veins. Two major fault zones that appear to have controlled the spatial distribution of volcanic rocks will be briefly described in the following section.

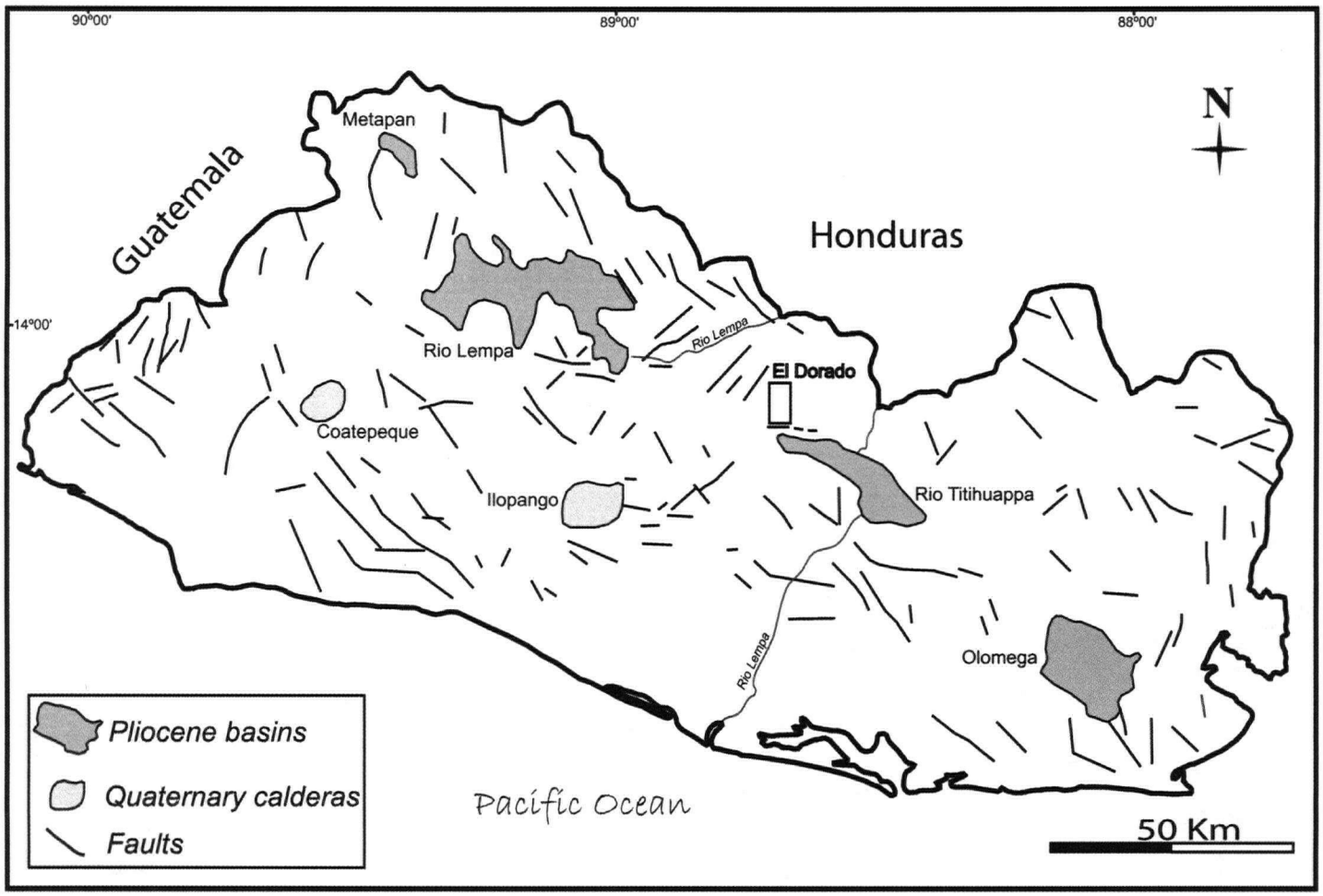

Figure 2.7. Simplified structural geology map of El Salvador modified from Weyl (1980) showing the location of four Pliocene basins (Olomega, Rio Titihuappa, Rio Lempa, and Metapan) and Quaternary calderas (Coatepeque and Ilopango). The Rio Titihuappa basin is found directly southeast of the El Dorado district. The Titihuappa River, an east-striking normal fault zone on the extreme south of the district, may define the northwestern margin of the Titihuappa basin. The Rio Titihuappa basin possibly represent a volcano-tectonic depression.

2.6.1 Titihuappa fault zone

At the southern edge of the district, the Titihuappa River follows a regional east-striking normal fault zone that possibly accommodated over 115 meters of vertical displacement (based on the elevation difference between two correlated siltstone and mudstone sections; see above). Displacement along the fault must post-date 3.93 ± 0.17 Ma, the age of the pyroclastic breccia underlying the siltstone and mudstone section south of the Titihuappa River. A west-northwest striking set of normal faults bordering the southern flank of the Plan de Minas area, with dip-slip to the south, could have formed in conjunction with the Titihuappa fault zone.

At the district and regional scale, the river traces an important boundary in the volcanic stratigraphy, separating Miocene volcanic basement rocks to the north from extensive Pliocene felsic pyroclastic and sedimentary rocks to the south (forming part of the upper volcaniclastic sequence described above). The general east-west distribution of rhyolite plugs and domes close to the Titihuappa River also supports the idea of a major fault zone potentially controlling the emplacement of sub-volcanic intrusive rocks. The Titihuappa fault zone potentially represents the margin of a Pliocene volcano-tectonic depression that downdropped the volcanic basement rocks to the south, and controlled the accumulation of pyroclastic and sedimentary rocks. The inferred volcano-tectonic depression possibly represents the northeastern limit of the Rio Titihuappa basin.

2.6.2 El Gallardo fault zone

A north-northwest-striking, syn- to post-mineral normal fault system, referred to as the El Gallardo fault zone, extends from the northern end of the Hacienda vein along the San Francisco River to the junction with the Titihuappa River. This fault zone could form a subsidiary set to the east-striking Titihuappa fault zone. It is composed of a series of sub-parallel, steeply west-dipping (60° to 80°) normal faults, that incrementally down-dropped the andesite basement, the overlying upper volcaniclastic sequence and the sinters to the west as schematically illustrated on Figure 2.8a (see below). The vertical displacement in the proximity of the El Gallardo sinters may be estimated at 40-50 meters, based on the elevation difference between the andesite basement on either sides of the fault zone in the Hacienda vein area (Figure 2.4). The southern extension of the El Gallardo fault zone follows the western margin of the South Gallardo rhyolite dome (see

above), where the ~170°-striking normal fault dips 65-70° to the west. Grove marks on the fault plane have a rake of 85°-south indicating normal slip with minor lateral displacement. Volcanic basement rocks do not outcrop west of the fault along the San Francisco River, where a pyroclastic breccia accumulated (see above). Vertical displacement in this area could be a minimum of 55 meters, based on the elevation difference between the volcanic basement rocks and the river bed east and west of the rhyolite dome respectively (Figure 2.4). The vertical displacement arguably increases from nearly absent along its northern extension to over 55 meters at the southern end where it intersects the Titihuappa fault zone, potentially defining a relay ramp (Peacock, 2002).

The Hacienda vein, adjacent to the fault zone on its eastern side, is mainly hosted by the andesite basement and closely follows the fault contact with the upper volcaniclastic sequence. Horizontal zones or "lenses" of silicification extend laterally into tuffaceous sandstones and siltstones to the west of the vein. The uppermost pyroclastic rocks forming part of the upper volcaniclastic sequence are not veined or silicified. Displacement along the fault may have been incremental, contemporaneous with the deposition of volcaniclastic rocks and near-surface hydrothermal activity.

The El Gallardo fault zone thus represents an important boundary in the volcanic stratigraphy: deposits of the upper volcaniclastic sequence are found extensively to the west, where they reach at least 70 meters in thickness. To the east of the fault zone, only veneers of the upper volcaniclastic sequence are preserved. At the district scale, sinters are found strictly west of the El Gallardo fault zone and Hacienda vein, where they are intercalated with rocks at the base of the upper volcaniclastic sequence. The fault zone appears to define a half-graben that confined the deposition of volcaniclastic deposits and controlled the hydrothermal flow gradient.

2.7 Veins and sinters

Detailed information on vein mineralogy and paragenesis can be found in Hudson et al. (2005), and much of the following is based on that study. Over one thousand veins have been mapped in the El Dorado district and vary in width from a few centimeters to over 15 meters, and in strike length from a few meters to over 1500 meters (Figure 2.4).

In Central and North El Dorado, veins crop out at the surface at elevations between ~400-600 meters above sea level, and have over 400 meters of vertical extent as revealed by drilling. In South El Dorado, veins and sinters are found at elevations varying between 250-450 meters above sea level.

Veins are generally crustiform banded to breccia, with less frequent colloform to cockade banding, and have multiple axes of deposition. Textural characteristics may vary remarkably along strike. Primary quartz, or quartz recrystallized from chalcedony, is the most common gange mineral, with lesser amounts of calcite and adularia. Minor amounts of clays are found in veins including montmorillonite at shallow depth, light green corrensite at intermediate levels and dark green nontronite in the deeper portions of the veins. Corrensite is locally associated with higher grade zones.

Sulfides and other ore minerals constitute a very small portion of the veins. In approximate order of decreasing abundance, those include chalcopyrite, pyrite, acanthite, covellite, gold, galena, sphalerite, and chalcocite (Hudson et al., 2005). These minerals are usually very small (a few μm) and occur as independent grains or as intergrowth of one another, with precious and base metals occurring together in the same band. Ore minerals occur in distinct bands or may be disseminated across a given zone. Adularia-rich bands have been observed to contain the most ore minerals. The highest gold grades occur in a well defined horizon at approximately 200 meters above sea level. The abundance of adularia and the presence of bladed calcite suggest that boiling may have been the primary mechanism for the deposition of gold. Base metals are typically very low in abundance and do not show any systematic zonation within a vein with depth.

A range of ages were obtained from vein adularia in Central El Dorado, including K-Ar ages of 4.7 ± 0.2 Ma and 3.6 ± 0.4 Ma (F. McDowell, written comm., 2006). These ages generally agree with replicate analyses obtained on one vein adularia sample from the current study, with plateau ages of (1) 4.06 ± 0.29 Ma, (2) 3.49 ± 0.58 Ma, and (3) 4.31 ± 0.19 Ma (Figure 3p, q, and r; Table 2.1). The second analysis produced a very poorly constrained plateau, possibly as a result of the low volume of the sample and the presence of contaminants (e.g., calcite) which may have increased the Ca/K ratio (T. Ullrich, written comm., 2006). This analysis was not considered statistically valid. The first and third runs produced better constrained plateaus, and were accepted as

statistically valid ages. A further constraint on the age of vein formation is provided by the stratigraphic position of the El Gallardo sinters.

In the southwest area of the district, mapped sinters follow a broad north-northwest distribution to the west of the north to north-northwest striking Hacienda vein and El Gallardo fault zone (Figure 2.4). The sinters contain anomalous gold and are found intercalated at the base of the upper volcaniclastic sequence (Figure 2.8a), defining the paleosurface of the El Dorado epithermal veins system. Directly below the El Gallardo sinters, the volcanic basement rocks are cross-cut by vein stockworks (Figure 2.8b). Plant fossils were locally observed in the El Gallardo sinters (Figure 2.8c), providing evidence of their formation at the surface. Locally, at the top of a sinter, flow-banded pyroclastic fragments are cemented in opaline silica (Figure 2.8d). The rock fragments have been pervasively silicified, but possibly belong to the overlying pyroclastic breccia (see above). East of the El Gallardo sinters, a 10-15 meters-thick silicified zone is observed in volcaniclastic rocks directly above the volcanic basement rocks. The zone consists of massive to banded silicified horizons up to 3-m-thick, interlayered with 1-50 cm-thick kaolinitized rhyolite beds (Figure 2.8e). Directly above the interlayered silica and rhyolite section, the rock consists of pervasively silicified, fragment supported heterolithic breccia overlain by weakly to pervasively silicified, parallel to cross-laminated, tuffaceous sandstone to siltstone forming part of the upper volcaniclastic sequence. The sedimentary rock section is locally interbedded with thin beds of finely laminated opaline silica that may represent silica oozes, or delicate replacement of the porous tuffaceous rocks. This continuous section has been interpreted to represent a hydrothermal pool or vent, which formed in conjunction with the accumulation of tuffaceous sediments.

The sinters have not been directly dated due to the lack of datable minerals. Their relative age is constrained by the mean weighted ^{40}Ar-^{39}Ar plateau age obtained on biotite phenocrysts from the pyroclastic breccia unit found in depositional contact with the El Gallardo sinters (3.93 ± 0.17 Ma; see above). This provides an age bracket on mineralization assuming that the sinters are related to the formation of epithermal veins in the sub-surface. Given the well established stratigraphic position of the pyroclastic breccia with respect to sinters (hence mineralization), the K-Ar age of 3.6 ± 0.4 Ma age

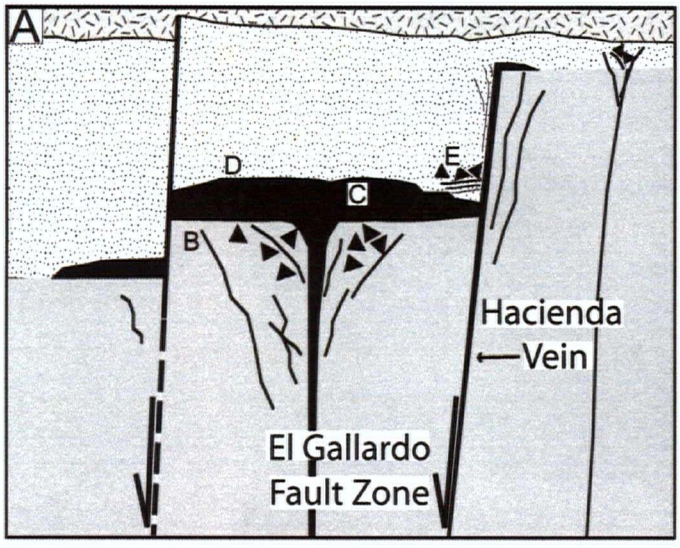

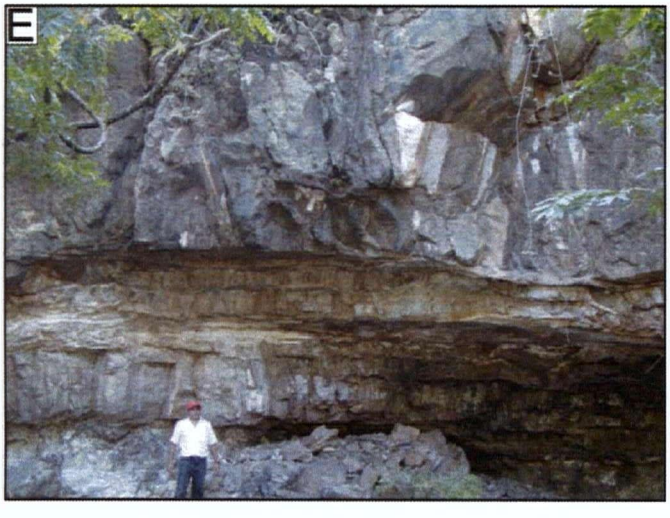

Figure 2.8. A) Schematic stratigraphic column representating the relationship between volcanic rocks and veins and sinters of the El Gallardo area. Rock units correspond to the patterns on the geological map (Figure 2.4). The photo plates demonstrate some of the field observations with their respective position on the diagram indicated by the corresponding letters. B) Vein stockwork hosted in volcanic basement rocks. C) Remanants of plant fossils in massive chalcedony sinter. D) Pervasively silicified pyroclastic rock fragments and cemented in opaline silica at the top of a sinter. E) Intercalated massive to brecciated replacement silica, and kaolinitized rhyolite horizons.

obtained on adularia by F. McDowell is rejected (see above). Accordingly, vein formation and mineralization in the El Dorado district is constrained between 4.7 ± 0.2 Ma to 4.06 ± 0.29 Ma, probably closer to the lower limit in agreement with the age of the pyroclastic breccia unit within uncertainties.

Hydrothermal breccias of possible phreatic origin are found in the southeast area of the district (Figure 2.4). Breccias contain flow banded rhyolite fragments, massive to banded chalcedony vein clasts, and hydrothermally altered mafic rock fragments (samples MR04-39 and MR04-60 in appendix B). The breccia cement mainly consist of druzy quartz, with a few percents pore space. The largest breccia body has an elongate, sub-circular outline at the surface, and contained anomalous gold, which was mined at the end of the 19th century (see above). Whether those breccias formed in conjunction with epithermal mineralization is not clear, however, they must post-date the Pliocene rhyolitic volcanic rocks which they cross-cut.

2.8 Summary and discussion

2.8.1 Chronology of volcanic and hydrothermal events

Two main groups of rocks are found in the El Dorado district: Miocene and older (?) dominantly mafic volcanic basement rocks unconformably overlain or cross-cut by dominantly felsic Pliocene volcanic rock sequences. Post-mineral Pliocene to Pleistocene (?) basaltic to andesitic lava flows cap the volcanic sequence and represent a much smaller eruption volume relative to felsic rock units. Based on argon geochronology of major stratigraphic units and limited veins samples, a ~5 m.y. time gap exists between the emplacement of the youngest volcanic basement rocks (10.7 ± 1.9 Ma based on the age obtained on a porphyritic andesite dome sample), and the unconformably overlying/cross-cutting volcanic rocks and epithermal veins (Figure 2.3; Table 2.1). Figure 2.9 schematically represents the volcanic and mineralization events in chronological order as constrained by field observations and geochronology.

The ages of emplacement of the Plan de Minas volcaniclastic rock sequence and the Cerro Caballo dome complex are not constrained by geochronology, although both units are cross-cut by veins, and must therefore pre-date mineralization. Based on the age of epithermal veins (4.7 ± 0.2 Ma to 4.06 ± 0.29 Ma), the Cerro Caballo dome complex

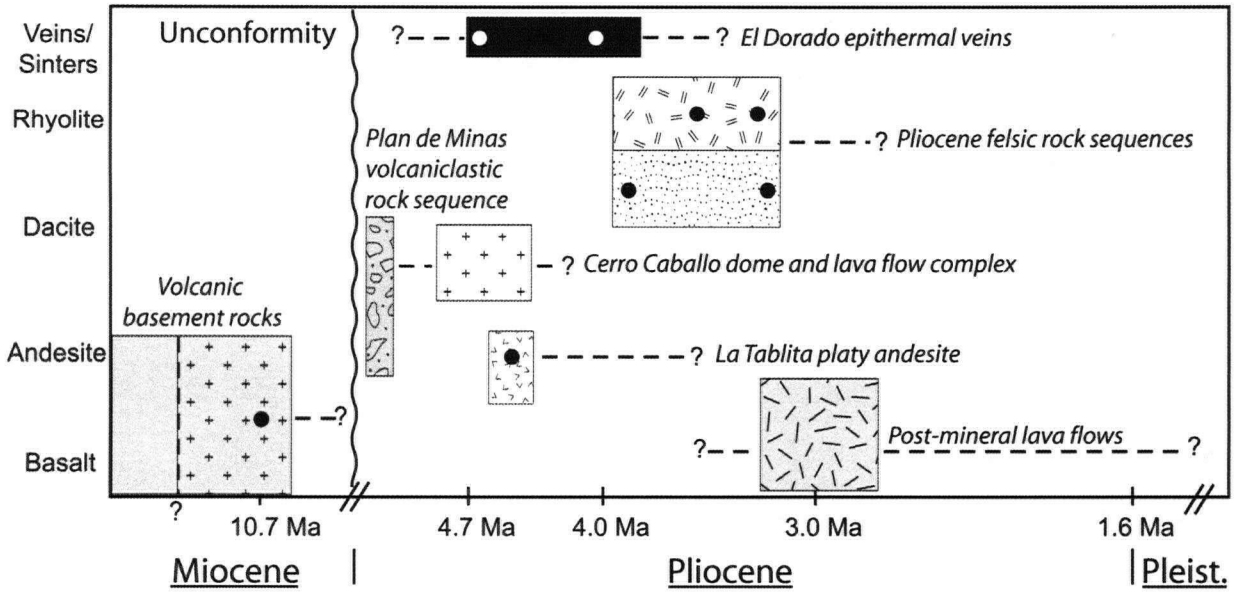

Figure 2.9. Time-event chart displaying the relative timing of volcanic activity and vein formation according to argon geochronology. The vertical axis represents the overall composition of the major rock units. Fill patterns are the same as those on the geological map. Time range of boxes include uncertainties on argon ages for each rock unit. The dots represent rock units constrained by geochronology.

and the Plan de Minas volcaniclastic rock sequence are assumed to have been emplaced during the early Pliocene (Figure 2.9), or possibly during the late Miocene. Upcoming dating of the Cerro Caballo dome rock will clarify the sequence of events.

The timing of emplacement of Pliocene andesite lava flows referred to as "La Tablita platy andesite" remains ambiguous. The age of the lava flow in Central El Dorado is constrained by a plateau age of 4.63 ± 0.37 Ma on a plagioclase separate. Similar outcrops of platy andesites were found in South El Dorado and were dated at 4.57 ± 0.74 Ma also based on plagioclase separates. These lava flows do not host any veins at the surface and do not show signs of hydrothermal alteration despite their overlapping age with that of epithermal veins. Assuming that the age obtained on platy andesites is correct, they would provide an age bracket to veining in the district: veins would have formed prior to 4.63 ± 0.37 Ma. However, the more robust age obtained on biotite from the pyroclastic breccia above the El Gallardo sinters indicates that surface hydrothermal activity may have lasted until about 3.93 ± 0.17 Ma. Platy andesites may therefore have been emplaced after mineralization, and the age obtained by argon geochronology on plagioclase may be slightly older than the actual age of the lava flows. A minimum age for the La Tablita platy andesite is provided by the cross-cutting Cerro Avila dacite dome dated at 3.62 ± 0.08 Ma. The platy andesites were likely emplaced in the stratigraphic sequence between 3.93 ± 0.17 Ma and 3.62 ± 0.08 Ma (Figure 2.9).

Two main groups of felsic volcanic rocks were identified in the district: coherent dacites and rhyolites (lava domes, dikes, and lava flows) and volcaniclastic rocks (tuffs, lapilli-tuffs and sedimentary rocks mainly derived from pyroclastic material). The two groups likely are temporally related as suggested by field relationships and overlapping radiometric age results within uncertainties. The spatial distribution of facies suggests that the pyroclastic rocks may represent eruption products deposited around and distal to the eruptive centers marked by the domes and plugs. The onset of felsic volcanism is constrained by the oldest age obtained on the pyroclastic breccia unit that directly overlies the El Gallardo sinters (3.93 ± 0.17 Ma). This age corresponds to the upper limit for epithermal mineralization according to argon geochronology of veins from Central El Dorado (4.7 ± 0.2 Ma to 4.06 ± 0.29 Ma). Field observations also support the idea that the onset of felsic volcanism marked the waning stages of hydrothermal activity since the

base of the upper volcaniclastic sequence is widely silicified and veined. Felsic volcanism continued for several hundred thousand years following epithermal mineralization with the emplacement of rhyolite domes, plugs, and lava flows that were dated between 3.6 ± 1.3 Ma and 3.36 ± 0.49 Ma (Figure 2.9). The apparent time gap between the oldest felsic rock unit (pyroclastic breccia; 3.93 ± 0.17 Ma) and second oldest (La Tabla rhyolite lava flow; 3.6 ± 1.3 Ma) may be a sampling artifact or may reflect the cyclicity of felsic volcanism between ~4 Ma and ~3.3 Ma. Long-lived compositionally evolved magmatic systems commonly have long repose periods between eruptive cycles (e.g., Bailey et al., 1976). Alternatively, Pliocene felsic volcanism may have been associated with distinct pulses of magmatic activity (e.g., Simon and Reida, 2005).

Basaltic to andesitic lava flows were part of the last eruptive events to occur in the district. One argon plateau age was obtained on a plagioclase separate from a basaltic lava flow in South El Dorado. The poorly constrained age of 10.8 ± 1.9 Ma is not geologically significant, since the lava flow overlies felsic volcaniclastic rocks of Pliocene age. This particular basaltic lava flow must be of similar age (Pliocene) to the felsic volcaniclastic rocks. This interpretation is based on load deformation textures observed at the base of the lava flow suggesting that the volcaniclastic deposits were poorly consolidated at the time the lava flow was emplaced. Other post-mineral basaltic to andesitic lava flows in the district could have been emplaced subsequent to felsic volcanism, and could even be of Pleistocene age (Figure 2.9).

2.8.2 A potential volcano-tectonic depression?

The topographic gradient (high to low from north to south, with over 400 meters elevation difference), and the general shallowing of the stratigraphic sequence and epithermal vein system to the south suggest that the entire district may have been tilted and/or downdropped southward possibly during and/or after epithermal vein formation. Figure 2.10 schematically represents the distribution of volcanic facies at the surface and their interpreted relationships at depth following a NNE- SSW cross-section across the district (represented by dashed line A-A' on Figure 2.4).

South of the Titihuappa fault zone, in the south-central and south-western parts of the district, the volcanic basement rocks do not outcrop, and are overlain by a >100

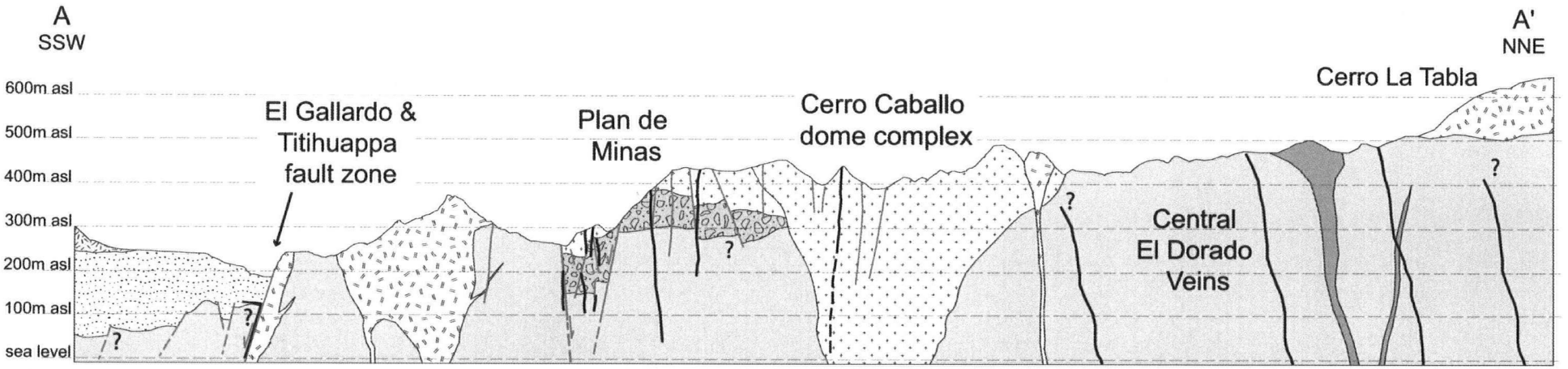

Figure 2.10. Cross-section of the El Dorado district drawn across the A-A' line on the district map (Figure 2.4). Vertical exaggeration x2. See geological map for rock units legend.

meters-thick sequence of Pliocene pyroclastic and sedimentary rocks (the upper volcaniclastic sequence), as schematically illustrated on the SSW end of the cross-section. Deposits of the upper volcaniclastic sequence are found extensively to the west of the El Gallardo fault zone where they are intercalated with sinters and silica replacement horizons at the base of the sequence. The Titihuappa and El Gallardo fault zones appear to have down-dropped the volcanic basement rocks to the south and west, respectively, controlled the deposition of volcaniclastic rocks and possibly the hydrothermal flow gradient associated with the epithermal vein system. The distribution of volcaniclastic rocks and normal faults potentially define the margin of a volcano-tectonic depression limited by the Titihuappa fault zone in the vicinity of the El Dorado district. The Pliocene Rio Titihuappa basin found to the southeast of the district (Weyl, 1980), could form part of the inferred volcano-tectonic depression. Deposits of the upper volcaniclastic sequence covering the plains south of the Titihuappa River may partly represent caldera-fill as illustrated on Figure 2.10.

Rhyolite domes and plugs are generally found bordering the Titihuappa River (Figure 2.4, 2.10). The Titihuappa fault zone may have controlled the near surface emplacement of felsic intrusive rocks, the domes being analogous to ring-dike intrusions (Smith and Bailey, 1968).

In the Plan de Minas area, post-mineral normal faults were identified and extended at depth as constrained by drilling (Figure 2.10). The faults downdropped the Plan de Minas volcaniclastic sequence and overlying lava flows to the south by approximately 100 meters. This fault zone may have been active in conjunction with the Titihuappa fault zone during the formation of the inferred volcano-tectonic depression.

The productive ore zone in the Central part of the district was found to be at 200 meters above sea level as revealed by exploration drilling, and interpreted to reflect the level at which fluid boiling and gold deposition occurred (Hudson et al., 2005). When projecting the Minita vein on a north-south longitudinal section, the ore shoot was found to smoothly deepen to the south, possibly associated with the hydrological dynamics of the epithermal veins system. Alternatively, the deepening of the productive ore zone could reflect southward tilting of the district associated with tectonic processes that affected the whole region during the Pliocene. Weyl (1980) argues that the uplift of large

parts of Central America to their present heights is largely due to late Tertiary and Quaternary tectonic processes. Rogers et al. (2002) argued that the uplift of northern Central America is the buoyant upper-plate response to a slab detachment event and subsequent influx of mantle asthenosphere during the late Tertiary. It is likely that the El Dorado district was affected by such tectonic processes during the Pliocene. Does the uplift coincide with the formation of the Rio Titihuappa basin? One cannot rule out the possibility that tectonic movements may have been accompanied with caldera formation, hence producing a volcano-tectonic depression.

2.8.3 Regional classification

One of the objectives of this research project was to establish correlations between district and regional scale stratigraphic sequences. Broad correlations may be made between the El Dorado district volcanic rocks and regional rock Formations of El Salvador, however, due to the complexity of the volcanic environment and facies variations, forcing the district scale volcanic stratigraphy into a pre-established regional classification scheme must be taken with caution. Misleading correlations and age assignments may result as was the case of the El Dorado district prior to the detailed field work and geochronology presented here.

As an example, the mineralized mid-Miocene mafic to intermediate volcanic basement rocks at the El Limon and Cerro Mojon mining districts in Nicaragua were classified as the base of the Coyol Group (Malone and Stoiber, 1987; Johnson et al., 2001), the equivalent of the Miocene Chalatenango Formation of El Salvador. The Chalatenango Formation has been described as extensive felsic volcanic rocks including ignimbrites, lava flows and domes (Reynolds, 1980). The criteria to correlate the volcanic basement rocks at El Limon and Cerro Mojon with the Chalatenango Formation are therefore not justified in El Salvador. The basement rocks of the El Dorado district, including the lower lava sequence and the late Miocene porphyritic domes and dikes, likely correlate with the Miocene basement rocks at the Cerro Mojon and El Limon mining districts. However, the basement rocks of the El Dorado district are more appropriately correlated with the Morazan Formation, and not the Chalatenango Formation. Although the time stratigraphic correlation can not confidently be demonstrated by field mapping, the general facies descriptions and compositional ranges

are similar (compare Figures 2.2 and 2.5). When correlating the volcanic framework of different mining districts (e.g., El Dorado vs. El Limon/Cerro Mojon, Nicaragua), local stratigraphic units are easier to compare in terms of composition and facies association, and where ages are available, the stratigraphic correlation can be confirmed with confidence. This provides an example of the difficulties encountered when forcing the complex district-scale stratigraphy into regional groups, where important facies information can be lost into broad descriptions. Nonetheless, an attempt will be made to classify the El Dorado district volcanic stratigraphy into the El Salvador regional classification scheme (see Figure 2.2).

The La Tablita platy andesite that unconformably overlies the porphyritic dikes and domes in Central El Dorado could be grouped with the Balsamo Formation according to the regional volcanic framework. Andesitic lavas of Pliocene age have been described in Guatemala and grouped with this Formation (e.g., Reynolds, 1980). It is not apparent if other rock units in the district correlate with the Balsamo Formation.

Prior to this research study, the felsic volcanic rock sequences had been classified as part of the Miocene Chalatenango Formation (Dayton Mining Corp. Feasibility Study, 2001), based on limited geochronology of apparently correlative rocks in adjacent countries (e.g., Reynolds, 1980). The felsic volcanic rocks at El Dorado, including domes, plugs, lava flows, and volcaniclastic rocks, yielded Pliocene ages do not correlate with the Miocene ignimbrites of Guatemala, Honduras and Nicaragua. The latter are distinctly older and no rock units equivalent to the Chalatenango Formation were identified in the El Dorado district. The Pliocene felsic volcanic rocks of the El Dorado district are thus best classified into the Cuscatlan Formation, which includes rhyolite tuffs and volcanogenic sedimentary rocks overlain by rhyolitic and basaltic lava flows (Reynolds, 1980). Mineralization at the El Dorado district may thus have preceded and partly occurred in conjunction with the deposition of Pliocene volcanic rocks forming part of the Balsamo and Cuscatlan Formations.

There might be many reasons as to why the felsic products of the Miocene Chalatenango are not found in the district. The accumulation of ignimbrites may have been controlled by valley systems that did not extend into the area, or they simply have not been preserved due to erosion. The source of the Miocene ignimbrites may also have

been distal to the district, possibly farther inland. It is interesting at this point to introduce again the idea of a shift in subduction and magmatic activity during the Tertiary.

2.8.4 Linking tectonic, magmatic and metallogenic events

The El Dorado district is found at a regional boundary in the regional stratigraphy: Miocene and older volcanic rocks are found to the north of the Titihuappa River (at the district scale), whereas Pliocene volcanic rocks are found extensively to the south. The regional distribution of volcanic rocks suggests that a trenchward shift in magmatic activity occurred during the Miocene to Pliocene transition (Weyl, 1980; see Figure 2.1). The Miocene and Pliocene volcanic rocks thus represent distinct magmatic events. At the district scale, Miocene and older volcanic rocks are dominantly mafic in composition and were derived from "dry" magmas (they contain no hydrous mineral phases) whereas Pliocene volcanic rocks are dominantly felsic in composition and were derived from hydrous magmas (hornblende and biotite are the main mafic mineral phases). A low differential stress regime during the Pliocene may have allowed felsic magmas to pond and form magma chambers at mid- to upper-crustal levels (Takada, 1994). The dacitic Cerro Caballo dome complex, cut by gold-bearing veins, marks the onset of hydrous and more evolved volcanism in the district. It is possible that the evolving magmatic plumbing system associated with the Cerro Caballo dome complex and subsequent Pliocene felsic volcanic rocks also represented the critical heat engine to the hydrothermal system and a possible source of brines and precious metals. It is improbable that near-surface felsic volcanic activity was the driving mechanism to the hydrothermal system: the heat source was likely distal (deep) relative to the district given the type of epithermal deposit (Heald et al., 1987). Field observations and geochronology indeed support the idea that the onset of felsic volcanism occurred in conjunction with the waning stages of hydrothermal activity associated with epithermal vein formation (see above). Extensive volcanism associated with the evolving magma chambers during the period ~4.0-3.3 Ma thus potentially lead to caldera collapse and suppression of the near-surface hydrothermal activity.

The time span of hydrothermal activity associated with epithermal vein formation at El Dorado is poorly constrained. Different age results, with over one million year difference considering uncertainties, were obtained on one vein sample from the current

study (4.06 ± 0.29 Ma, 3.49 ± 0.58 Ma and 4.31 ± 0.19 Ma; see Figure 2.3o, p, and q). Sample impurities and small volume sample likely affected the results (T. Ullrich, pers. comm., 2006). Contrasting ages on two adularia vein samples from Central El Dorado were produced by F. McDowell (written comm., 2006), and likely encountered similar analytical problems. Considering field relationships and geochronology, epithermal vein formation is constrained between 4.7 ± 0.2 Ma and 4.06 ± 0.29 Ma, but likely occurred closer to the younger limit (in agreement with the more robust plateau age obtained on biotite from the pyroclastic breccia unit found in depositional contact with the El Gallardo sinters). Hydrothermal activity associated with epithermal vein formation commonly occurs over relatively short periods of time, well under 0.5 m.y. according to Henry et al. (1997). Hydrothermal activity at El Dorado may have lasted for a few hundred thousand years or much less, with gold being brought into the hydrothermal system during discrete pulses, possibly in association with the evolving Pliocene magmatic system found at deeper crustal levels. The idea that vein emplacement may have occurred during more than one hydrothermal event was treated by Hudson et al. (2005). Barren low-temperature silica veins and wall-rock silicification commonly overprint early mineralized veins at depth (sample MR04-95 in Appendix B). A detailed paragenesis study and additional dating of veins, and volcanic rocks would be needed in order to understand the complexity of epithermal mineralization at El Dorado.

2.9 Conclusion

In light of the recent field mapping and new isotopic dating results, it is possible to place the volcanic rocks of the El Dorado district into a well constrained time-stratigraphic framework. The El Dorado district includes two main groups of volcanic rocks separated by a ~5 m.y. time unconformity: dominantly mafic to intermediate Miocene and older volcanic basement rocks unconformably overlain by mafic to dominantly felsic Pliocene volcanic rock sequences. The volcanic basement rocks include a lower lava flows and sedimentary rock sequence that was intruded by porphyritic domes and dikes during the late Miocene. These rocks form the principal host to gold-bearing epithermal veins and petrologically correlate with rocks of the Morazan Formation of El Salvador. The epithermal vein system formed during the early Pliocene and immediately preceded a period of widespread felsic volcanism. The onset of felsic volcanism in the district appears to coincide with the waning stages of mineralization as suggested by field observations and geochronology, and continued for several hundred thousand years following vein formation. The evolved magmatic plumbing system associated with the Pliocene volcanic rock sequences may have represented the heat engine driving the once active hydrothermal system related to epithermal vein formation and mineralization in the district. The source or exact timing of gold mineralization remains unknown. Extensive volcanism associated with the compositionally evolved Pliocene magmatic system potentially lead to the formation of a volcano-tectonic depression and suppression of the near-surface hydrothermal activity. The Titihuappa River (fault zone) on the extreme south defines the northwestern margin of the inferred volcano-tectonic depression, possibly forming part of the larger Pliocene Rio Titihuappa basin extending to the southeast of the district.

The El Dorado district epithermal veins system is younger than previously considered. Gold-bearing epithermal vein systems of Pliocene age may be common elsewhere in El Salvador or in adjacent countries, although the lack of detailed geochronology only allow speculations concerning the extent of the metallogenic event along the convergent plate margin. Future exploration and academic research will hopefully elucidate further the volcanic history, and the tectonic and metallogenic evolution of the Central American region.

2.10 References

Annen, C., Blundy, J.D., and Sparks, S.J., 2006, The genesis of intermediate and silicic magmas in deep crustal hot zones, Journal of Petrology, vol. 47, p. 505-539.

Bailey, R.A., Dalrymple, G.B., and Lanphere, M.A., 1976, Volcanism, structure, and geochronology of Long Valley caldera, Mono County, California, Journal of Geophysical Research, vol. 81, p. 725-744.

Baxter, S., 1984, Lexico Estratigrafico de El Salvador, Programa "Exploracion de hidrocarburo en El Salvador", Superintendencia de energia, comision ejecutiva hidroelectrica del Rio Lempa, San Salvador, El Salvador, 108 pp.

B.f.B., 1974, Mapa Geologico de la Republica de El Salvador 1:500,000, published by the Bundesanstalt für Bodenforschung, Hannover 1974.

Catastro e inventario de recursos naturales, 1972, Geology of Western Nicaragua, Operations consultant's final report for 1968-1970 surveys, vol. 4, 221 p.

Curran, H., Geological Report on the El Porvenir area, El Dorado exploration concession, Dept. of Cabanas, El Salvador, March 1975.

Dayton Mining Corporation, Kinross El Salvador, S.A. de C.V., Feasibility Study El Dorado Gold and Silver Project El Salvador, July 2001.

Everett, J.R., and Fakundiny, R.H., 1976, Structural geology of El Rosario and Comayagua quadrangles, Honduras, Central America, Publicaciones Geologicas del ICAITI, no.5, p. 31-42.

Heald, P., Foley, N.K., and Hayba, D.O., 1987, Comparative anatomy of volcanic-hosted epithermal deposits: acid-sulfate and adularia-sericite types, Economic Geology, vol. 82, p. 1-26.

Henry, C.D., 1997, Recent progress in understanding caldera development and mineralization in the southern Toquima Range near Round Mountain, Nevada, Special Publication-Geological Society of Nevada, vol. 26, p. 241-246.

Henry, C.D., Elson, H.B., McIntosh, W.C., Heizler, M.T., and Castor, S.B., 1997, Brief duration of hydrothermal activity at Round Mountain, Nevada, determined from $^{40}Ar/^{39}Ar$ geochronology, Economic Geology, vol. 92, p. 807-826.

Hudson, D.M., Richer, M., Gehlen, W.T., 2005, Geology of the El Dorado epithermal vein system, El Salvador, Central America, Proceedings of the Geological Society of Nevada, Symposium 2005, vol. II, p. 723-740.

Johnson, M.D., Bybee, R.W., and Strapko, J.D., 2001, Geology and gold mineralization at the Cerro Mojon Deposit, La Libertad, Nicaragua, Special Publication-Society of Economic Geologists, p. 331-337.

Kesler, S.E., 1978, Metallogenesis of the Caribbean region, Journal of the Geological Society of London, vol. 135, p. 429-441.

Ludwig, K.R 2003. Isoplot 3.09 A Geochronological Toolkit for Microsoft Excel. Berkeley Geochronology Center, Special Publication No. 4.

Malone, G.B. and Soiber, R.B., 1987, Caldera-related gold mineralization of the El Limon mining district, western Nicaragua, Journal of Volcanology and Geothermal Research, vol.33, p. 217-222.

Malouf, S.E. (consulting geologist ltd), 1992, Summary report on New York and El Salvador Mining Company LTD, El Dorado Project.

McBirney, A.R., and Williams, H., 1965, Volcanic history of Nicaragua, University of California Publications in Geological Sciences, vol. 55, 73 pp.

McBirney, A.R., & Weill, D.F., 1966, Rhyolite magmas of Central America, Bulletin of Volcanology, vol. 29, p. 435-446.

Meschede, M., and Frisch, W., 1998, A plate-tectonic model for the Mesozoic and Early Cenozoic history of the Caribbean plate, Tectonophysics, v. 296, p. 269-291.

Peacock, D.C.P., 2002, Propagation, interaction and linkage in normal fault systems, Earth-Science Reviews, vol. 58, p. 121-142.

Pichler, H., and Weyl, R., 1973, Petrochemical aspects of Central American Magmatism, International Journal of Earth Sciences, vol. 62, p. 357-396.

Renne, P.R., Swisher, C.C., III, Deino, A.L., Karner, D.B., Owens, T. and DePaolo, D.J., 1998, Intercalibration of standards, absolute ages and uncertainties in $^{40}Ar/^{39}Ar$ dating. Chemical Geology, vol. 145, p. 117-152.

Reynolds, J.H., 1977, Tertiary Volcanic Stratigraphy of Northern Central America, Master's Thesis, Dartmouth College, Hanover, N.H., 89pp.

Reynolds, J.H., 1980, Late Tertiary Volcanic Stratigraphy of Northern Central America, Bulletin Volcanologique, vol. 43, p. 601-607.

Rogers, R.D., Karason, H., and van der Hilst, R.D., 2002, Epeirogenic uplift above a detached slab in northern Central America, Geology, vol. 30, p. 1031-1034.

Simon, J.I., and Reida, M.R., 2005, The pace of rhyolite differentiation and storage in an archetypical silicic magma system, Long Valley, California, Earth and Planetary Science Letters, vol. 235, p. 123– 140.

Smith, R.L., and Bailey, R.A., 1968, Resurgent cauldrons, Geological Society of America Memoir, vol. 116, p. 613-662.

Takada, A., 1994, The influence of regional stress and magmatic input on styles of monogenetic and polygenetic volcanism, Journal of Geophysical Research, vol. 99, p. 13,563-13,573.

Weyl, R., 1980, Geology of Central America: Berlin-Stuttgart, Gebruder Borntraeger, 371 pp.

Wiesemann, Gerd, 1975, Remarks on the geologic structure of the Republic of El Salvador, Central America, Mitt. Geol. Paläont. Inst. Univ. Hamburg, vol. 44, p. 557-574.

CHAPTER 3

GEOCHEMICAL EVOLUTION OF TERTIARY VOLCANIC ROCKS ALONG THE CARIBBEAN PLATE MARGIN: THE EL DORADO GOLD DISTRICT, EL SALVADOR

3.1 Introduction

The Central American volcanic arc is an excellent area of research for investigating the mantle source composition, magma generation processes, components involved in magma genesis...etc., through geochemical variations of lavas and tephras (e.g., Carr et al. 1990; Patino et al. 2000, Cameron et al., 2002). While most studies have focused on geochemical variations along the arc (e.g., Carr et al., 1990), across the arc to the back-arc (e.g., Walker et al., 2000), or within individual volcanic centers (e.g., Albrecht et al., 2005), very few have focused on the Tertiary volcanic stratigraphy (e.g., Viray, 2003; Lundin et al. 2003). Limited data thus constrains the composition of the Tertiary sub-arc mantle, the components involved during magma genesis and their subsequent emplacement in the continental crust.

Based on the general distribution of volcanic rock formations in Central America, the Miocene to Pliocene transition appears to have been accompanied with a trenchward shift in subduction and associated magmatic activity (Weyl, 1980). Miocene and Pliocene volcanic rocks thus represent distinct Tertiary magmatic events. Are there geochemical similarities or differences between Miocene and Pliocene magmatism? How do Tertiary magma generation processes compare to those identified for the Quaternary volcanic arc?

The El Dorado mining district located in northern El Salvador represents an ideal geological setting to investigate the geochemical evolution between the Miocene and Pliocene magmatic events, with a recently established volcanic stratigraphy constrained by ^{40}Ar-^{39}Ar geochronology. Two compositionally distinct groups of rocks are found in the district: Miocene and possibly older mafic to intermediate volcanic basement rocks, unconformably overlain and cross-cut by Pliocene and possibly younger mafic to dominantly felsic volcanic rocks, with a ~5 m.y. time unconformity separating the two groups. This manuscript describes the lithogeochemistry of the main groups of rocks at El Dorado bringing interpretations concerning magma genesis and processes of geochemical differentiation.

3.2 Geological setting

3.2.1 Regional volcanic stratigraphy

The El Dorado low-sulfidation epithermal veins system located in northern El Salvador is hosted by Tertiary volcanic rocks that cover extensive areas of northern Central America (Figure 3.1). Five Tertiary to Quaternary volcanic rock formations are recognized in northern Central America based on their respective age ranges, spatial distribution, composition and nature of volcanism (Wisemann, 1975; Reynolds, 1980). In El Salvador, these include the Eocene (?) to Miocene Morazan Formation, the Miocene Chalatenango Formation, the late Miocene to Pliocene Balsamo Formation, the Pliocene to Pleistocene Cuscatlan Formation, and the Holocene San Salvador Formation. Figure 3.2a illustrates the relative age and general description of each rock Formation. These volcanic rock sequences accumulated in response to the east to northeastward subduction of the Farallon/Cocos plates beneath the Caribbean plate along the Middle America Trench, and form continuous belts extending from Guatemala to central Costa Rica (Figure 3.1). A general southwestward younging of the volcanic and intrusive rock groups is observed at the regional scale, with the Morazan and Chalatenango Formations found extensively in the highlands of northern Central America, while younger Formations are widely distributed along the Pacific Coast (Figure 3.1). This pattern has been interpreted to reflect a trenchward shift in subduction and magmatic activity during the Miocene to Pliocene transition (Weyl, 1980), possibly as a consequence of slab roll-back and/or due to the relative eastward migration of the Caribbean plate relative to the subducting Cocos/Farallon plates (Meschede and Frisch, 1998). The Miocene and Pliocene volcanic rocks thus represent distinct magmatic events.

3.2.2 El Dorado district volcanic stratigraphy

The oldest and effective volcanic basement rocks at El Dorado include a lower sequence of basaltic to andesitic lava flows and sedimentary rocks that was intruded by porphyritic domes and dikes of similar composition during the late Miocene (10.7 ± 1.9 Ma based on ^{40}Ar-^{39}Ar geochronology on plagioclase). These rocks represent the principal host to the epithermal veins in the district, and petrologically correlate with the Morazan Formation (compare Figure 3.2a and b).

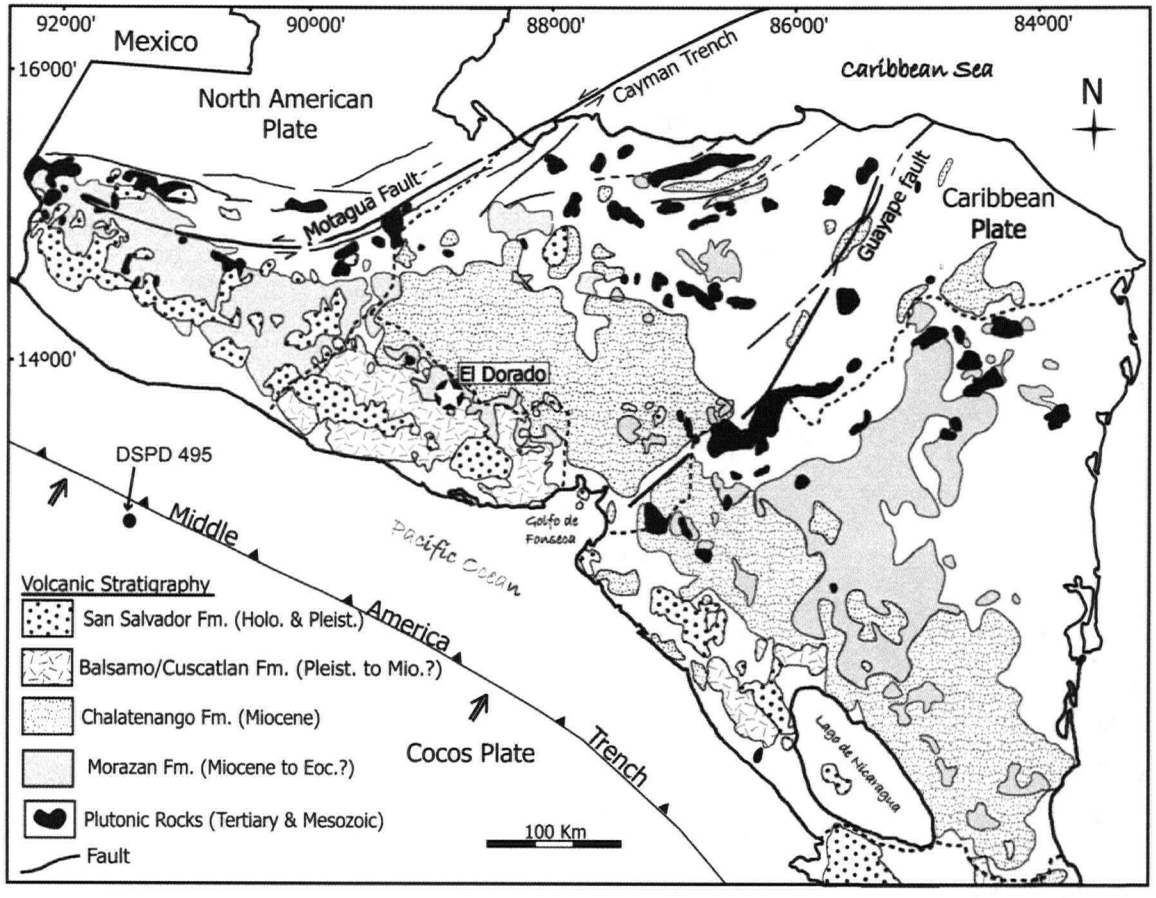

Figure 3.1. Distribution of Cenozoic volcanic and Mesozoic to Cenozoic intrusive rocks in northern Central America (modified from Weyl, 1980). Volcanic rock formations are named after the El Salvador nomenclature (Wisemann, 1975). Tertiary volcanic rocks in Guatemala include deposits of the Morazan and Chalatenango Formations, but are not differentiated on the map of Weyl (1980). They have been grouped as one single unit here under the Morazan Formation for illustration purposes.

A

Volcanic stratigraphy of El Salvador

Age	Formations	Facies descriptions	Av. silica (wt%)
Holocene	San Salvador Fm	Lavas and tephras of the Quaternary volcanoes along the volcanic front and back-arc regions;	52.4-65.7
Pleistocene to Pliocene 4.0±0.2 Ma	Cuscatlan Fm	Felsic pyroclastic and epiclastic rocks at the base grading into felsic to intermediate lava flows and domes;	–
4.1±0.4 Ma Pliocene to Miocene? 6.65±0.3 Ma	Balsamo Fm	Mafic to intermediate lava flows and associated autobreccias intercalated with epiclastic to pyroclastic rocks ;	–
9.4±0.4 Ma Miocene	Chalatenango Fm	Extensive felsic pyroclastic and epiclastic rocks locally interbedded with felsic lava flows;	70.8
15.7±0.6 Ma Miocene to Eocene?	Morazan Fm	Felsic to intermediate intrusive rocks;	–
		Mafic to intermediate lava flows and autobreccias, volcanogenic sedimentary rocks and intermediate to felsic epiclastic and pyroclastic rocks;	57.7

B

Volcanic stratigraphy of the El Dorado district

Age	District Unit Name	Facies descriptions	Silica (wt %)
Pleist.? Pliocene?	Post-mineral lava flows	-Mafic to intermediate lava flows;	51 to 60
3.36±0.49 Ma to 3.93±0.17 Ma	Pliocene felsic rock sequences	-Coeval felsic pyroclastic to tuffaceous sedimentary rocks and rhyolitic to dacitic domes/plugs/dikes and lava flows;	66 to 76
4.06±0.29 Ma to 4.7±0.2 Ma (?)	Epithermal veins and sinters	-Sinter deposits and silica replacement horizons associated with hydrothermal breccias;	
Pliocene	Cerro Caballo dome complex	-Dacite dome complex associated with flow banded, spherulite/lithophysae-rich lava flows;	63 to 69
	Plan de Minas volcaniclastics	-Intermediate to felsic, interbedded epiclastic and pyroclasitc rock sequence;	
4.57±0.74 Ma to 4.63 ± 0.37 Ma	Platy andesites	-Andesite lava flows (post-mineral?);	57 to 60
10.7±1.9 Ma Miocene Oligocene?	Volcanic basement rock sequence	-Porphyritic basalt to andesite domes and dikes; -Basaltic to andesitic lava flows and autobreccias, interbedded with volcanogenic sedimentary rocks ;	50 to 60

Figure 3.2. A) Volcanic stratigraphy of El Salvador after Wiesemann (1975). Age limits are from Catastro (1972) and Reynolds (1977, 1980). Average composition of volcanic rock Formations are from Pichler and Weyl (1973). B) Volcanic stratigraphy of the El Dorado district with timeline constrained by current geochronology results and those of McDowell (written comm., 2006). Compositional range of different rock units in terms of silica content from current study.

The volcanic basement rocks in the district are unconformably overlain and cross-cut by mafic to dominantly felsic Pliocene volcanic rocks. The Cerro Caballo lava dome and flow complex, although not yet constrained by geochronology, may have been emplaced during the late Miocene or early Pliocene prior to epithermal mineralization. The dome rock and associated lava flows host mineralized veins at the surface. Andesite lava flows with a gently dipping fracture pattern referred to as "platy andesites" were dated at 4.63 ± 0.37 Ma and 4.57 ± 0.74 Ma based on ^{40}Ar-^{39}Ar geochronology on plagioclase. Their age is likely younger since they do not host any veins or signs of hydrothermal alteration, and likely post-date mineralization, which is constrained between 4.7 ± 0.2 Ma and 4.06 ± 0.29 Ma based on ^{40}Ar-^{39}Ar geochronology on vein adularia. The waning stages of hydrothermal activity associated with vein formation coincide with the onset of extensive felsic volcanism, which was active between 3.94 ± 0.29 Ma and 3.36 ± 0.49 Ma based on argon geochronology of major felsic volcanic rock units (Figure 3.2b). Felsic volcanic rocks include domes, plugs, lava flows, and volcaniclastic rocks including pyroclastic and sedimentary rocks. Basaltic to andesitic lava flows of Pliocene to Pleistocene age post-date mineralization and cap the volcanic stratigraphy. Petrographic descriptions and major geochemical characteristics of all rock units are summarized in table 3.1. For an extensive description of the volcanic stratigraphy and the related epithermal vein system, the reader is referred to the manuscript forming the first part of this thesis (a formal reference will be included at the time of publication).

The volcanic rocks building the framework of the El Dorado epithermal vein system have thus evolved from dominantly mafic and intermediate to dominantly felsic with a major time unconformity (~5 m.y.) separating the two compositional groups. The two groups represent distinct magmatic events that characterize the shift in subduction and magmatic activity during the Miocene to Pliocene transition.

Table 3.1
Summary of petrographic and geochemical characteristics of major volcanic rock units at El Dorado.

Rock unit name	Symbol	Petrography	Geochemistry (Normalized to 100% anhydrous)
Post-mineral lava flows	Tb	Massive, flow banded to columnar jointed plagioclase-pyroxene-phyric basaltic to andesitic lava flows.	Calc-alkaline: SiO_2 (52-63 wt%), $Na_2O + K_2O$ (4.06-5.53 wt%).
Platy andesite lava flows	Ta	Medium-grained porphyritic, plagioclase-pyroxene-phyric andesitic lava flows.	Calc-alkaline: SiO_2 (59-60 wt%), $Na_2O + K_2O$ (5.39-5.44 wt%).
Pliocene felsic rock sequences	Tr	Quartz-plagioclase-biotite ± hornblende-phyric dacite and rhyolite domes, plugs, dikes, lava flows and tuffs; Accessory zircon and apatite common.	Calc-alkaline to high-K: SiO_2 (68-77 wt%), $Na_2O + K_2O$ (6.16-8.40 wt%).
Cerro Caballo lava flows facies	Tdf	Finely flow-banded to brecciated plagioclase-pyroxene(?)-hornblende-phyric dacite/rhyolite containing abundant lithophysae and spherulites. Widely silicified and hydrothermally altered.	Calc-alkaline: SiO_2 (72.78 wt%), $Na_2O + K_2O$ (6.77 wt%).
Cerro Caballo dome facies	Tdd	Medium- to coarse-grained porphyritic, plagioclase-pyroxene-hornblende-phyric dacite grading to finer-grained flow-banded textures towards the margins of the dome; Contains accessory zircons.	Calc-alkaline: SiO_2 (64-65 wt%), $Na_2O + K_2O$ (6.08-6.36 wt%).
Porphyritic dikes and domes (volcanic basement rocks)	Tap	Medium- to coarse-grained porphyritic plagioclase-pyroxene-phyric basaltic to andesitic dikes and domes.	Calc-alkaline: SiO_2 (52-63 wt%), $Na_2O + K_2O$ (4.56-6.86 wt%).
Lower lava sequence (volcanic basement rocks)	Tma	Fine- to medium-grained, sparsely porphyritic plagioclase-pyroxene-phyric basaltic to andesitic lava flows.	Calc-alkaline: SiO_2 (53-57 wt%), $Na_2O + K_2O$ (4.10-5.11 wt%).

3.3 Data and analytical methods

Thirty-nine rock samples representing all major stratigraphic levels were analyzed by X-ray fluorescence spectroscopy (XRF) and inductively coupled plasma mass spectrometry (ICP-MS) methods for major and trace elements at ALS/Chemex laboratories in North Vancouver, Canada. The samples were crushed and pulverized by chrome steel plates and digested using a lithium metaborate fusion followed by dissolution in trace acid. To assess data quality, five rock samples were split into three to four aliquots and sent under different tag names. Those samples include MM01, MR04-42, MR04-79, MR04-50 and MR04-83, respectively representing a volcanic basement basaltic andesite lava flow, the Cerro Caballo dome and lava flow facies, a rhyolite lava flow and a post-mineral basaltic lava flow. Two aliquots of two MDRU standards, P-1 and BAS-1, a rhyolite and a basalt respectively, were also included. The analytical precision (expressed as a percentage standard deviation) ranges from 0.2% to ~10% for major oxides, ~1% to ~5% for large ion lithophile elements, and below 15% for the remaining trace elements. The full geochemical data set for the thirty-nine rock samples and the seven replicate samples is included in Appendix C.

Although the freshest samples were preferentially selected in the field, many have experienced the effects of hydrothermal alteration and show signs of element mobility. This paper uses a subset of twenty-six fresh samples that show no (or very limited) signs of element mobility due to hydrothermal alteration. The altered samples were identified and taken out of the original data set for the purpose of the geochemical analysis. The details on the selection process can be found in Appendix D.

Twelve samples that best represent all stratigraphic units in the district were analyzed at the Pacific Centre for Isotopic and Geochemical Research (PCIGR), at the University of British Columbia, for selected trace elements (Rb, Sr, Ta, Th, Hf, Nb), and for whole rock strontium, neodymium, and lead isotopic ratios. The whole rock XRF, high precision trace elements and isotope geochemistry of the twelve rock samples are shown in Table 3.2. The Sr ratios were obtained on a Triton Finnigan TIMS using the single Ta method whereas a Nu Instrument MC-ICP-MS was used to determined Nd and Pb ratios. Details on the analytical procedure can be found in Pretorius et al. (2006) and Weis et al. (2005). Table 3.3 shows the isotopic composition of each rock sample, with

duplicate and average values for SRM 987, La Jolla Nd and SRM 981 standards obtained during this study. The measured isotopic compositions were recalculated to the initial ratios considering age uncertainties on the different rock units and appropriate decay constants. The results are summarized in Table 3.4.

The geochemistry of lavas and tephras from Quaternary volcanic centers of Central America were used as a geochemical reference to compare with Tertiary volcanic rocks. The data was taken from an updated version of the CENTAM database of Carr and Rose (1987) available online (*http://www.rci.rutgers.edu/~carr/index.html*). The database includes whole rock geochemical analyses of 1528 volcanic rock samples including major and trace elements, and Sr, Nd, and limited Pb isotopic ratios.

In order to fully understand the geochemical variations observed in volcanic rocks erupted along the Central American plate margin, it is important to consider seafloor sediments being subducted along the Middle America trench. The sediment column identified by DSDP hole 495 off the coast of Guatemala (Figure 3.1) is composed of a 250-m-thick basal section of carbonate sediments overlain by a 175-m-thick sequence of hemipelagic sediments with contrasting geochemistry (Patino et al., 2000). Selected trace element ratios of Central American arc lavas indicate the possible input from those sediments during magma genesis (e.g., Patino et al., 2000, Cameron et al., 2002). The mean composition of the two sediment types reported by Patino et al. (2000) will be used here to infer source components for the volcanic rocks at El Dorado.

Table 3.2
Geochemical analyses for a suite of twelve rock samples representing all stratigraphic levels at El Dorado.

Elements/ samples	MM01	MR04-53	MR04-06	MR04-61	MR04-79	MR04-42	MR04-50	MR04-24	MR04-16	MR04-58	MR04-83	MR04-101	Mean std dev
SiO2 (wt%)	51.91	55.30	55.80	50.25	70.02	64.17	71.58	66.07	72.37	75.90	51.15	60.01	0.47
Al2O3	18.30	18.01	18.37	20.50	14.41	17.00	13.92	16.64	12.36	13.10	19.69	15.95	0.24
Fe2O3	9.59	7.63	6.92	8.18	2.24	4.94	1.85	3.28	1.53	0.78	9.01	5.51	0.10
CaO	8.40	7.03	5.73	9.01	2.02	4.13	1.87	2.87	0.82	1.05	9.98	5.29	0.11
MgO	4.20	3.22	1.64	2.69	0.41	1.33	0.44	0.51	0.51	0.05	3.35	2.55	0.07
Na2O	3.19	3.48	4.04	3.37	2.90	4.10	3.60	4.06	2.01	3.75	3.02	3.60	0.09
K2O	0.83	1.50	0.95	1.03	3.61	2.18	3.18	2.74	4.58	3.59	0.99	1.69	0.04
TiO2	1.03	0.87	0.84	0.93	0.24	0.50	0.19	0.33	0.20	0.19	0.95	0.58	0.04
MnO	0.16	0.13	0.18	0.16	0.06	0.09	0.07	0.08	0.04	0.01	0.18	0.10	0.01
P2O5	0.17	0.24	0.29	0.19	0.08	0.13	0.05	0.02	0.04	0.03	0.19	0.16	0.02
LOI	1.30	2.23	4.98	3.00	3.47	1.07	2.77	2.54	3.58	1.17	1.09	2.79	0.10
Ba (ppm)	482	594	1145	485	1575	956	1195	1150	1345	1375	550	809	16
Rb**	7.44	26.90	18.20	16.60	123.00	47.00	68.90	64.00	105.00	81.00	22.00	31.00	1.58
Sr**	513.59	450.00	653.00	525.00	394.90	389.00	225.00	286.00	119.00	133.00	552.00	402.00	7.79
Hf**	2.40	3.57	3.30	2.20	2.67	3.62	2.40	3.50	3.10	2.64	1.80	2.90	0.09
Nb**	2.49	3.56	3.11	1.94	4.07	3.82	3.80	4.10	5.10	4.20	2.00	3.30	0.12
Ta**	0.120	0.163	0.143	0.101	0.340	0.297	0.340	0.343	0.488	0.415	0.110	0.180	0.007
Th**	1.17	1.73	1.21	1.33	4.00	3.30	5.93	4.69	7.30	7.50	1.92	2.40	0.09
Tl*	0.5	0.4	0.4	0.4	0.5	0.5	0.5	0.4	0.4	0.4	0.5	0.4	-
U*	0.5	0.7	0.5	0.5	1.5	1.3	2.2	2.0	2.5	3.0	0.7	1.0	0.1
Y	20.1	23.0	27.4	21.2	13.3	16.7	8.7	9.0	10.6	9.0	18.5	21.7	0.6
Zr	84.6	144.0	119.5	90.6	87.1	142.6	79.9	131.0	105.0	80.3	64.8	132.0	5.2
La	8.4	11.8	12.1	8.8	14.2	12.6	13.0	11.4	18.0	19.4	8.6	12.0	0.4
Ce	18.5	25.1	26.6	19.0	22.5	23.5	22.3	22.9	29.6	27.0	18.1	27.6	0.8
Pr	2.7	3.6	4.0	2.8	2.9	3.1	2.5	2.3	3.5	3.8	2.7	3.2	0.2
Nd	13.4	15.8	18.2	13.0	11.4	13.6	9.3	8.0	11.7	12.0	13.4	13.0	0.7
Sm	3.4	3.6	4.7	3.6	2.1	2.9	1.6	1.5	1.9	1.9	3.4	2.9	0.1
Eu*	1.1	1.1	1.3	1.0	0.6	0.8	0.4	0.6	0.4	0.5	1.1	1.0	0.1
Gd	3.6	3.8	4.4	3.6	2.2	2.9	1.6	1.5	1.7	1.7	3.4	3.3	0.1
Tb*	0.6	0.6	0.7	0.6	0.3	0.4	0.2	0.2	0.3	0.3	0.5	0.5	-
Dy	3.6	3.8	4.4	3.7	1.8	2.7	1.3	1.4	1.4	1.3	3.4	3.1	0.1
Ho*	0.7	0.8	0.9	0.7	0.3	0.5	0.3	0.3	0.3	0.3	0.6	0.7	0.1
Er	2.1	2.3	2.6	2.0	1.2	1.8	0.9	0.9	1.0	0.9	2.0	1.9	0.1
Tm*	0.3	0.4	0.4	0.3	0.2	0.2	0.1	0.2	0.2	0.2	0.3	0.3	0.1
Yb	2.1	2.3	2.5	1.8	1.2	1.9	1.1	1.2	1.1	1.1	1.9	2.0	0.1
Lu*	0.3	0.4	0.4	0.3	0.2	0.3	0.2	0.2	0.2	0.2	0.3	0.3	-
Pb	4	6	5	4	8	7	8	9	11	11	5	6	1
87Sr/86Sr	0.703747	0.703772	0.703729	0.703743	0.703722	0.703850	0.703786	0.703758	0.703895	0.703849	0.703717	0.703718	0.000007
143Nd/144Nd	0.512951	0.512941	0.512941	0.512966	0.512963	0.512953	0.512959	0.512953	0.512952	0.512957	0.512966	0.512962	0.000006
206Pb/204Pb	18.6770	18.6612	18.6656	18.6583	18.6500	18.6700	18.6375	18.6701	18.6480	18.6489	18.6153	18.6506	0.0008
207Pb/204Pb	15.5772	15.5787	15.5777	15.5757	15.5744	15.5769	15.5728	15.5777	15.5756	15.5741	15.5689	15.5760	0.0008
208Pb/204Pb	38.3741	38.3720	38.3709	38.3658	38.3597	38.3786	38.3463	38.3723	38.3600	38.3546	38.3148	38.3629	0.0025

Note: all major oxides are given in wt% and all trace elements are given in ppm;
The composition of samples MM01, MR04-79, MR04-42, MR04-83 and MR04-50 represent the mean of replicate analyses.
* elements below or at detection level; analysis by ALS/Chemex
**elements analyzed at the PCIGR; mean standard deviation calculated from uncertainties reported by PCIGR

Table 3.3
Isotopic analyses of El Dorado rock samples and standards reported by PCIGR.

Samples/isotopes	$^{206}Pb/^{204}Pb$	Uncertainty (2σ)	$^{207}Pb/^{204}Pb$	Uncertainty (2σ)	$^{208}Pb/^{204}Pb$	Uncertainty (2σ)	$^{87}Sr/^{86}Sr$	Uncertainty (2σ)	$^{143}Nd/^{144}Nd$	Uncertainty (2σ)
MM01	18.6821	0.0007	15.5789	0.0006	38.3801	0.0017	0.703756	0.000007	0.512949	0.000006
MM01 Duplicate	18.6718	0.0010	15.5755	0.0010	38.3682	0.0032	0.703737	0.000006	0.512952	0.000008
MR04-06	18.6656	0.0009	15.5777	0.0011	38.3709	0.0038	0.703729	0.000007	0.512941	0.000008
MR04-16	18.6480	0.0008	15.5756	0.0009	38.3600	0.0022	0.703895	0.000007	0.512952	0.000007
MR04-24	18.6701	0.0007	15.5777	0.0007	38.3723	0.0020	0.703758	0.000008	0.512953	0.000006
MR04-42	18.6500	0.0007	15.5744	0.0006	38.3597	0.0016	0.703722	0.000008	0.512963	0.000007
MR04-50	18.6375	0.0014	15.5728	0.0017	38.3463	0.0054	0.703786	0.000007	0.512959	0.000005
MR04-53	18.6612	0.0008	15.5787	0.0005	38.3720	0.0018	0.703772	0.000007	0.512941	0.000006
MR04-58	18.6489	0.0009	15.5741	0.0008	38.3546	0.0024	0.703849	0.000008	0.512957	0.000006
MR04-61	18.6583	0.0007	15.5757	0.0006	38.3658	0.0018	0.703743	0.000006	0.512966	0.000006
MR04-79	18.6702	0.0005	15.5765	0.0005	38.3770	0.0016	0.703856	0.000007	0.512951	0.000006
MR04-79 Duplicate	18.6698	0.0007	15.5773	0.0009	38.3803	0.0027	0.703844	0.000007	0.512955	0.000006
MR04-83	18.6153	0.0006	15.5689	0.0006	38.3148	0.0017	0.703717	0.000007	0.512966	0.000006
MR04-101	18.6506	0.0010	15.5760	0.0010	38.3629	0.0032	0.703718	0.000007	0.512962	0.000006
Standard SRM 987	-	-	-	-	-	-	0.710247	0.000011	-	-
Standard La Jolla									0.511849	0.000010
Standard SRM 981	16.9409	0.0018	15.4970	0.0018	36.7147	0.0058	-	-	-	-

2σ uncertainty is the absolute error value of the individual sample analysis (internal error)
The uncertainty on standards is 2 standard devision on the mean of the standard material

Table 3.4
Initial isotopic ratios of selected volcanic rock samples at El Dorado recalculated according to their respective age.

Samples	Age Ma (min-max)	$^{206}Pb/^{204}Pb$ (min)	$^{206}Pb/^{204}Pb$ (max)	$^{207}Pb/^{204}Pb$ (min)	$^{207}Pb/^{204}Pb$ (max)	$^{208}Pb/^{204}Pb$ (min)	$^{208}Pb/^{204}Pb$ (max)	Age Ma (min-max)	$^{87}Sr/^{86}Sr$ (min)	$^{87}Sr/^{86}Sr$ (max)	$^{143}Nd/^{144}Nd$ (min)	$^{143}Nd/^{144}Nd$ (max)
MR04-53	8.8-15.0	18.6511	18.6440	15.5783	15.5779	38.3638	38.3581	8.8-15.0	0.703750	0.703735	0.512933	0.512927
MM01	8.8-15.0	18.6662	18.6586	15.5767	15.5763	38.3658	38.3599	8.8-15.0	0.703741	0.703738	0.512942	0.512935
MR04-06	8.8-12.0	18.6570	18.6533	15.5773	15.5772	38.3640	38.3610	8.8-12.0	0.703719	0.703715	0.512932	0.512928
MR04-61	8.8-12.0	18.6475	18.6429	15.5752	15.5750	38.3563	38.3522	8.8-12.0	0.703732	0.703727	0.512956	0.512952
MR04-42	4.7-8.0	18.6420	18.6365	15.5741	15.5738	38.3527	38.3479	4.7-8.0	0.703699	0.703683	0.512959	0.512956
MR04-79	4.7-8.0	18.6612	18.6551	15.5765	15.5762	38.3708	38.3653	4.7-8.0	0.703790	0.703748	0.512950	0.512947
MR04-24	3.5-3.7	18.6624	18.6620	15.5773	15.5773	38.3664	38.3661	3.5-3.7	0.703725	0.703724	0.512950	0.512950
MR04-16	3.4-4.0	18.6405	18.6391	15.5752	15.5752	38.3528	38.3515	3.4-4.0	0.703771	0.703750	0.512950	0.512949
MR04-50	3.4-4.0	18.6285	18.6269	15.5724	15.5723	38.3382	38.3367	3.4-4.0	0.703743	0.703736	0.512957	0.512956
MR04-58	2.9-3.9	18.6413	18.6386	15.5738	15.5737	38.3483	38.3461	2.9-3.9	0.703777	0.703752	0.512955	0.512955
MR04-101	2.0-3.0	18.6474	18.6457	15.5758	15.5757	38.3603	38.3590	2.0-3.0	0.703712	0.703708	0.512960	0.512959
MR04-83	2.0-3.0	18.6126	18.6112	15.5688	15.5687	38.3123	38.3110	2.0-3.0	0.703714	0.703712	0.512964	0.512963

3.4 El Dorado district lithogeochemistry

3.4.1 Major oxides

The volcanic rocks at El Dorado are calc-alkaline, bordering the high-K series, and range in composition from basaltic andesites to rhyolites (Figure 3.3a & b). Volcanic basement rocks of the lower lava sequence (open triangles) plot within the basaltic andesite field (Figure 3.3b), while the porphyritic domes and dikes (solid triangles), represented by four rock samples, cover the basaltic andesite to dacite fields, with one sample bordering the trachy-andesite/dacite fields (Figure 3.3b). The rocks from the Cerro Caballo dome complex (solid square and + symbol) are dacitic and rhyolitic, representing the intrusive and lava flow facies respectively. This lava flow sample is partly silicified and its apparent rhyolitic composition could therefore be an effect of hydrothermal alteration (see sample MR04-79 in Appendix B). The lava flow facies associated with the Cerro Caballo dome complex are invariably hydrothermally altered, but this sample was included as the "least altered" in order to represent the extrusive facies of the dome (see Appendix D). The Pliocene felsic rock sequences (solid diamonds) are dacitic to mainly rhyolitic and overlap between the calc-alkaline to high-K series (Figure 3.3a and b). The platy andesite lava flows (open squares) form a cluster in the andesite field. Post-mineral lava flows (asterisks) are basaltic to andesitic in composition (Figure 3.3b). The apparent lack of basaltic volcanic rocks on the total alkali vs. silica diagram (Figure 3.3b) is likely the result of normalizing rocks to an anhydrous composition. Many of the volcanic rock samples, especially the volcanic basement rocks, contain up to 5 wt% volatiles (Table 3.2), the result of simple hydration with no signs of element mobility (see Appendix D). When normalizing to an anhydrous composition, this causes a shift of the geochemical analyses to higher SiO_2 and alkali content, hence the apparent lack of basaltic rocks.

Selected major oxides show smooth, negatively correlated trends with SiO_2 as the measure of differentiation (Figure 3.3c-f). All groups of rocks form coherent trends and clusters, with the exception of MgO vs. SiO_2, where the porphyritic domes and dikes of the volcanic basement rock sequence form a distinct trend at lower MgO contents relative to the main trend (Figure 3.3e).

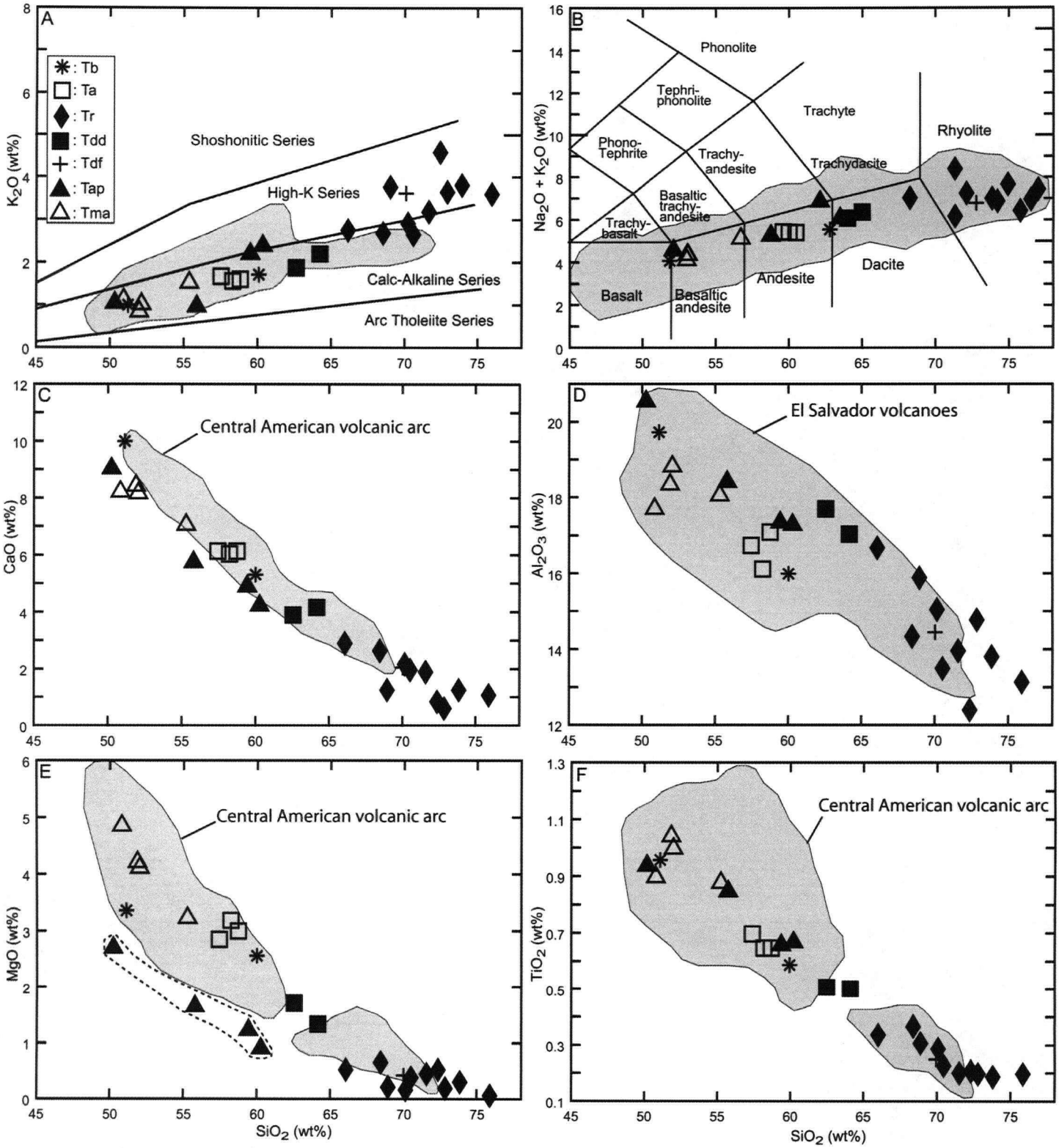

Figure 3.3. Bivariate plots of major oxides for the suites of rocks of the El Dorado district. A) Potassium vs. silica displaying the rock type divisions after Peccerillo and Taylor (1976). B) Alkali vs. silica diagram (TAS) from LeBas et al. (1986) using data normalized to 100% on a volatile-free basis. C) through F) Calcium, aluminum, magnesium and titanium oxides vs. silica respectively. The shaded areas outline the range of geochemical composition of lavas of the Central American volcanic arc. A 1-sigma analytical uncertainty is smaller than the symbols size on all diagrams. Symbols: Tma = lower basement lava sequence; Tap = basement porphyritic dikes and domes; Tdf = Cerro Caballo lava flow facies; Tdd = Cerro Caballo dome facies; Tr = rhyolite domes, flows and tuffs; Ta = post-mineral (?) platy andesites; Tb = post-mineral lava flows.

3.4.2 Trace elements geochemistry

Selected trace element concentrations of the volcanic rocks at El Dorado were plotted against thorium as a measure of differentiation. Most trace elements show smooth positive or negative correlations with increasing Th content, with complete overlap between mafic and intermediate Miocene and Pliocene volcanic rocks. The variations in trace element concentrations partly reflect mantle source composition, degree of melting and/or crystal fractionation processes as will be discussed below.

Barium (Figure 3.4a) shows a steep enrichment trend among mafic rocks, and becomes smooth among felsic rocks. Volcanic basement rocks of the lower lava sequence have Ba values ranging between 473 to 594 ppm. Porphyritic domes and dikes have data ranging from 485 to an anomalously high sample at 1145 ppm. The Cerro Caballo dome and lava flows range from 956 to 1575 ppm. Rhyolites of the Pliocene felsic rock sequences range from 1150 to 1520 ppm. Platy andesites form a cluster between 751 and 859 ppm and post-mineral basaltic and andesitic lava flows have values of 550 and 809 ppm respectively.

Rubidium shows a smooth and progressive enrichment from mafic to felsic rocks (Figure 3.4b). Volcanic basement rocks of the lower lava sequence have Rb values ranging between 7.4 to 26.9 ppm. Porphyritic domes and dikes have a wider range of values from 16.6 ppm to anomalously high samples up to 50.6 ppm. The Cerro Caballo dome facies have values of 25 and 47 ppm to a high of 123 ppm for the lava flow sample. Rhyolites of the Pliocene felsic rock sequences range from 64 to 105 ppm. Platy andesites form a cluster between 27 and 30 ppm and post-mineral basaltic and andesitic lava flows have values of 22 and 31 ppm respectively.

Strontium shows a steady depletion with increasing thorium content (Figure 3.4c). Volcanic basement rocks of the lower lava sequence have Sr values ranging between 450 and 519 ppm. Porphyritic domes and dikes again have a wider range of values from 334 ppm to an anomalously high sample at 653 ppm. The Cerro Caballo dome and lava flow facies have similar values between 386 and 395 ppm. Rhyolites of the Pliocene felsic rock sequences range from 317 to 70 ppm. Platy andesites form a cluster between 438 and 470 ppm and post-mineral basaltic and andesitic lava flows have values of 552 and 402 ppm respectively.

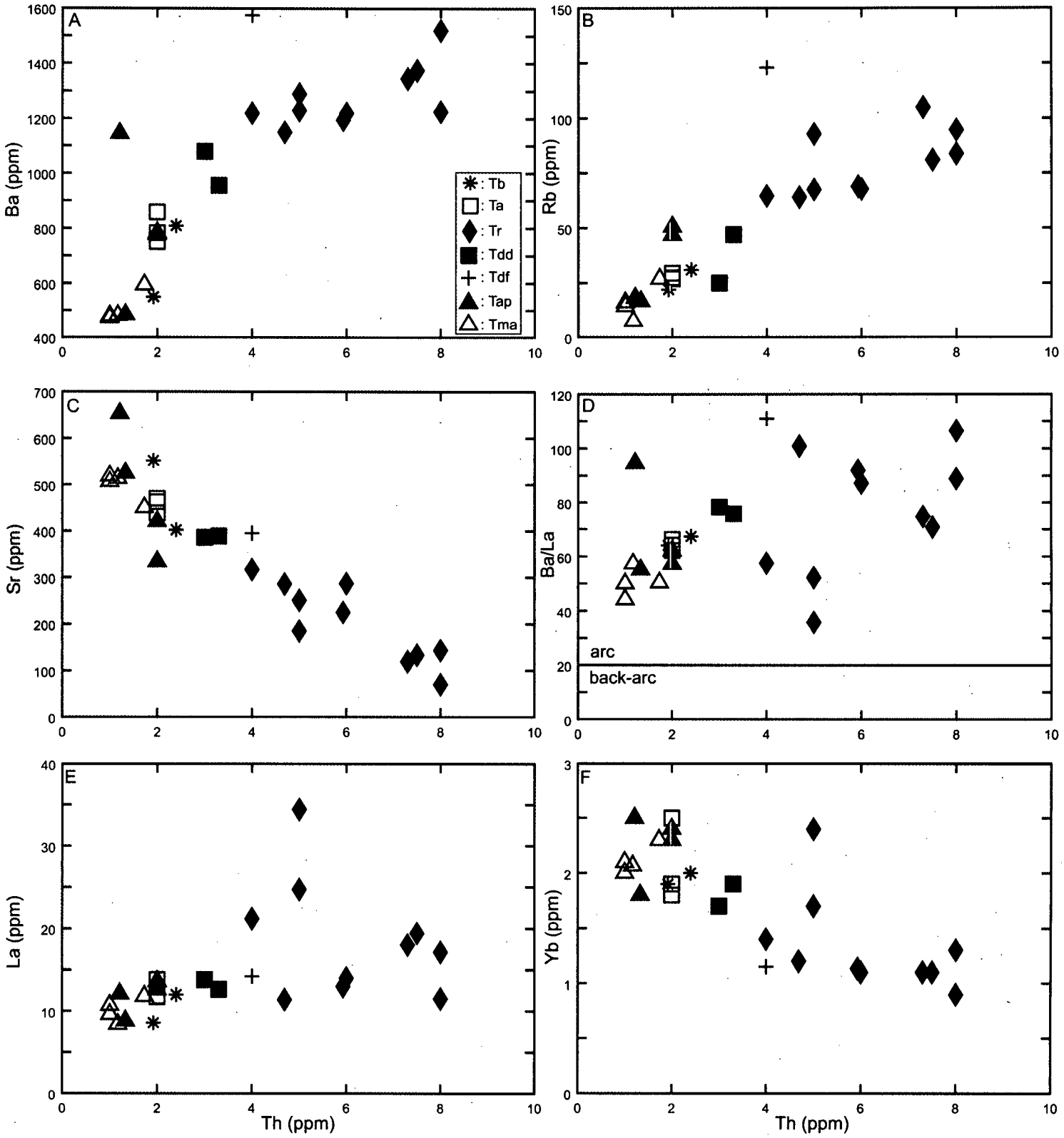

Figure 3.4. Variation diagrams for selected trace elements and element ratios with Th as a measure of differentiation. All trace element concentrations are given in ppm. The arc/back-arc fields limit on the Ba/La vs. Th plot is from Kay et al. (1994). A 1-sigma analytical uncertainty is smaller than the symbols size on all diagrams. See figure 3.3 for symbols explanation.

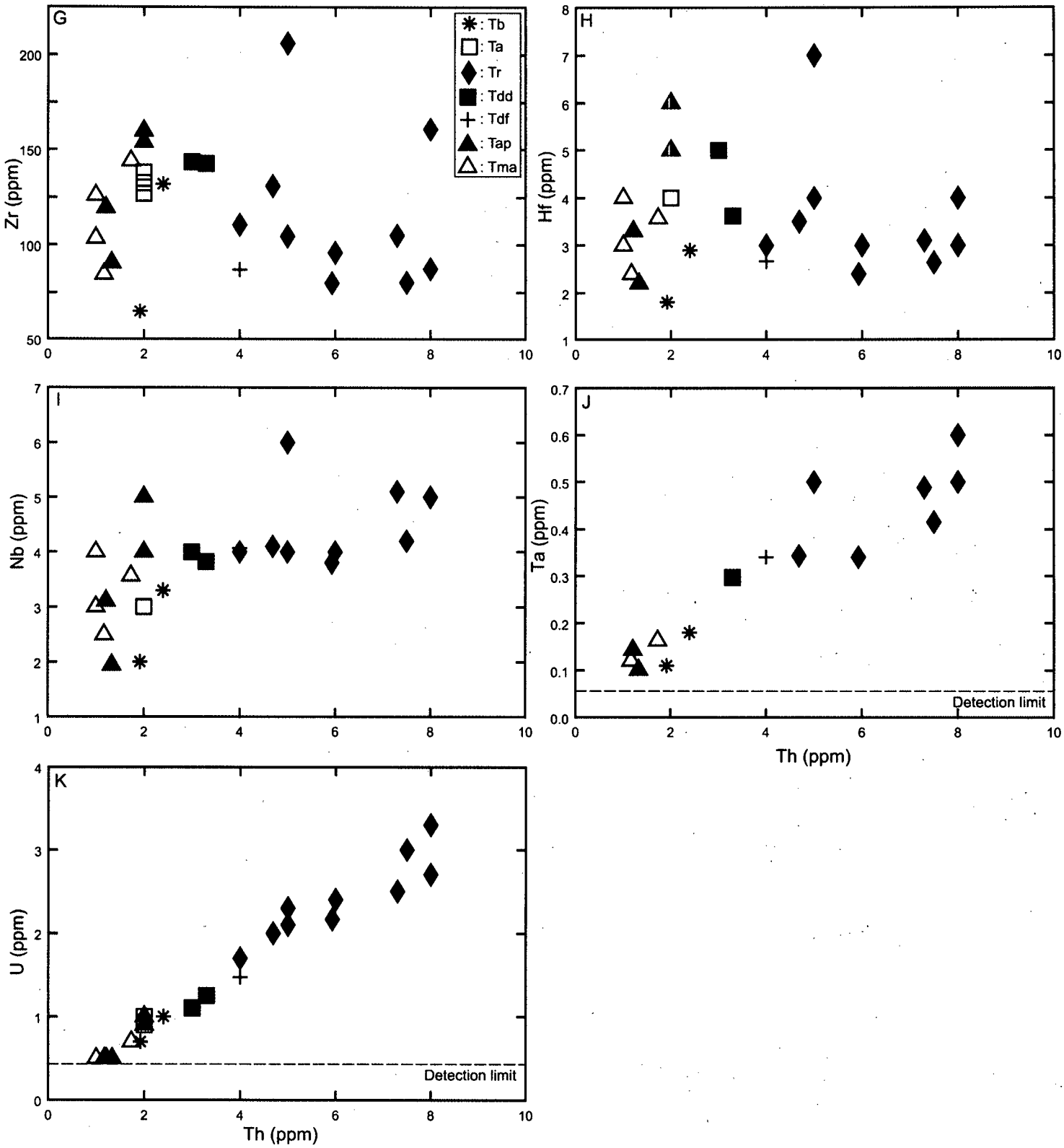

Figure 3.4. Continued.

The Ba/La ratio has been used to differentiate arc vs. back-arc environment for volcanic rocks (Kay et al., 1994). Rocks of the El Dorado district invariably plot in the arc field on a Ba/La vs. Th diagram (Figure 3.3d). With the exception of three rhyolite samples with low Ba/La, it is possible to observe a subtle increase in the Ba/La from mafic to felsic rocks. The low Ba/La of the three felsic rock samples is due to their high La concentrations.

Lanthanum, the lightest of the rare earth elements, shows a smooth and subtle positive correlation with increasing thorium content (Figure 3.4e). Volcanic basement rocks and Pliocene mafic to intermediate volcanic rocks have values ranging from 6.9 to 16.8 ppm. The Cerro Caballo dome and lava flow facies have similar values between 12 and 14 ppm. Most rhyolite samples of the Pliocene felsic rock sequences range from 11.4 to 19.4 ppm, but three samples outliers plot above the main trend reaching up to 34.4 ppm. Those samples plot at distinctively lower Ba/La ratio (Figure 3.4d).

Ytterbium, a heavy rare earth element, shows a smooth negative trend that flattens among felsic samples with increasing Th (Figure 3.4f). The mafic to intermediate rocks have Yb concentrations ranging between 1.4 and 3.4 ppm while the felsic rocks range between 0.9 and 2.4 ppm. Volcanic basement rocks of the lower lava sequence have Yb values ranging between 2.0 and 2.3 ppm. Porphyritic domes and dikes have values between 1.8 and 2.5 ppm. The Cerro Caballo dome facies have similar values of 1.7 and 1.9 ppm, while the lava flow sample has a value of 1.2 ppm. Rhyolites of the Pliocene felsic rock sequences range from 1.7 to 0.9 ppm, with one anomalous sample at 2.4 ppm. Platy andesites have values between 1.8 and 2.5 ppm and post-mineral basaltic and andesitic lava flows have values of 1.9 and 2.0 ppm respectively.

Two similar trends are defined by the high field strength elements Zr and Hf (Figure 3.4g and h). Mafic to intermediate volcanic rocks show a steep positive correlation with increasing thorium content at which point the trend become negative among felsic volcanic rocks (Figure 3.4g). Volcanic basement rocks of the lower lava sequence have Zr values ranging between 84 and 144 ppm. Porphyritic domes and dikes have values between 90 and 160 ppm. The Cerro Caballo dome facies have similar values of 142 and 143 ppm, while the lava flow sample has a value of 87 ppm. Rhyolites of the Pliocene felsic rock sequences range from 110 to 80 ppm, with two anomalous sample at

161 and 206 ppm. Platy andesites cluster between 127 and 138 ppm and post-mineral basaltic and andesitic lava flows have values of 65 and 132 ppm respectively.

The highly incompatibly elements niobium and tantalum display positive correlations with increasing thorium content (Figure 3.4i and j). Niobium shows a steep enrichment among mafic to intermediate volcanic rocks and a relatively flat pattern among felsic rocks. Tantalum on the other hand shows a smooth enrichment from mafic to felsic rocks. In the case of tantalum, many mafic to intermediate rocks have values below the 0.5 ppm detection limit, in which case they do not appear on the diagram.

Uranium displays a perfect positive correlation with increasing Th. Mafic to intermediate rocks have very low uranium concentrations approaching the detection limit of 0.5 ppm, in which case the samples do not appear on the diagram. Volcanic basement rocks of the lower lava sequence have U values ranging from <0.5 to 0.7 ppm. Porphyritic domes and dikes have values between 0.5 and 1.0 ppm. The Cerro Caballo dome and lava flow facies have values between 1.1 and 1.5 ppm. Rhyolites of the Pliocene felsic rock sequences range from 1.7 to 3.3 ppm. Platy andesites cluster between 0.9 and 1.0 ppm and post-mineral basaltic and andesitic lava flows have values of 0.7 and 1.0 ppm respectively.

3.4.3 Rare earth elements

The mafic to intermediate volcanic basement rocks (Figure 3.5a & b) show smooth chondrite-normalized rare earth elements patterns, with relatively flat mid- to heavy-REE tails. The lower lava sequence shows very tight patterns, with minor spread of values in light and heavy-REE (Figure 3.5a). The porphyritic domes and dikes show a slight enrichment in light-REE (30x to 50x chondrite) relative to the lower lava sequence (see grey shaded area for reference), a slightly negative europium anomaly, and relatively flat mid- to heavy-REE patterns (Figure 3.5b).

Rocks of the Cerro Caballo dome and lava flow complex show a more pronounced enrichment in light-REE (50x to 60x chondrite) relative to heavy-REE and a slightly depleted mid-REE to heavy-REE pattern relative to the lower lava sequence (Figure 3.5c). The lava flow sample (+ symbol) shows a greater depletion in mid- and heavy-REE relative to the intrusive facies of the dome (solid square).

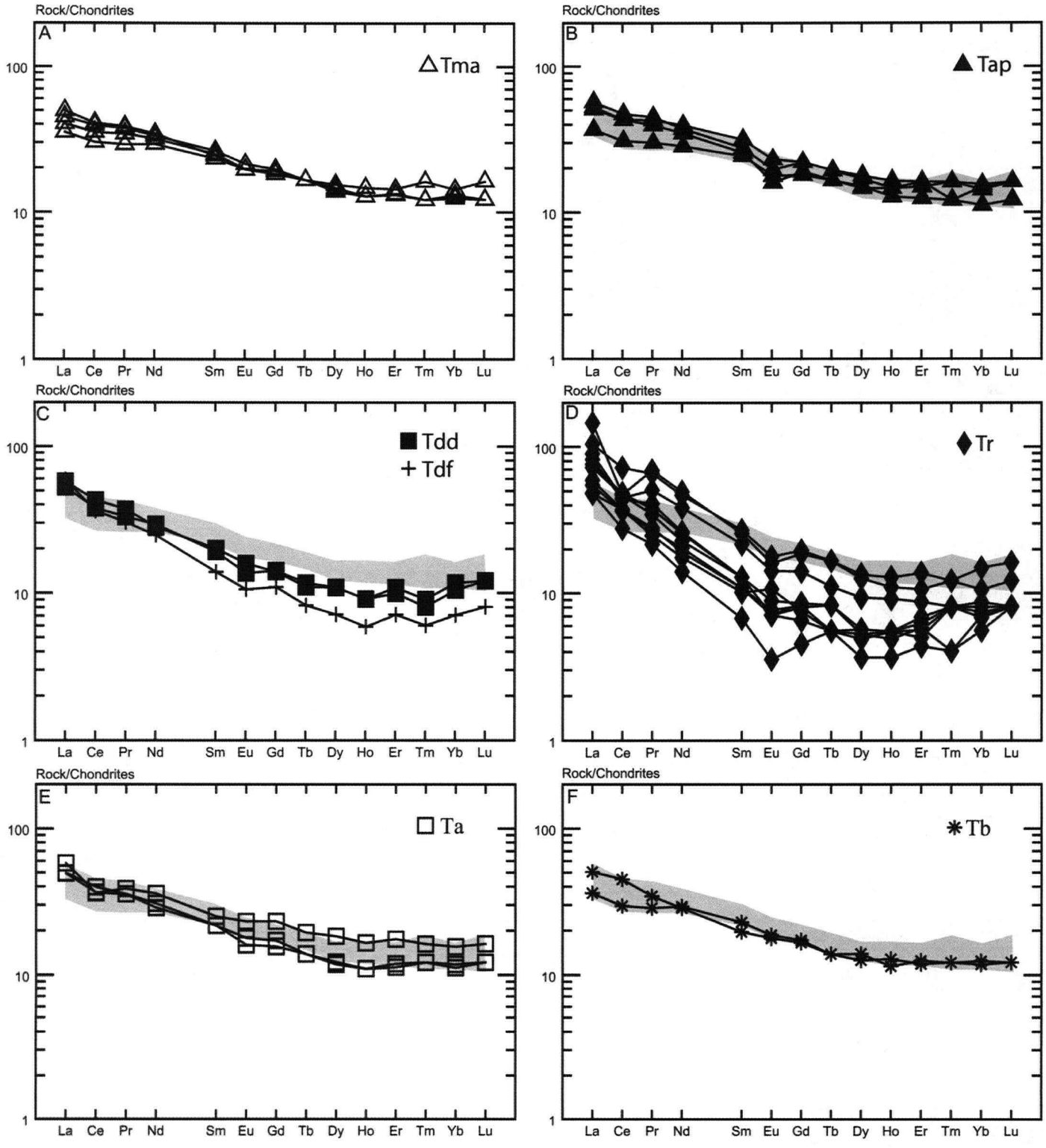

Figure 3.5. Rare earth element patterns normalized to chondritic values from McDonough and Sun (1995). A) Lower lava sequence; B) Porphyritic domes and dikes; C) Cerro Caballo dome and lava flow complex; D) Pliocene felsic rock sequences: rhyolite domes, dikes, lava flows, and tuffs. E) Platy andesite lava flows; F) Post-mineral basaltic and andesitic lava flows. The grey shaded area outlines on diagram b) to f) the pattern produced by the lower lava sequence (Tma) on diagram A). Rocks of the Cerro Caballo dome and flow complex show a slight LREE enrichment and MREE depletion relative to Tma samples. Rhyolitic units on diagram D) show a marked enrichment in LREE and a depletion in MREE. Post-mineral andesitic and basaltic lava flows shown on diagram E) and F) show identical patterns to the mafic to intermediate lava flows forming the basement rocks.

All rhyolites of the Pliocene felsic rock sequences show a pronounced enrichment in light-REE (50x to 150x chondrite) relative to mid- and heavy-REE, and most rocks show a marked depletion in mid-REE to heavy-REE relative to the lower lava sequence (Figure 3.5d). Most rocks also show a slightly negative europium anomaly.

The platy andesite lava flows and the post-mineral basaltic to andesitic lava flows show patterns that overlap with those defined by the lower lava sequence (Figure 3.5e and f). Both rock units show smooth and relatively flat mid- to heavy-REE patterns.

3.4.4 Isotope geochemistry

The neodymium and strontium isotopic ratios of the volcanic rocks at El Dorado were compared those of the Central American arc lavas (Figure 3.6a). Two main trends are defined by the Quaternary mafic lavas of Central America (Carr et al., 1990). On one hand, volcanic rocks from Guatemala and Honduras define a mixing array between a low $^{87}Sr/^{86}Sr$ source, isotopically equivalent to a depleted to enriched MORB, and a high $^{87}Sr/^{86}Sr$ source, isotopically equivalent to crustal samples from Guatemala (Cameron, 1998). In contrast, the Sr and Nd isotopic composition of volcanic rocks from Nicaragua, El Salvador and Costa Rica define an unusual positive correlation between a low $^{87}Sr/^{86}Sr$ source, isotopically equivalent to a depleted to enriched MORB, and a modified mantle source inferred by Carr et al. (1990) to account for the elevated $^{87}Sr/^{86}Sr$ and $^{143}Nd/^{144}Nd$. The modified mantle results from metasomatism of the sub-arc mantle, isotopically equivalent to a depleted to enriched MORB, by a flux of slab and sediment-derived fluids isotopically equivalent to the mean seafloor sediments (Figure 3.6a). Mean seafloor sediments plot at significantly elevated $^{87}Sr/^{86}Sr$ values with means of 0.70763 and 0.70858 for hemipelagic and carbonate sediments respectively. In addition, hemipelagic sediments have a higher $^{143}Nd/^{144}Nd$ isotopic ratio relative to mean carbonate sediments and crustal samples from Guatemala.

The Sr and Nd isotopic composition of volcanic rocks at El Dorado are extremely limited, forming a tight cluster of data at the junction between the two Central American trends explained above (Figure 3.6a). The measured and initial Sr and Nd isotopic ratios of volcanic rocks at El Dorado show no apparent correlation (Figure 3.6b and c). The possible range in initial isotopic composition for each sample, considering age uncertainties, is represented by the bars across the symbols (Figure 3.6c). Three volcanic

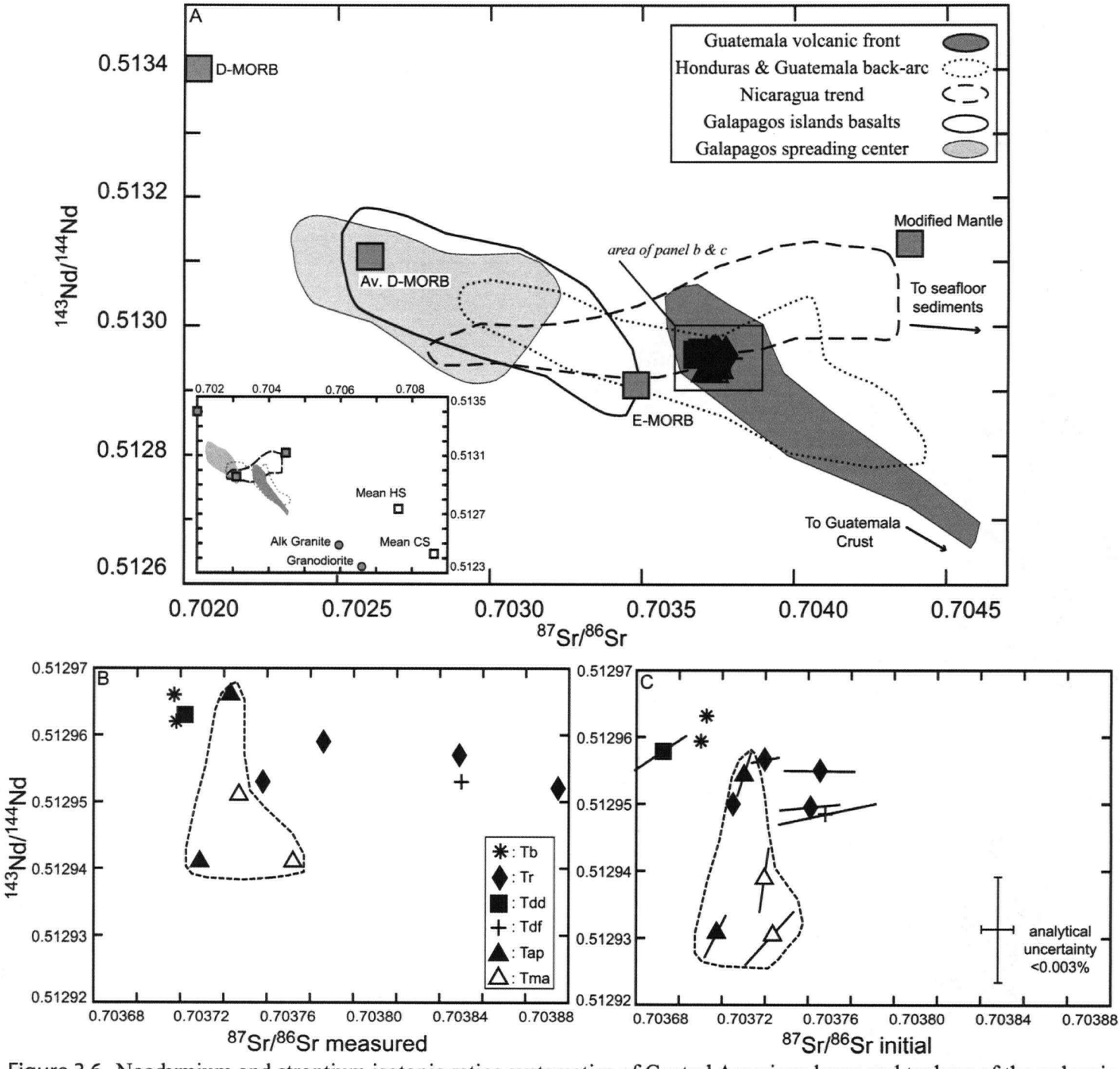

Figure 3.6. Neodymium and strontium isotopic ratios systematics of Central American lavas and tephras of the volcanic front and back-arc regions compared to the El Dorado volcanic rocks. A) D-MORB (Salters and Stracke, 2004), E-MORB (Sun and McDonough, 1989), basalts of the Galapagos hot spot and spreading center (Schilling et al., 2003), and volcanic front (VF) and back-arc lavas (BVF) from Guatemala and Honduras plot along the mantle array. Crustal samples from Guatemala (Cameron, 1998), plot along the extension of this trend, outside the limit of the diagram (see small panel). Quaternary arc lavas from El Salvador, Nicaragua and Costa Rica form a positive correlation defined as the Nicaragua trend on the diagram (dashed contour). This trend extends to an inferred modified mantle source (see text; Carr et al., 1990). Mean subducted sediments (CS: carbonate, HS: hemipelagic) plot outside the limit of the diagram (see small panel). The Tertiary volcanic rocks of El Dorado form a tight cluster at slightly elevated $^{87}Sr/^{86}Sr$ relative to E-MORB. B) and C) Closer view on measured and initial Nd and Sr isotopic ratios for the El Dorado volcanic rocks outlining the volcanic basement rocks. The bars across the symbols represent the possible range of values based on the age uncertainties. Analytical uncertainty is below 0.003%. See figure 3.3 for symbols explanations.

basement rock samples have slightly lower values of $^{143}Nd/^{144}Nd$ (0.512929-0.512942) relative to the main group of samples (0.512948-0.512965), although they partly overlap considering analytical uncertainties. It seems reasonable to conclude that the source region for the El Dorado volcanic rocks is isotopically homogeneous: magmas show no significant variations in $^{87}Sr/^{86}Sr$ and $^{143}Nd/^{144}Nd$, independently of their age and composition.

The volcanic rocks at El Dorado have very limited Pb isotopic composition as shown on uranogenic and thorogenic diagrams (Figure 3.7a and c), overlapping with the fields of sediments and Central American arc lavas. A detailed view on the initial Pb isotopic composition of volcanic rocks at El Dorado is shown on Figure 3.7b and d. The possible range of isotopic composition for each sample is given by the bar across the symbol, and where no bar is present, the range in possible values is included by the symbol size. A maximum analytical uncertainty of 0.015% is associated with each measurements, and includes the external reproducibility. On both thorogenic and uranogenic diagrams, volcanic basement rocks plot at the high $^{206}Pb/^{204}Pb$ end of the spectrum (Figure 3.7b and d). The low $^{206}Pb/^{204}Pb$ end of the spectrum on both diagrams corresponds to a post-mineral basaltic lava flow (Figure 3.7b and d). Rhyolites of the Pliocene felsic rock sequences and rocks from the Cerro Caballo dome and lava flow have isotopic ratios that vary from intermediate $^{206}Pb/^{204}Pb$ values extending to the high end of the spectrum. The implication of this apparent mixing trend, of short extent, between low $^{206}Pb/^{204}Pb$ and high $^{206}Pb/^{204}Pb$ sources will be discussed below. Overall, the Pb isotopic composition (likewise Sr and Nd) of volcanic rocks at El Dorado are extremely limited, independent of rock age or composition.

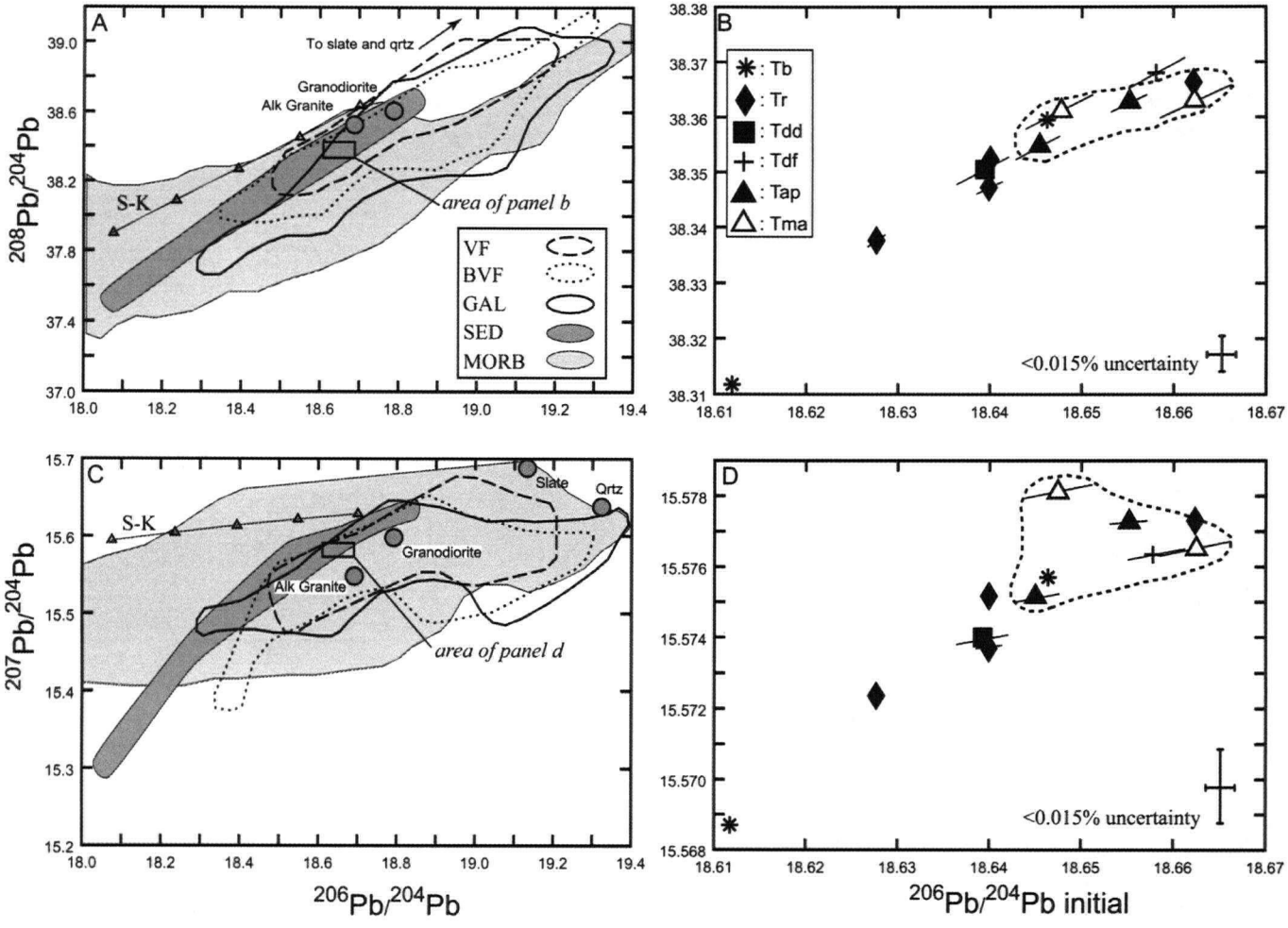

Figure 3.7. A) and C) Thorogenic and uranogenic diagrams showing the range of Pb isotopic composition covered by the Central American volcanoes (VF=Volcanic front; BVF=Back-arc), the carbonate and hemipelagic seafloor sediments off the coast of Guatemala (SED), the Galapagos islands basalts (GAL; Schilling et al., 2003), Pacific MORB (Hoffmann, 2003), Guatemalan crustal samples (Cameron, 1998), and a selected suite of El Dorado volcanic rocks. The average crustal Pb-growth curve of Stacey and Kramers (1975) is shown back to 400 Ma (S-K). Dashed fields on B) and D) outline the compositional range of volcanic basement rocks. See figure 3.3 for symbols explanations.

3.5 Source chemistry and components

3.5.1 Mantle source

The Sm/La ratio, a measure of source depletion in light rare earth element, was plotted against La/Yb, a measure of degree of melting in primitive magmas (Figure 3.8). The Central American sub-arc mantle is compositionally constrained between an enriched and a depleted MORB source (Carr et al., 1990; Plank, 2005), with Sm/La ratios between Pacific E-MORB (~0.4) and N-MORB values (~1.0) for primitive lavas. The mafic to intermediate volcanic rocks at El Dorado have Sm/La values approaching average pacific E-MORB (0.2-0.4) (Figure 3.8), providing a trace element constraint on the composition of the Tertiary sub-arc mantle. Felsic volcanic rocks at El Dorado extend to high La/Yb, with values similar to the continental crust, reflecting the relative enrichment in light-REE, likely due to magmatic differentiation (see below).

The composition of the Central American sub-arc mantle is further constrained by the Sr and Nd isotopic ratios of Quaternary mafic lavas, which compositionally lie between average values of depleted and enriched MORB (Figure 3.6a). The elevated Sr and Nd isotopic composition of lavas from Nicaragua, El Salvador and Costa Rica further suggest the presence of an isotopically modified mantle resulting from the flux of slab and sediment-derived fluids in the mantle wedge (Carr et al. 1990; see above). The Sr and Nd isotopic ratios of the El Dorado volcanic rocks define a tight cluster between the composition of enriched MORB and the inferred modified mantle (Figure 3.6a).

The similarities in trace elements and isotopic composition of Tertiary and Quaternary volcanic rocks suggest that the sub-arc mantle sources have remained analogous. The sub-arc mantle compositionally lies between a depleted and enriched MORB, and is locally modified by the flux of slab and sediment-derived fluids with elevated Sr and Nd isotopic composition (Carr et al. 1990). The very limited isotopic composition of the El Dorado volcanic rocks, independent of rock type or age, suggests a constant and homogenous mantle source associated with the El Salvador volcanic arc during the late Tertiary. This important observation will be expanded below.

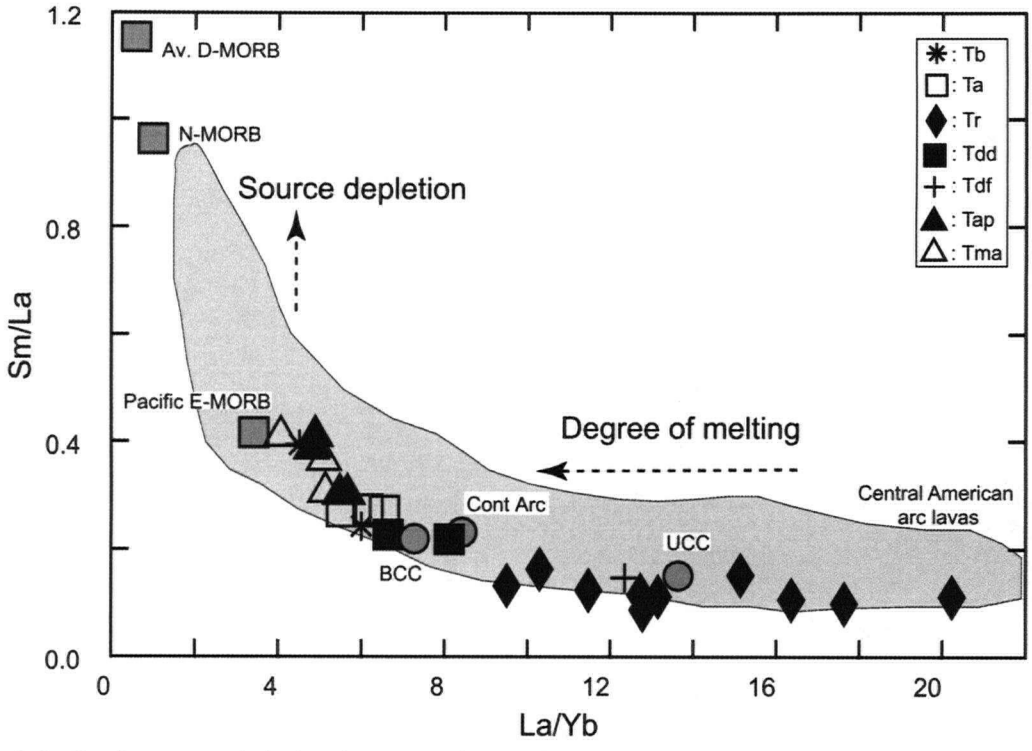

Figure 3.8. Sm/La vs. La/Yb for the Central American lavas and the volcanic rocks at El Dorado. The Sm/La ratio is a measure of source depletion (e.g. Plank, 2005), and the La/Yb ratio a measure of the degree of melting in mafic rocks (e.g. Cameron et al., 2002). The grey shaded area represents the field of Central American arc lavas. Pacific E-MORB from GERM supplemental data, D- and N-MORB from Salters and Stracke (2004) and Hart et al. (1999). Average values for the continental crust by Taylor and McLennan (1995) and Rudnick and Fountain (1995). UCC: upper continental crust; BCC: bulk continental crust. A 1-sigma analytical uncertainty is smaller than the symbols size. See figure 3.3 for symbols explanation.

3.5.2 Input of sediments and slab-derived fluids

The variable input of subducted hemipelagic and carbonate sediments along the Middle America Trench has been demonstrated by Patino et al. (2000) on the basis of Ba/Th and U/La systematics of Central American arc lavas. The two sediment types have distinct geochemistry: hemipelagic sediments have high U/La and relatively low Ba/Th, while carbonate sediments have high Ba/Th and low U/La (Figure 3.9). MORB and continental crust (including Guatemalan crustal samples) define an array of data at relatively constant and low Ba/Th (Figure 3.9). Lavas of the Galapagos spreading center extend along the MORB/crust trend.

Lavas and tephras from individual volcanic centers of Central America define linear arrays sub-parallel to the two sediments end-members, at different distances from the MORB/crust trend. This trend is well illustrated by the Holocene lavas of Telica volcano in western Nicaragua (light-grey diamonds on figure 3.9). Telica volcano has the highest Ba/Th at given values of U/La among Central American volcanoes, and its lavas form a roughly linear trend from low to high U/La. A relationship with the relative age of the lavas was identified by Patino et al. (2000), the oldest rocks having the lowest U/La while younger lavas have progressively higher U/La and lower Ba/Th ratios (older to younger arrow on figure 3.9). This mixing trend has been interpreted to reflect the variable input of hemipelagic versus carbonate sediments in mantle derived magmas at any given time, possibly linked to the physical introduction of sediments during subduction (Patino et al., 2000). In the case of Telica volcano, lavas show a progressively greater input of hemipelagic sediments with time. The high sediment input in the lavas at Telica volcano is further supported by some of the highest $^{10}Be/^{9}Be$ isotopic ratios among Central American volcanoes (Reagan et al., 1994).

The volcanic rocks at El Dorado show a similar linear array, with volcanic basement rocks plotting at low U/La and relatively high Ba/Th, post-mineral basaltic and andesitic lava flows and Cerro Caballo dome and lava flow samples at intermediate U/La, and rhyolites of the Pliocene felsic rock sequences at progressively higher U/La and lower Ba/Th ratios (Figure 3.9). Following the reasoning of Patino et al. (2000), the input of carbonate sediments would appear more important among volcanic basement rocks, while hemipelagic sediment arguably represents a more dominant component of post-

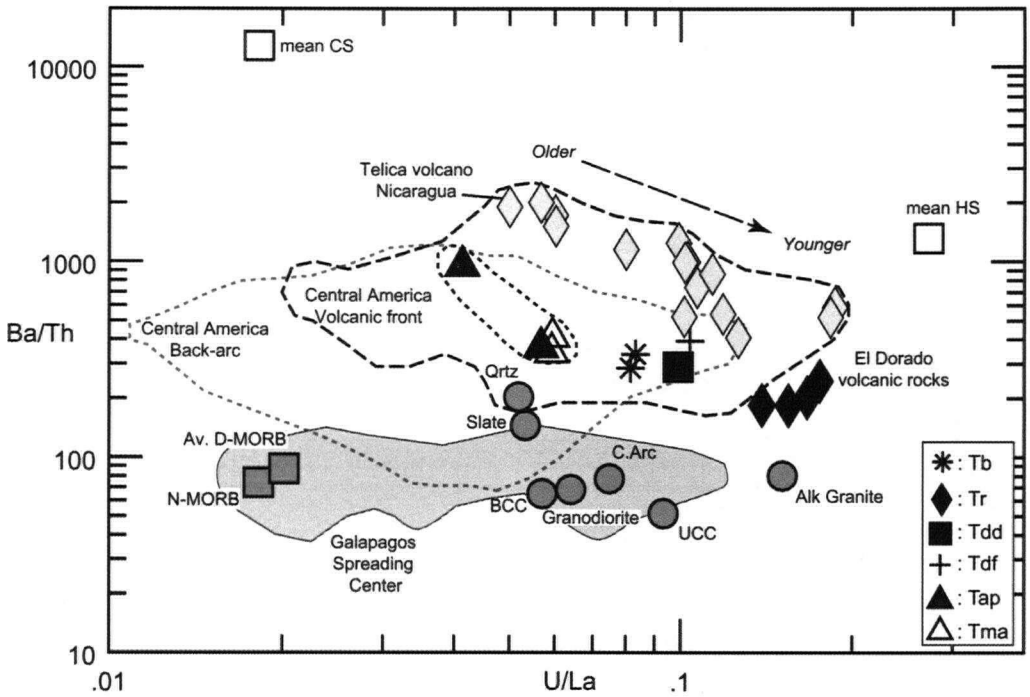

Figure 3.9. Trace element ratios used to infer mixing between different sources during magma genesis along the Central American volcanic arc. Mean compositions of carbonate (CS) and hemipelagic sediments (HS) have contrasting geochemistry (Patino et al., 2000). The grey shaded areas represent the range of composition for basalts of the Galapagos spreading ridge (Schilling et al., 2003). Values of the continental crust/arc from Taylor and McLennan (1995), Rudnick and Fountain (1995), and Cameron (1998). MORB values from Salters and Stracke (2004) and Hart et al. (1999). Lavas from different volcanoes form arrays of data sub-parallel to the mixing line between CS and HS, as displayed by the light grey diamonds representing a suite of rocks from Telica volcano, western Nicaragua. Older lavas at Telica volcano have lower U/La ratios and younger lavas have progressively higher U/La and lower Ba/Th ratios as indicated by the arrow. El Dorado volcanic rocks form a linear array with mafic rocks plotting to the left side of the trend and felsic rocks to progressively higher U/La. UCC: upper continental crust; BCC: bulk continental crust. A 1-sigma analytical uncertainty is smaller than the symbols size on all diagrams. See figure 3.3 for symbols explanations.

mineral basaltic and andesitic lava flows. Subducted sediments may represent a component of felsic volcanic rocks, however, the trend to lower Ba/Th and higher U/La likely represents magmatic differentiation (see Figure 3.4).

The isotope geochemistry of the El Dorado volcanic rocks and Central American arc lavas provides further constraints on the possible input from subducted sediments. In $^{206}Pb/^{204}Pb$ vs. $^{87}Sr/^{86}Sr$ and $^{143}Nd/^{144}Nd$ space, Central American arc lavas appear to define a mixing trend between mantle and crustal sources with hemipelagic sediment having similar isotopic composition to a granite and a granodiorite from Guatemala (Figure 3.10a and b). Similar trends are produced when comparing $^{207}Pb/^{204}Pb$ or $^{208}Pb/^{204}Pb$ to $^{87}Sr/^{86}Sr$ and $^{143}Nd/^{144}Nd$ and therefore are not included. The volcanic rocks at El Dorado overlap with the fields of Central American arc lavas, defining tight clusters with no clear trends among the suite of samples (Figure 3.10c to f). Interestingly, carbonate sediments do not appear to represent a component affecting the isotopic composition of Central American arc lavas and volcanic rocks at El Dorado. This observation appears in disagreement with trace elements signatures of Central American arc lavas that suggest the input of both types of subducted sediments (Figure 3.9). Hawkesworth et al. (1997) showed how trace elements mobilized by a slab-derived fluid flux can modify the geochemistry of arc lavas while retaining their mantle-like Sr isotopic signature. In Central America, slab or sediment-derived fluids could potentially affect the fluid mobile to fluid immobile trace element ratios of arc lavas (e.g., Ba/Th), without modifying their isotopic composition. Under specific segments of the Central American volcanic arc (e.g., western Nicaragua), the input of hemipelagic sediments (as partial melts) may potentially explain the elevated isotopic composition of arc lavas (Figure 3.6a; Figure 3.10a and b). Crustal contamination in come cases could also modify the isotopic composition of arc lavas (Figure 3.10a and b). At El Dorado, the input of subducted hemipelagic sediments and/or crustal contaminant, if any, uniformly modified (or buffered) the isotopic composition of arc magmas during the Miocene and the Pliocene.

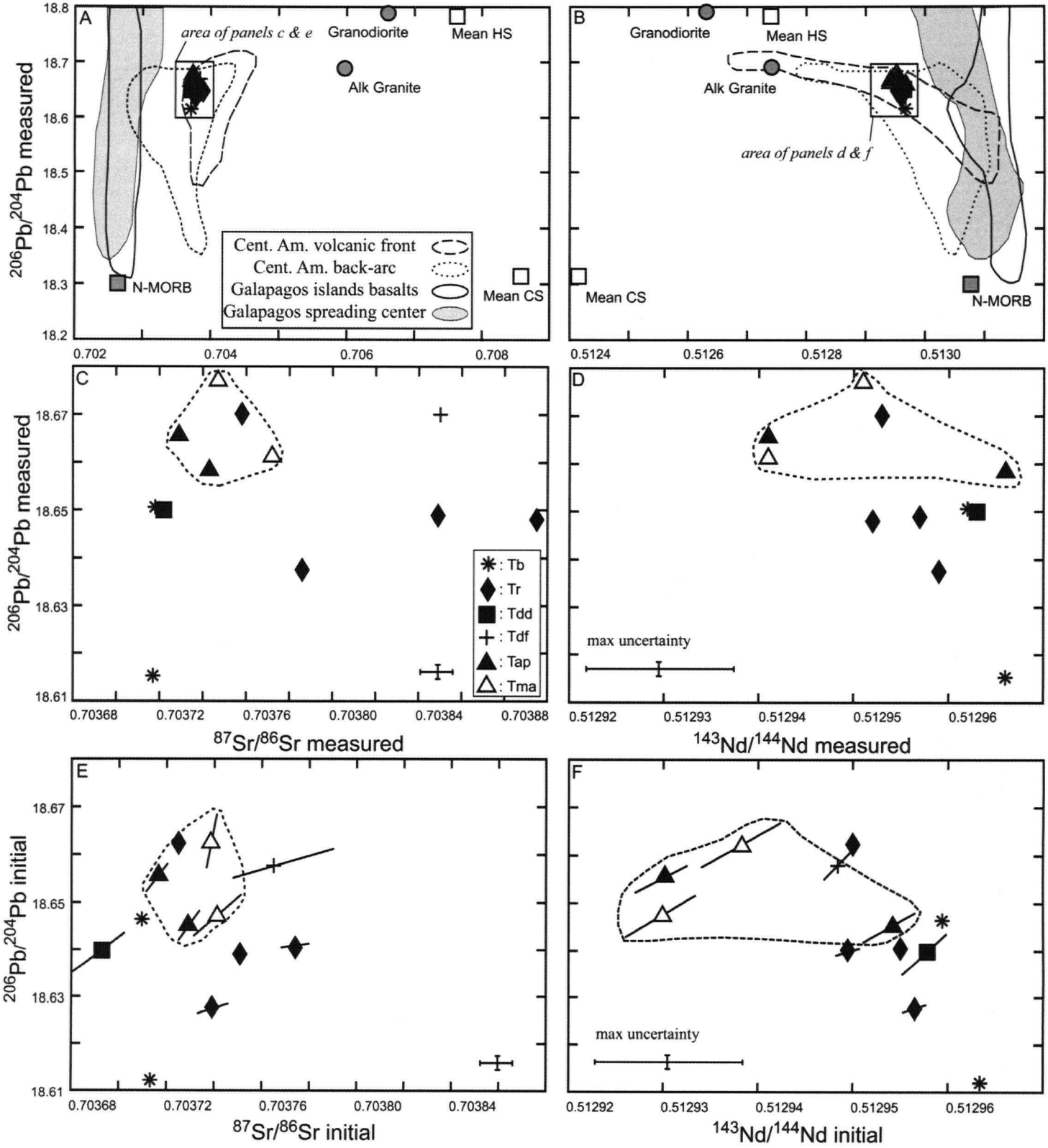

Figure 3.10. A) and B) Measured $^{206}Pb/^{204}Pb$ versus Sr and Nd isotopic composition of Central American arc lavas, the Galapagos islands basalts and spreading center (Schilling et al., 2003), the mean composition of carbonate (CS) and hemipelagic (HS) seafloor sediments off the coast of Guatemala, N-MORB (Hart et al., 1999), Guatemalan crustal samples (Cameron, 1998), and a selected suite of El Dorado volcanic rocks. C) and D) Detailed view on measured $^{206}Pb/^{204}Pb$ versus Sr and Nd isotopic composition of the El Dorado volcanic rocks. E) and F) Detailed view on initial $^{206}Pb/^{204}Pb$ versus Sr and Nd isotopic composition of the El Dorado volcanic rocks. See figure 3.3 for symbols explanations.

3.5.3 Crustal contamination

Physical evidence of crustal assimilation was found in the Cerro Caballo dome rock, where zircons have inherited cores (R. Friedmann, written comm., 2006). Despite trace element signatures that could potentially indicate crustal contributions to Pliocene felsic volcanic rocks (Figure 3.8 and 3.9), the Sr isotopic composition of volcanic rocks at El Dorado is remarkably constant independent of their age or composition (Figure 3.11). Such small variation in isotopic ratios despite a wide range in SiO_2 is also the case of Ordivician volcanic rocks from the Andean margin (Kleine et al., 2004). The authors ruled out any significant assimilation at shallow crustal levels as this would raise the Sr isotopic composition of volcanic rocks (indicated by the AFC arrow on Figure 3.11). Kleine et al. (2004) concluded that the suite of rocks acquired their homogeneous isotopic signatures in the mantle or deep in the crust. The same scenario may have occurred at the Central American margin. The Sr isotopic ratios of volcanic rocks at El Dorado are slightly elevated relative to an enriched mantle source (Carr et al.,1990), but remain remarkably constant well below Guatemalan crustal values (Figure 3.11) ruling out the possibility of assimilation of such material. If crustal rock were indeed assimilated by Tertiary magmas, as revealed by the presence of inherited zircons, the crustal contaminant must have shared an identical isotopic composition to that of volcanic rocks at El Dorado.

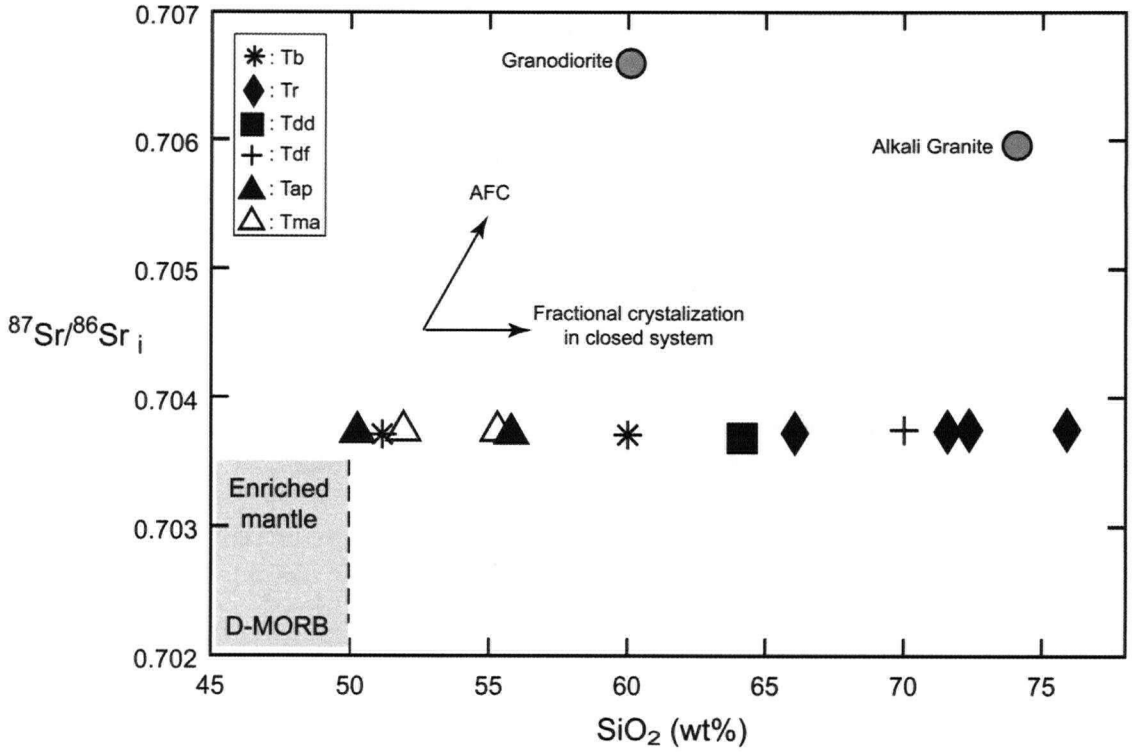

Figure 3.11. Initial Sr isotopic ratios with increasing silica content for the suite of rocks at El Dorado. The MORB field corresponds to the D-MORB and enriched mantle of Salters & Stracke (2004) and Carr et al. (1990) respectively. The SiO_2 content of MORB sources is only schematic. Crustal samples from Guatemala show higher $^{87}Sr/^{86}Sr$ relative to the El Dorado volcanic rocks. The isotopic homogeneity of rocks at El Dorado is striking, independent of rock age or composition, with slightly elevated values relative to an enriched mantle source inferred to be present in the mantle wedge (Carr et al., 1990). A 1-sigma analytical uncertainty is smaller than the symbols size. See figure 3.3 for symbols explanations.

3.6 Magmatic evolution of the El Dorado volcanic rocks

3.6.1 Generation of Miocene volcanic rocks

The trace element and isotope geochemistry of volcanic basement rocks at El Dorado indicate a mantle source compositionally approaching E-MORB (Figure 3.6 and 3.8), with geochemical signatures that potentially indicate a slab and sediment-derived fluid component (e.g., high Ba/Th; see Figure 3.9). Nonetheless, the isotopic composition of volcanic basement rocks is identical to that of Pliocene volcanic rocks with no indication of a different input from subducted sediments (as partial melts) or by assimilation of isotopically elevated crustal rocks. The processes that generated Miocene magmas must be analogous to the models offered by Carr et al. (1990) and Cameron et al. (2002), with a combination of decompression and flux melting in the mantle wedge. The same processes likely account for the generation of Pliocene mafic magmas.

3.6.2 Generation of Pliocene volcanic rocks

The major and trace elements and isotope geochemistry of Miocene volcanic basement rocks overlap with that of mafic and intermediate Pliocene volcanic rocks (Figure 3.3-3.4). This observation rises the idea of recurrence between the Miocene and Pliocene sub-arc magmatic systems, including similar source regions and parent magmas. The Pliocene volcanic sequence, however, is characterized by the generation of voluminous amounts of felsic volcanic rocks. Distinct melt generation processes must therefore explain the origin of Pliocene felsic magmas.

As seen above, the homogeneneity in $^{87}Sr/^{86}Sr$ (likewise Nd and Pb) of the El Dorado volcanic rocks led to the idea of MASH processes during magma genesis (Hildreth and Moorbath, 1988). Annen et al. (2006) showed numerically how magmas of intermediate and felsic composition can be generated in deep crustal hot zones by introducing basaltic sills at the base of the crust and melting previously emplaced igneous rocks or older continental crust. Despite the very limited isotopic composition of volcanic rocks at El Dorado, felsic volcanic rocks appear to form mixing trends (of short extent) on thorogenic and uranogenic diagrams (Figure 3.7b and d), between a low $^{206}Pb/^{204}Pb$ source, represented by a post-mineral Pliocene basaltic lava flow, and a higher $^{206}Pb/^{204}Pb$ source, represented by Miocene volcanic basement rocks. These trends would be consistent with a scenario where felsic magmas are generated by partially melting

previously emplaced sub-arc igneous rocks, isotopically equivalent to the high $^{206}Pb/^{204}Pb$ volcanic basement rocks in the district, by introducing basaltic magmas, isotopically equivalent to the low $^{206}Pb/^{204}Pb$ basaltic lava flow, in deep crustal hot zones (Annen et al., 2006). Since the most primitive magmas have very similar isotopic composition to that of the inferred sub-arc igneous rocks, the latter offers little isotopic leverage, thus generating felsic magmas with limited Pb, Sr and Nd isotopic composition. The Miocene ignimbrites of Nicaragua have also been argued to result from partial melting of previously emplaced sub-arc igneous rocks (Viray, 2003), a process that therefore seems consistent on a regional scale.

Closed system fractional crystallization during ascent and ponding of felsic magmas at higher crustal levels would cause no further changes in isotopic composition (Kleine et al., 2004), but could produce the observed trace element fractionation trends (Figure 3.4).

3.6.3 Crystal fractionation in felsic magmas

The trace elements Zr and Hf illustrate well the effect of magmatic fractionation (Figure 3.3g and h). Mafic to intermediate volcanic rocks show a steep enrichment in Zr and Hf with increasing Th content up to dacitic compositions at which point the trend becomes negative. Fractionation of several accessory minerals in evolved magmas (e.g. zircon, apatite, allunite, monazite) could cause these trends with high partitioning coefficient for the highly incompatible elements (Rollinson, 1993). In the case of felsic volcanic rocks at El Dorado, zircon and apatite would be the most obvious fractionating phases since they were observed in thin section (see Appendix B). Hornblende fractionation could also potentially cause a depletion in Zr in dacitic and rhyolitic melts, with a documented partitioning coefficient up to 4 in hornblende (Rollinson, 1993). Hornblende is a common mafic mineral in felsic rocks at El Dorado and in the Quaternary volcanic arc.

The fractionating mineral assemblage in felsic magmas can be inferred using rare earth element ratios (Figure 3.12). Changes in Sm/Yb among all groups of rocks are relatively small (approx. 2-fold) with considerable overlap between mafic to felsic volcanic rocks. Changes are more apparent in the La/Yb (y-axis) and La/Sm (slope) ratios with a 5-fold and 4-fold increase respectively from mafic and intermediate to felsic

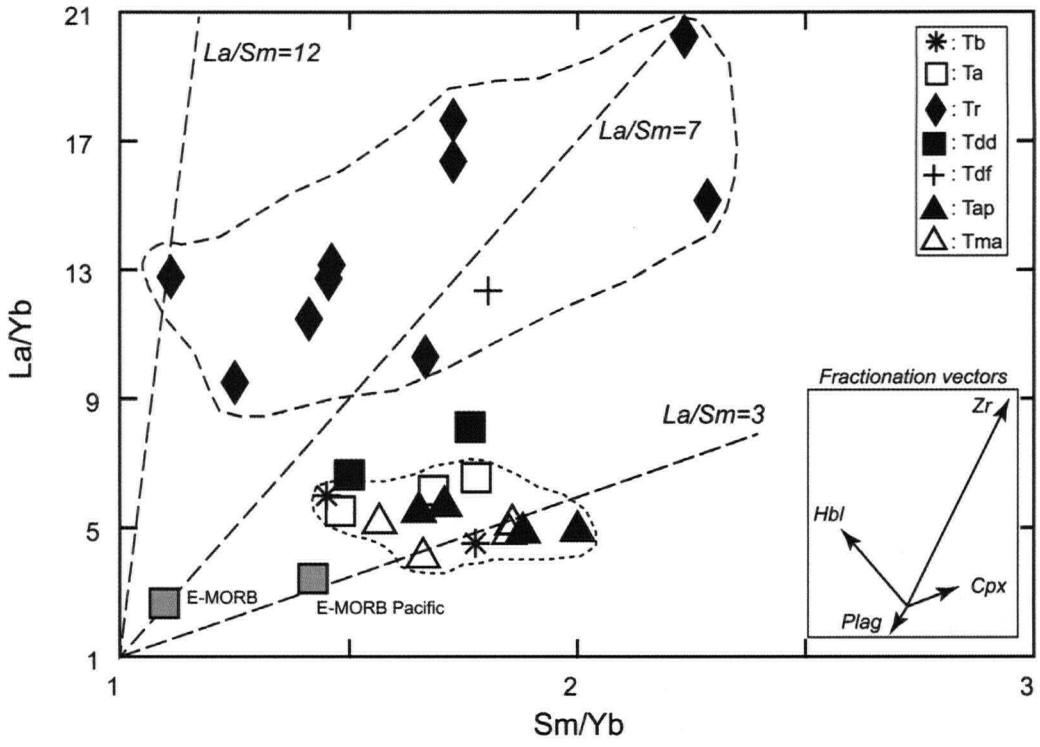

Figure 3.12. La/Yb vs. Sm/Yb ratios for the El Dorado volcanic rocks. Felsic volcanic rocks outlined by the dashed contour show a wider range of rare earth element ratios. The fractionation vectors schematically represent the geochemical effect of fractional crystallization of different phases. The plagioclase and clinopyroxene vectors were calculated with respect to a basaltic composition, with 20% crystallization, whereas the hornblende and zircon vectors were calculated with respect to a rhyolite composition, with 10% and 2% crystallization respectively (partitioning coefficient from GERM database; see text for references). The relative magnitude of each vector is schematic. Pacific and average E-MORB from the GERM supplemental data and Sun and McDonough (1989). A 1-sigma analytical uncertainty is smaller than the symbols size on all diagrams. See figure 3.3 for symbols explanations.

volcanic rocks. Fractionation vectors were calculated using a simple fractional crystallization equation and reported partitioning coefficient of La, Sm, and Yb in selected minerals (GERM partitioning coefficient database). The plagioclase and clinopyroxene vectors were calculated using a basaltic composition (Kd values from Matsui et al., 1977; Villemant et al., 1981; Hack et al. 1994; McKay et al., 1994; and Bindeman et al., 1998), whereas the hornblende and zircon vectors were calculated using a rhyolitic composition (Sisson et al., 1994; Mahood and Hildreth, 1983). Those fractionation vectors are schematically illustrated in the box on Figure 3.12.

All groups of mafic to intermediate volcanic rocks are compositionally similar, approaching the rare earth element content of Pacific E-MORB (Figure 3.12). Changes in geochemistry between genetically related groups of rocks could occur from a combination of clinopyroxene and plagioclase fractionation. Clinopyroxene fractionation occurs at constant La/Sm ratio (along a constant slope). Plagioclase was also likely part of the fractionating mineral assemblage given the negative europium anomalies observed in some volcanic basement rocks (Figure 3.5b), although it would cause very minor changes in the La/Yb and Sm/Yb ratios. Other mineral phases potentially account for the minor changes observed among mafic to intermediate volcanic rocks but are not considered in details here. Slight differences in source geochemistry could also be responsible for some of the observed variations among mafic to intermediate volcanic rocks.

Felsic volcanic rocks (including the rocks of the Pliocene felsic sequences and the Cerro Caballo lava flow facies) show a wider range in La/Yb and Sm/Yb ratios. Relative to mafic and intermediate volcanic rocks, felsic rocks have higher La/Yb and La/Sm, and partially overlapping Sm/Yb values. If felsic magmas were generated by partially melting sub-arc igneous rocks, as suggested by their isotopic composition (see above), the starting REE composition of felsic magmas arguably approached that defined by the cluster of mafic and intermediate volcanic rocks, although different degrees of partial melting could also affect their initial ratio (Figure 3.8). Subsequent fractional crystallization during their ascent and ponding at upper crustal levels could account for the observed changes in REE ratios. Two minerals of interest are found in felsic volcanic rocks at El Dorado: hornblende and zircon. Hornblende is one of the major mafic mineral phases in felsic

volcanic rocks at El Dorado (see Table 3.1; Appendix B), and its fractionation from a rhyolitic magma would drive the residual liquid to higher La/Yb and La/Sm, and lower Sm/Yb (see hornblende vector in box on Figure 3.12). Fractionation of zircon on the other hand would have a contrasting effect, greatly increasing both La/Yb and Sm/Yb ratios of residual liquids. A combination of hornblende and zircon fractionation (not necessarily in conjunction) could potentially produce the range of REE ratios observed in felsic volcanic rocks. Fractionation of other accessory phases such as apatite was not considered here, but would certainly affect the trace element composition of felsic magmas. Plagioclase fractionation may also be responsible for the negative europium anomaly observed among certain felsic rock samples (Figure 3.5d).

3.6.4 Linking tectonic and magmatic events

As mentioned previously, based on the regional distribution of volcanic rock Formations in northern Central America, the Miocene to Pliocene transition was accompanied by a trenchward shift in subduction and magmatic activity (Weyl, 1980). Figure 3.13 schematically illustrates this change in tectonic setting. Carr et al. (1990) showed that the dip of the subducted lithosphere could be correlated with regional variations in the La/Yb ratio of Central American arc lavas (also reflecting the volcanic flux). Since the La/Yb ratio of Miocene and Pliocene mafic volcanic rocks at El Dorado (4-6; figure 3.8) overlap with that of Quaternary volcanic arc lavas in El Salvador (~3-7), the dip in subduction is assumed to have remained constant.

The volcanic basement rocks at El Dorado consists of a >400 meters-thick package of dominantly mafic and intermediate volcanic rocks. Compositionally evolved rocks (i.e. dacite) form a volumetrically minor portion of the volcanic basement rocks (see the manuscript forming the first part of this thesis). During periods of high differential stress, magmas are more likely to erupt with minor dike interaction and ponding at different crustal levels (Takada, 1994). This situation might have prevailed during the period which volcanic basement rocks were emplaced, as schematically illustrated on figure 3.13a. This scenario is used here as a mean to compare the change in tectonic setting between the Miocene and the Pliocene. No inferences are made concerning magmatic and tectonic processes during the Miocene (and prior to?) based on the limited understanding of the volcanic basement stratigraphy on a regional scale.

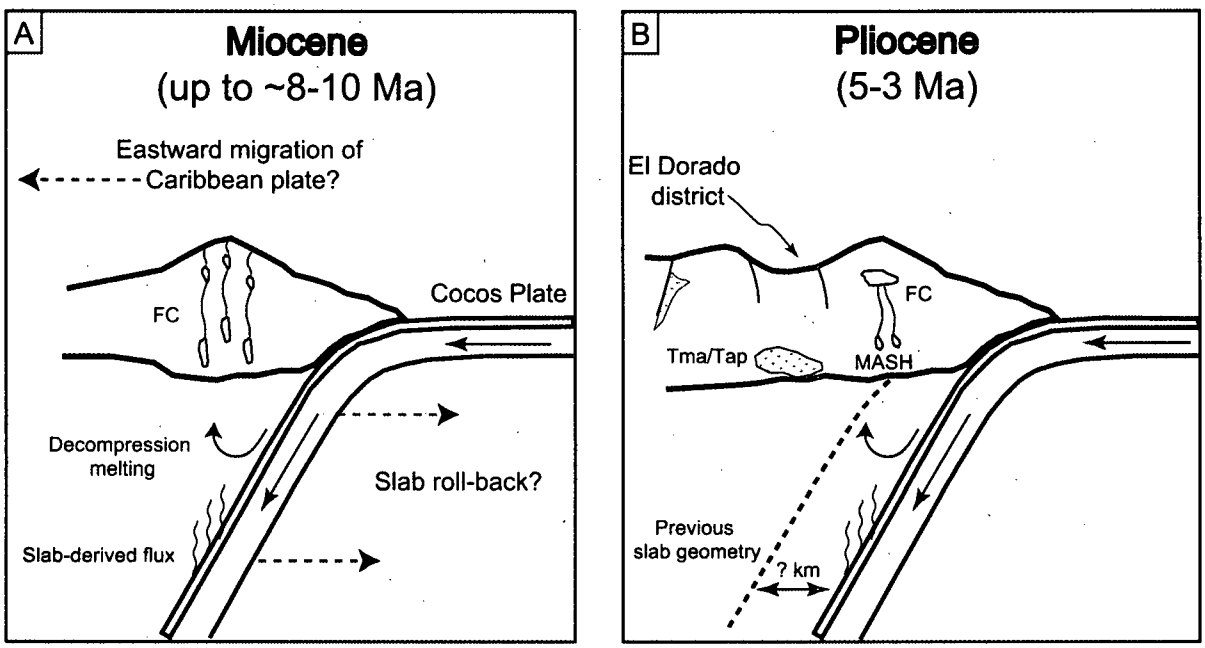

Figure 3.13. Schematic representation of the Central American subduction zone geometry and relative position of the Miocene and Pliocene volcanic arcs. A) Miocene and older (?) magmas were produced from a combination of flux and decompression melting with a possible sediment input. High differential stress possibly promoted the eruption of mafic magmas with limited ponding and differentiation at upper crustal levels (Takada, 1994). B) Felsic magmas were generated by MASH processes in deep crustal hot zones (Hildreth and Moorbath, 1988; Annen et al., 2006). A low differential stress regime during the Pliocene accounts for the formation of evolved upper crustal magma chambers (Takada, 1994), where felsic magmas further differentiated by fractional crystallization.

The Miocene to Pliocene transition was marked by a trenchward shift in subduction zone (Figure 3.13b), and subsequently characterized by a period of dominantly felsic volcanism. During a period of low differential stress (Takada, 1994), dikes are more likely to interact at different crustal levels forming magma chambers. Felsic magmas generated in the lower crust (see above) are likely to have ascended and accumulated in magma chambers at shallow crustal levels where they were allowed to fractionate further. The Pliocene felsic magmatic event is possibly a consequence of changes in the tectonic stress regime following the shift in subduction zone.

3.7 Conclusion

The Caribbean plate margin in the vicinity of the El Dorado district developed in association with two distinct Tertiary magmatic events. The first magmatic event is represented by the dominantly basaltic to andesitic Miocene and older (?) volcanic basement rocks. The second magmatic event developed during the Pliocene following a trenchward shift in subduction and magmatic activity, and is represented by the mafic and intermediate to dominantly felsic Pliocene volcanic rocks found in the district. Pliocene felsic magmas were likely generated by MASH processes at deep crustal levels (Hildreth and Moorbath, 1988) where previously emplaced igneous rocks are partially melted by subsequent magma input producing intermediate to felsic magmas (Annen et al., 2006). The isotope geochemistry of Tertiary magmas was buffered by the mantle, and possibly, by a constant input of hemipelagic sediments and slab-derived fluids, yielding volcanic rocks with homogeneous isotopic composition, independent of rock type and age. The low differential stress conditions, possibly resulting from the plate reconfiguration, allowed felsic magmas to pond in shallow magma chambers, where fractionation of hornblende and zircon (and probably other accessory minerals) likely produced the trace element trends observed in felsic volcanic rocks.

3.8 References

Albrecht, J. L., Walker, J. A., Patino, L. C., and Carr, M. J., 2005, Geochemical history of the Telica volcanic complex, Nicaraguan volcanic front; implications of new data, Abstracts with Programs - Geological Society of America, vol. 37, p. 29.

Annen, C., Blundy, J.D., and Sparks, S.J., 2006, The genesis of intermediate and silicic magmas in deep crustal hot zones, Journal of Petrology, vol. 47, p. 505-539.

Bindeman, I.N., Davis, A.M. and Drake, M.J., 1998, Ion microprobe study of plagioclase-basalt partition experiments at natural concentration levels of trace elements, Geochimica et Cosmochimica Acta, vol. 62, p. 1,175-1,193.

B.f.B., 1974, Mapa Geologico de la Republica de El Salvador 1:500,000, published by the Bundesanstalt für Bodenforschung, Hannover 1974.

Cameron, B.I., 1998, Melt generation and magma evolution in southeastern Guatemala, Ph.D. Thesis, Northern Illinois University. DeKalb. IL, 399 pp.

Cameron, B.I., Walker, J.A., Carr, J.A., Patino, L.C., Matias, O., and Feigenson, M.D., 2002, Flux versus decompression melting at stratovolcanoes in southeastern Guatemala, Journal of Volcanology and Geothermal Research, vol. 119, p. 21-50.

Carr, M.J., and Rose, W.I., (1987), CENTAM-a data base of Central American volcanic rocks, Journal of Volcanology and Geothermal Research Res., vol. 33, p. 239-240.

Carr, M.J., Feigenson, M.D., and Bennett, E.A., 1990, Incompatible element and isotopic evidence for tectonic control of source mixing and melt extraction along the Central American arc, Contributions to Mineralogy and Petrology, vol. 105, p. 369-380.

Catastro e inventario de recursos naturales, 1972, Geology of Western Nicaragua, Operations consultant's final report for 1968-1970 surveys, vol. 4, 221 p.

Hack, P.J., Nielsen, R.L. and Johnston, A.D., 1994, Experimentally determined rare-Earth element and Y partitioning behavior between clinopyroxene and basaltic liquids at pressures up to 20 Kbar, Chemical Geology, vol. 117, p. 89-105.

Hawkesworth, C.J., Turner, S.P., McDermott, F., Peate, D.W., and van Calsteren, P., 1997, U-Th isotopes in arc magmas: implications for element transfer from the subducted crust, Science, vol. 276, p. 551-555.

Hart, S.R., Blusztajn, J., Dick, H.J.B., Meyer, P.S. and Muehlenbachs, K., 1999, The fingerprint of seawater circulation in a 500-meter section of ocean crust gabbros, Geochimica et Cosmochimica Acta, vol. 63, p. 4,059-4,080.

Hildreth, W. and Moorbath, S., 1988, Crustal contributions to arc magmatism in the Andes of central Chile, Contributions to Mineralogy and Petrology, vol. 98, p. 455-489.

Hofmann, A.W., 2003, Sampling Mantle Heterogeneity through Oceanic Basalts: Isotopes and Trace Elements, *In*: Treatise on Geochemistry, vol. 2, p. 61-101, Editor: R.W. Carlson, Executive Editors: H.D. Holland and K.K. Turekian, 568 pp.

Kleine, T., Mezger, K., Zimmermann, U., Munker, C., and Bahlburg, H., 2004, Crustal evolution along the Early Ordivician proto-Andean margin of Gondwana: trace element and isotope evidence from the Complejo Igneo Pocitos (Northwest Argentina), Journal of Geology, vol. 112, p. 503-520.

Le Bas, M .J., Le Maitre, R .W., Streckeisen, A., and Zanettin, B.A., 1986, Chemical classification of volcanic rocks based on the total alkali-silica diagram, Journal of Petrology, vol. 27, p. 745-750.

Lundin, B.S., Sigurdsson, H., Carey, S. N., and Jordan, B. R., 2003, Petrology of Tertiary ignimbrite province in Central America, Geological Society of America, Northeastern Section, 38th annual meeting, Halifax, NS, Canada.

Mahood, G.A. and Hildreth, E.W., 1983, Large partition coefficients for trace elements in high-silica rhyolites, Geochimica et Cosmochimica Acta, vol. 47, p. 11-30.

Matsui, Y., Onuma, N., Nagasawa, H., Higuchi, H. and Banno, S., 1977, Crystal structure control in trace element partition between crystal and magma, Tectonics, vol. 100, p. 315-324.

McDonough, W.F., and Sun, S.-s., 1995, The composition of the Earth, Chemical Geology, vol. 120, p. 223-253.

McKay, G., Le, L., Wagstaff, J. and Crozaz, G., 1994, Experimental partitioning of rare Earth elements and strontium: constraints on petrogenesis and redox conditions during crystallization of Antarctic angrite Lewis Cliff 86010, Geochimica et Cosmochimica Acta, vol. 58, p. 2,911-2,919.

Meschede, M., and Frisch, W., 1998, A plate-tectonic model for the Mesozoic and Early Cenozoic history of the Caribbean plate, Tectonophysics, v. 296, p. 269-291.

Patino, L.C., Carr, M.J., and Feigenson, M.D., 2000, Local and regional variations in Central American arc lavas controlled by variations in subducted sediment input, Contributions to Mineralogy and Petrology, vol. 138, p. 265-283.

Peccerillo, A., and Taylor, S.R., 1976, Geochemistry of Eocene calc-alkaline volcanic rocks from the Kastamonu area, northern Turkey, Contributions to Mineralogy and Petrology, vol. 58, p. 63-81.

Pretorius, W., Weis, D., Williams, G., Hanano, D., Kieffer, B., and Scoates, J., 2006, Complete trace elemental characterization of granitoid (USGS G-2, GSP-2) reference materials by high resolution inductively coupled plasma-mass spectrometry, Geostandards and Geoanalytical Research, vol. 30, p. 39-54.

Pichler, H., and Weyl, R., 1973, Petrochemical aspects of Central American Magmatism, International Journal of Earth Sciences, vol. 62, p. 357-396.

Plank, T., 2005, Constraints from thorium/lanthanum on sediment recycling at subduction zones and the evolution of the continents, Journal of Petrology, vol. 46, p. 921-944.

Plank, T., and Langmuir, C.H., 1998, The geochemical composition of subducting sediment and its consequences for the crust and mantle, Chemical Geology, vol. 145, p. 325-394.

Reagan, M.K., Morris, J.D., Herrstrom, E.A., and Murrell, M.T., 1994, Uranium series and beryllium isotope evidence for an extended history of subduction modification of the mantle below Nicaragua, Geochimica et Cosmochimica Acta, vol. 58, p. 4199-4212.

Reynolds, J.H., 1977, Tertiary Volcanic Stratigraphy of Northern Central America, Master's Thesis, Dartmouth College, Hanover, N.H., 89pp.

Reynolds, J.H., 1980, Late Tertiary Volcanic Stratigraphy of Northern Central America, Bulletin Volcanologique, vol. 43, p. 601-607.

Rollinson, H., 1993, Using geochemical data: evaluation, presentation, interpretation. Longman group UK limited, 352 pp.

Rudnick, R.L., and Fountain, D.M., 1995, Nature and composition of the continental crust: a lower crustal perspective, Reviews in Geophysics, vol. 33, p. 267-309.

Salters, V. and Stracke, A., 2004, Composition of the depleted mantle, Geochemistry, Geophysics, Geosystems, vol. 5, No. 5, Q05004.

Schilling, J., Fontignie, D., Blichert-Toft, J., Kingsley, R. and Tomza, U., 2003, Pb-Hf-Nd-Sr isotope variations along the Galapagos Spreading Center (101°--83°W): Constraints on the dispersal of the Galapagos mantle plume, Geochemistry, Geophysics, Geosystems, vol. 4, No. 10, 8512.

Sisson, T.W., 1994, Hornblende-Melt Trace-Element Partitioning Measured by Ion Microprobe, Chemical Geology, vol. 117, p. 331-344.

Stacey, J.S., and Krammers, J.D., 1975, Approximation of terrestrial lead isotope evolution by a two-stage model, Earth and Planetary Science Letters, vol. 26, p. 207-221.

Sun, S.S. and McDonough, W.F., 1989, Chemical and isotopic systematics of oceanic basalts; implications for mantle composition and processes, In: Magmatism in the ocean basins, Saunders, A.D. and Norry, M.J. (Editors), Geological Society of London, London, 398 pp.

Takada, A., 1994, The influence of regional stress and magmatic input on styles of monogenetic and polygenetic volcanism, Journal of Geophysical Research, vol. 99, p. 13,563-13,573.

Taylor, S.R. and McLennan, S.M., 1995, The geochemical evolution of the continental crust, Reviews in Geophysics, vol. 33, p. 241-265.

Villemant, B., Jaffrezic, H., Joron, J.L. and Treuil, M., 1981, Distribution Coefficients of Major and Trace-Elements - Fractional Crystallization in the Alkali Basalt Series of Chaine-Des-Puys (Massif Central, France), Geochimica et Cosmochimica Acta, vol. 45, p. 1,997-2,016.

Viray, E.L.E., 2003, Origin and evolution of the Nicaraguan silicic ash-flow sheets, Master's thesis, Michigan State University, 100 pp.

Walker, J.A., Patino, L.C., Cameron, B.I., and Carr, M.J., 2000, Petrogenetic insights provided by compositional transects across the Central American arc: Southeastern Guatemala and Honduras, Journal of Geophysical Research, vol. 105, p. 18,949-18,963.

Weis, D., Kieffer, B., Maerschalk, C., Pretorius, W., Barling, J., 2005, High-precision Pb-Sr-Nd-Hf isotopic characterization of USGS BHVO-1 and BHVO-2 reference materials, Geochemistry, Geophysics, Geosystems, vol. 6, 10 pp.

Weyl, R., 1980, Geology of Central America: Berlin-Stuttgart, Gebruder Borntraeger, 371 pp.

Wiesemann, Gerd, 1975, Remarks on the geologic structure of the Republic of El Salvador, Central America, Mitt. Geol. Paläont. Inst. Univ. Hamburg, vol. 44, p. 557-574.

CHAPTER 4

CONCLUSIONS AND SUGGESTIONS FOR FUTURE WORK

4.1 Conclusion

The recent field mapping, new geochronology and geochemical data allowed to build the volcanic framework to the El Dorado epithermal vein system, constrain the timing of vein formation, and understand the geochemical evolution of volcanic rocks.

Two compositionally distinct groups of volcanic rocks are found at El Dorado: Miocene and possibly older dominantly mafic to intermediate volcanic basement rocks, overlain and cross-cut by Pliocene and possibly younger mafic to dominantly felsic volcanic rocks, with a ~5 m.y. time unconformity separating the two groups. Vein formation and mineralization is poorly constrained between ~4.7-4.0 Ma, and likely occurred closer to the lower limit as suggested by field relationships and geochronology of bracketing rock units. The onset of felsic volcanism marks the waning stages of hydrothermal activity in the district, and continued for several hundred thousand years following ore formation (~4.0-3.3 Ma). Pliocene and possibly younger post-mineral mafic to intermediate lava flows of represent the last stages of volcanic activity in the district.

The current outcrops from north to south at El Dorado appear to represent an oblique cross section through the volcanic and hydrothermal system associated with the low-sulfidation epithermal vein system. The topographic gradient, the southward younging of the stratigraphic sequence, and the shallowing of the epithermal vein system to the south suggests that the entire district may have been tilted and/or downdropped southward possibly shortly after vein formation. The east-striking Titihuappa fault zone on the extreme south, defines the northwestern margin of the Rio Titihuappa basin, potentially representing a volcano-tectonic depression. The Pliocene felsic pyroclastic and sedimentary rocks found on the plains south of the Titihuappa River, defining the fault zone, potentially represent caldera fill, and the rhyolite domes following the northern margin of the River are analogous to ring dike intrusions.

The sub-arc mantle source that generated primary magmas during the Miocene and Pliocene is compositionally constrained between depleted- and enriched-MORB sources. The isotope geochemistry of Tertiary magmas was buffered by the mantle, and possibly, by a constant input of hemipelagic sediments and slab/sediment-derived fluids, yielding volcanic rocks with homogeneous isotopic composition, independent of rock

type and age. Pliocene felsic magmas were likely generated by the partial melting of previously emplaced sub-arc igneous rocks by introducing basaltic magmas, of similar isotopic composition, in deep crustal hot zones (Annen et al., 2006). This process is consistent with felsic magma generation on a regional scale (Viray, 2003). Felsic magmas further differentiated in upper crustal magma chambers by fractional crystallization of hornblende and zircon (and possibly other accessory minerals).

Of general interest to this study is the possible link between tectonic, magmatic and metallogenic events in northern Central America. Based on the general distribution of volcanic rock Formations on a regional scale, the Miocene to Pliocene transition appears to have been accompanied with a trenchward shift in subduction and associated magmatic activity (Weyl, 1980). Could tectonic movements affect the nature of magmatism and metallogenesis in the region? Large-scale changes in tectonic configuration and magmatic processes have been linked to distinct metallogenic events along the Andean margin (e.g. Kay and Mpodozis, 2001). Kesler (1978) also suggested a genetic link between ignimbritic felsic volcanic rocks and precious metal epithermal vein deposits in several mining districts of Central America. The change in tectonic stress regime associated with plate reconfiguration during the Pliocene appear to have been followed by the formation of long-lived, upper crustal magma chamber(s), which in turn provided a heat engine to the once active hydrothermal system, and a possible source of metals. Extensive felsic volcanism associated with the magma chamber(s), possibly associated with caldera formation, eventually suppressed hydrothermal activity at El Dorado. Is this scenario viable at other mining districts of Central America (e.g. El Limon, Nicaragua)? The complex volcanic history and metallogenic evolution of the Central American region still has much to be unveiled.

4.2 Suggestion for future work

The current study opens doors to many areas of future academic research from the district to the regional scale:

-A detailed paragenesis study and additional dating of veins and volcanic rocks would be needed in order to understand the complexity of epithermal mineralization at El Dorado.

-A more complete study of hydrothermal alteration would also be a key missing element.

-Regional mapping and additional geochronology of volcanic rocks would constrain the temporal and spatial evolution of volcanism and tectonic processes that occurred during the Miocene to Pliocene transition.

-Dating of known epithermal deposits found in the region would help to constrain the extent of the Pliocene metallogenic event.

4.3 References

Kay, S.M., and Mpodozis, C., 2001, Central Andean ore deposits linked to evolving shallow subduction systems and thickening crust, GSA Today, vol. 11, p. 4-9.

Kesler, S.E., 1978, Metallogenesis of the Caribbean region, Journal of the Geological Society of London, vol. 135, p. 429-441.

Annen, C., Blundy, J.D., and Sparks, S.J., 2006, The genesis of intermediate and silicic magmas in deep crustal hot zones, Journal of Petrology, vol. 47, p. 505-539.

Viray, E.L.E., 2003, Origin and evolution of the Nicaraguan silicic ash-flow sheets, Master's thesis, Michigan State University, 100 pp.

Weyl, R., 1980, Geology of Central America: Berlin-Stuttgart, Gebruder Borntraeger, 371 pp.

APPENDIX A

^{40}AR-^{39}AR GEOCHRONOLOGY DATA SET

Laser[1] Power (%)	Isotope Ratios									
	$^{40}Ar/^{39}Ar$	$^{38}Ar/^{39}Ar$	$^{37}Ar/^{39}Ar$	$^{36}Ar/^{39}Ar$	Ca/K	Cl/K	$\%^{40}Ar$	$\%^{39}Ar$	$^{40}Ar^*/^{39}Ar_K$	Age±2σ
MR05-74, plagioclase, J = 0.002537±0.000004; volume $^{39}Ar_K = 61.26 \times 10^{-13}cm^3$, integrated age = 10.50±2.67 (2σ)										
<2>	59.934±0.022	0.066±0.038	1.360±0.026	0.197±0.028	3.857	0.003	95.7	31.56	2.553±1.607	11.65±7.31
<2.2>	20.097 0.036	0.029 0.093	4.179 0.034	0.064 0.038	11.894	0.001	89.02	24.77	2.178 0.740	9.94 3.37
<2.5>	27.929 0.031	0.038 0.094	16.923 0.034	0.097 0.042	48.877	0.001	91.65	11.31	2.332 1.154	10.64 5.25
<2.8>	24.276 0.013	0.049 0.117	20.935 0.017	0.086 0.039	60.75	0.004	89.8	8.77	2.478 1.015	11.31 4.61
<3.2>	18.435 0.009	0.042 0.146	15.879 0.015	0.065 0.044	45.815	0.003	87.8	9	2.228 0.866	10.17 3.94
<3.6>	16.106 0.013	0.043 0.154	19.005 0.019	0.057 0.069	55.038	0.004	82.5	7.21	2.790 1.176	12.72 5.34
<4>	12.807 0.009	0.036 0.121	20.205 0.016	0.052 0.054	58.591	0.003	92.15	7.37	0.972 0.854	4.44 3.90
MR05-55, plagioclase, J =0.002538±0.000004; volume $^{39}Ar_K = 67.04 \times 10^{-13}cm^3$, integrated age = 5.22±0.96 (2σ)										
<2>	55.530±0.014	0.217±0.073	9.394±0.022	0.193±0.054	26.948	0.038	95.19	2.5	2.634±3.034	12.02±13.80
<2.4>	68.464 0.015	0.117 0.046	9.163 0.021	0.233 0.038	26.243	0.014	96.61	6.28	2.311 2.546	10.55 11.59
<2.8>	13.072 0.008	0.057 0.065	8.574 0.015	0.047 0.049	24.53	0.008	93.58	12.61	0.806 0.692	3.69 3.16
<3.2>	2.956 0.007	0.062 0.059	7.766 0.015	0.010 0.072	22.196	0.011	53.87	22.21	1.295 0.213	5.92 0.97
<3.6>	2.146 0.007	0.064 0.067	7.530 0.014	0.008 0.066	21.947	0.011	53.25	25.15	0.937 0.162	4.28 0.74
<4>	1.792 0.006	0.061 0.037	7.981 0.014	0.007 0.050	23.273	0.01	41.83	31.25	0.977 0.104	4.47 0.47
MR05-58, plagioclase, J = 0.002538±0.000004; volume $^{39}Ar_K = 43.96 \times 10^{-13}cm^3$, integrated age = 5.67±1.54 (2σ)										
<2>	401.978±0.014	0.319±0.063	4.881±0.024	1.350±0.024	14.514	0.01	98.12	3.28	7.580±8.409	34.38±37.78
<2.3>	26.991 0.008	0.043 0.165	6.093 0.017	0.092 0.054	18.109	0.002	96.18	7.57	0.992 1.468	4.54 6.70
<2.7>	6.079 0.007	0.036 0.056	5.574 0.016	0.020 0.066	16.541	0.004	81.03	22.26	1.099 0.387	5.03 1.77
<3.1>	4.128 0.006	0.049 0.062	6.172 0.015	0.014 0.061	18.326	0.007	77.49	24.23	0.871 0.256	3.98 1.17
<3.5>	2.470 0.008	0.064 0.091	6.954 0.014	0.008 0.147	20.845	0.011	53.68	21.04	1.038 0.364	4.74 1.66
<4>	1.943 0.009	0.050 0.063	8.044 0.015	0.007 0.175	24.147	0.008	35.54	21.62	1.117 0.351	5.11 1.60

[1] "<" indicates step used in plateau age calculations, ">'" indicates step used in inverse correlation calculations.

Neutron flux monitors: 24.36 Ma MAC-83 biotite (Sandeman et al. 1999); 28.02 Ma FCs (Renne et al., 1998)

Isotope production ratios: $(^{40}Ar/^{39}Ar)_K=0.0302$, $(^{37}Ar/^{39}Ar)_{Ca}=1416.4306$, $(^{36}Ar/^{39}Ar)_{Ca}=0.3952$, $Ca/K=1.83(^{37}Ar_{Ca}/^{39}Ar_K)$.

Laser[1] Power (%)	Isotope Ratios									
	$^{40}Ar/^{39}Ar$	$^{38}Ar/^{39}Ar$	$^{37}Ar/^{39}Ar$	$^{36}Ar/^{39}Ar$	Ca/K	Cl/K	$\%^{40}Ar$	$\%^{39}Ar$	$^{40}Ar^*/^{39}Ar_K$	Age±2σ
MR04-37, biotite, J =0.002531±0.000004; volume $^{39}Ar_K$ = 876.43 x $10^{-13}cm^3$, integrated age = 3.51±0.08 (2σ)										
<2>	196.205±0.012	0.279±0.094	0.123±0.203	0.657±0.027	0.317	0.033	97.64	0.17	4.462±4.893	20.26±22.09
<2.3>	48.659 0.010	0.150 0.071	0.072 0.070	0.164 0.037	0.186	0.024	97.32	0.32	1.200 1.709	5.47 7.78
<2.6>	8.615 0.005	0.173 0.044	0.047 0.091	0.026 0.060	0.121	0.035	86.16	0.85	1.016 0.467	4.63 2.13
<3>	3.245 0.005	0.208 0.033	0.028 0.080	0.008 0.085	0.073	0.044	65.27	2.62	0.978 0.197	4.46 0.90
<3.4>	1.540 0.004	0.199 0.017	0.011 0.038	0.003 0.051	0.029	0.042	45.66	10.58	0.762 0.040	3.47 0.18
<3.8>	1.184 0.004	0.197 0.010	0.007 0.054	0.001 0.055	0.018	0.042	33.4	25.64	0.736 0.024	3.36 0.11
<4.3>	1.175 0.004	0.197 0.012	0.005 0.049	0.001 0.038	0.012	0.042	31.88	34.89	0.754 0.016	3.44 0.07
<4.8>	1.128 0.006	0.200 0.014	0.008 0.021	0.001 0.048	0.02	0.043	28.74	17.67	0.738 0.019	3.37 0.09
<5.3>	1.246 0.005	0.195 0.016	0.005 0.087	0.002 0.145	0.013	0.042	25.56	5.34	0.772 0.070	3.52 0.32
<5.8>	1.811 0.008	0.200 0.035	0.008 0.225	0.004 0.126	0.022	0.043	34.81	1.62	0.787 0.140	3.59 0.64
<7>	5.720 0.012	0.196 0.096	0.010 0.470	0.014 0.246	0.027	0.041	14.69	0.29	2.175 1.009	9.90 4.58
MR04-37 run#2, biotite, J = 0.002531±0.000004; volume $^{39}Ar_K$ = 686.56 x $10^{-13}cm^3$, integrated age = 3.54±0.10 (2σ)										
<2>	226.997±0.015	0.270±0.048	0.115±0.148	0.765±0.029	0.311	0.026	98.25	0.29	3.943±5.835	17.92±26.38
<2.3>	30.329 0.014	0.174 0.075	0.055 0.157	0.101 0.045	0.15	0.032	95.7	0.47	1.249 1.288	5.69 5.86
<2.7>	5.843 0.010	0.221 0.028	0.036 0.072	0.017 0.067	0.098	0.047	79.24	1.59	1.146 0.329	5.23 1.50
<3.1>	1.991 0.008	0.215 0.020	0.020 0.101	0.004 0.086	0.054	0.046	56.69	5.11	0.808 0.106	3.69 0.48
<3.5>	1.290 0.009	0.203 0.014	0.006 0.056	0.002 0.051	0.017	0.043	37.56	20.8	0.768 0.027	3.50 0.12
<3.9>	1.141 0.008	0.201 0.013	0.005 0.054	0.001 0.052	0.015	0.043	31.16	34.67	0.751 0.021	3.42 0.09
<4.3>	1.157 0.007	0.199 0.016	0.003 0.118	0.001 0.045	0.008	0.042	31.93	15.64	0.746 0.019	3.40 0.09
<5>	1.101 0.007	0.196 0.013	0.004 0.071	0.001 0.080	0.01	0.042	27.8	21.43	0.757 0.028	3.45 0.13

[1] "<" indicates step used in plateau age calculations, ">'" indicates step used in inverse correlation calculations.

Neutron flux monitors: 24.36 Ma MAC-83 biotite (Sandeman et al. 1999); 28.02 Ma FCs (Renne et al., 1998)

Isotope production ratios: $(^{40}Ar/^{39}Ar)_K$=0.0302, $(^{37}Ar/^{39}Ar)_{Ca}$=1416.4306, $(^{36}Ar/^{39}Ar)_{Ca}$=0.3952, Ca/K=1.83$(^{37}Ar_{Ca}/^{39}Ar_K)$.

Laser[1] Power (%)	Isotope Ratios									
	$^{40}Ar/^{39}Ar$	$^{38}Ar/^{39}Ar$	$^{37}Ar/^{39}Ar$	$^{36}Ar/^{39}Ar$	Ca/K	Cl/K	$\%^{40}Ar$	$\%^{39}Ar$	$^{40}Ar^*/^{39}Ar_K$	Age±2σ
MR04-24, biotite, J =0.002533±0.000004; volume $^{39}Ar_K$ = 632.44 x $10^{-13}cm^3$, integrated age = 3.65±0.18 (2σ)										
<2>	32.440±0.009	0.158±0.026	0.014±0.123	0.108±0.025	0.032	0.029	96.65	2.2	1.034±0.779	4.72±3.55
<2.2>	22.031 0.008	0.158 0.037	0.015 0.109	0.073 0.033	0.032	0.03	95.56	2.21	0.915 0.705	4.17 3.21
<2.5>	13.583 0.012	0.172 0.022	0.009 0.099	0.044 0.026	0.021	0.034	94.51	4.6	0.696 0.337	3.18 1.54
<2.8>	6.636 0.012	0.188 0.026	0.008 0.092	0.020 0.026	0.02	0.039	86.24	6.67	0.848 0.155	3.87 0.71
<3.1>	4.351 0.008	0.195 0.016	0.009 0.067	0.012 0.020	0.023	0.041	79.61	11.36	0.827 0.073	3.78 0.33
<3.4>	3.227 0.009	0.192 0.016	0.007 0.069	0.008 0.028	0.017	0.041	73.89	12.57	0.778 0.068	3.55 0.31
<3.7>	2.823 0.009	0.217 0.017	0.144 0.021	0.007 0.032	0.363	0.046	71.01	16.37	0.759 0.069	3.46 0.32
<4>	2.755 0.007	0.193 0.017	0.008 0.064	0.007 0.024	0.018	0.041	68.15	12.28	0.803 0.047	3.67 0.22
<4.4>	2.519 0.007	0.194 0.018	0.005 0.098	0.006 0.041	0.011	0.041	63.71	12.4	0.834 0.071	3.81 0.32
<4.9>	2.319 0.006	0.193 0.014	0.004 0.088	0.005 0.043	0.008	0.041	62.67	10.21	0.773 0.069	3.53 0.31
<5.5>	1.986 0.006	0.191 0.015	0.004 0.098	0.004 0.051	0.009	0.04	55.55	9.14	0.768 0.066	3.51 0.30
MR04-24 run#2, biotite, J = 0.002533±0.000004; volume $^{39}Ar_K$ = 367.32 x $10^{-13}cm^3$, integrated age = 3.56±0.18 (2σ)										
<2>	30.125±0.020	0.167±0.042	0.014±0.086	0.102±0.025	0.038	0.031	98.35	3.24	0.466±0.738	2.13±3.37
<2.3>	6.584 0.013	0.183 0.028	0.007 0.168	0.020 0.033	0.017	0.038	89.09	8.62	0.682 0.199	3.12 0.91
<2.7>	2.642 0.014	0.189 0.021	0.003 0.098	0.006 0.039	0.008	0.04	67.65	21.23	0.818 0.074	3.73 0.34
<3.1>	1.973 0.015	0.189 0.019	0.002 0.119	0.004 0.024	0.006	0.04	57.96	31.33	0.793 0.034	3.62 0.15
<3.5>	1.600 0.013	0.188 0.017	0.002 0.143	0.003 0.051	0.005	0.04	48.89	24.97	0.778 0.044	3.55 0.20
<3.9>	1.846 0.009	0.186 0.022	0.003 0.182	0.004 0.096	0.008	0.039	52	8.83	0.827 0.102	3.78 0.46
<4.5>	4.072 0.011	0.192 0.033	0.014 0.238	0.012 0.130	0.037	0.04	75.86	1.77	0.879 0.453	4.01 2.06

[1] "<" indicates step used in plateau age calculations, ">'" indicates step used in inverse correlation calculations.

Neutron flux monitors: 24.36 Ma MAC-83 biotite (Sandeman et al. 1999); 28.02 Ma FCs (Renne et al., 1998)

Isotope production ratios: $(^{40}Ar/^{39}Ar)_K$=0.0302, $(^{37}Ar/^{39}Ar)_{Ca}$=1416.4306, $(^{36}Ar/^{39}Ar)_{Ca}$=0.3952, Ca/K=1.83($^{37}Ar_{Ca}/^{39}Ar_K$).

Laser[1] Power (%)	Isotope Ratios									
	$^{40}Ar/^{39}Ar$	$^{38}Ar/^{39}Ar$	$^{37}Ar/^{39}Ar$	$^{36}Ar/^{39}Ar$	Ca/K	Cl/K	$\%^{40}Ar$	$\%^{39}Ar$	$^{40}Ar^*/^{39}Ar_K$	Age±2σ
MR04-50, biotite, J =0.002534±0.000004; volume $^{39}Ar_K$ = 478.77 x $10^{-13}cm^3$, integrated age = 3.68±0.30 (2σ)										
<2>	145.730±0.008	0.230±0.056	0.058±0.165	0.490±0.021	0.14	0.03	98.65	0.74	1.903±2.937	8.68±13.36
<2.2>	43.578 0.007	0.117 0.046	0.017 0.130	0.144 0.025	0.041	0.018	96.98	2.86	1.270 1.079	5.80 4.92
<2.4>	43.906 0.010	0.135 0.048	0.018 0.135	0.145 0.023	0.043	0.022	96.69	2.11	1.401 0.960	6.39 4.37
<2.6>	48.373 0.009	0.183 0.043	0.022 0.098	0.162 0.024	0.053	0.032	98.27	1.59	0.793 1.131	3.62 5.16
<2.9>	17.724 0.008	0.158 0.030	0.014 0.106	0.058 0.020	0.035	0.031	95.39	4.32	0.771 0.343	3.52 1.56
<3.2>	10.438 0.009	0.153 0.032	0.020 0.050	0.033 0.025	0.048	0.031	92.93	7.56	0.695 0.240	3.17 1.10
<3.5>	7.245 0.007	0.156 0.022	0.052 0.040	0.022 0.022	0.127	0.032	88.55	9.95	0.783 0.146	3.58 0.66
<3.8>	5.001 0.005	0.187 0.021	0.345 0.015	0.015 0.024	0.851	0.039	84.03	18.72	0.758 0.102	3.46 0.46
<4.1>	3.520 0.008	0.156 0.018	0.103 0.016	0.009 0.024	0.255	0.032	77.46	17.5	0.745 0.067	3.40 0.30
<4.5>	2.812 0.008	0.153 0.016	0.022 0.054	0.007 0.030	0.055	0.032	69.31	14.64	0.803 0.060	3.67 0.28
<5>	2.329 0.007	0.152 0.016	0.035 0.034	0.005 0.044	0.087	0.032	63.79	16.42	0.781 0.068	3.57 0.31
<5.5>	4.266 0.005	0.160 0.031	0.087 0.055	0.011 0.056	0.215	0.033	75.86	3.58	0.899 0.189	4.11 0.86
MR04-50 run#2, biotite, J =0.002534±0.000004; volume $^{39}Ar_K$ = 486.26 x $10^{-13}cm^3$, integrated age = 3.86±0.34 (2σ)										
<2>	81.881±0.007	0.199±0.030	0.059±0.050	0.276±0.018	0.163	0.031	98.23	2.65	1.420±1.442	6.48±6.57
<2.3>	32.587 0.008	0.182 0.020	0.037 0.031	0.109 0.018	0.103	0.034	97.6	5.81	0.753 0.576	3.44 2.63
<2.6>	15.062 0.011	0.167 0.020	0.013 0.070	0.048 0.021	0.035	0.033	93.41	7.57	0.961 0.304	4.39 1.39
<2.9>	7.073 0.012	0.161 0.020	0.027 0.026	0.022 0.022	0.076	0.033	88.51	14.16	0.781 0.142	3.57 0.65
<3.2>	4.960 0.010	0.295 0.015	0.943 0.016	0.014 0.025	2.698	0.064	81.86	20.25	0.869 0.105	3.97 0.48
<3.5>	3.936 0.009	0.167 0.015	0.096 0.018	0.011 0.024	0.274	0.035	78.54	25.56	0.813 0.077	3.71 0.35
<4>	4.008 0.010	0.162 0.023	0.033 0.034	0.011 0.027	0.095	0.033	78.72	24.01	0.821 0.088	3.75 0.40

[1] "<" indicates step used in plateau age calculations, ">'" indicates step used in inverse correlation calculations.

Neutron flux monitors: 24.36 Ma MAC-83 biotite (Sandeman et al. 1999); 28.02 Ma FCs (Renne et al., 1998)

Isotope production ratios: $(^{40}Ar/^{39}Ar)_K$=0.0302, $(^{37}Ar/^{39}Ar)_{Ca}$=1416.4306, $(^{36}Ar/^{39}Ar)_{Ca}$=0.3952, Ca/K=1.83$(^{37}Ar_{Ca}/^{39}Ar_K)$.

Laser[1] Power (%)	Isotope Ratios									
	$^{40}Ar/^{39}Ar$	$^{38}Ar/^{39}Ar$	$^{37}Ar/^{39}Ar$	$^{36}Ar/^{39}Ar$	Ca/K	Cl/K	$\%^{40}Ar$	$\%^{39}Ar$	$^{40}Ar^*/^{39}Ar_K$	Age±2σ
MR04-58, biotite, J = 0.002535±0.000004; volume $^{39}Ar_K$ = 1182.02 x $10^{-13}cm^3$, integrated age = 3.39±0.07 (2σ)										
<2>	239.298±0.014	0.318±0.057	0.050±0.185	0.810±0.025	0.129	0.035	98.9	0.18	2.571±4.878	11.72±22.16
<2.3>	54.101 0.009	0.132 0.058	0.025 0.086	0.182 0.024	0.064	0.019	98.32	0.57	0.859 1.259	3.92 5.75
<2.6>	10.738 0.006	0.128 0.050	0.015 0.115	0.033 0.031	0.038	0.025	89.49	1.04	1.032 0.300	4.71 1.37
<3>	3.382 0.005	0.145 0.017	0.010 0.110	0.009 0.031	0.025	0.03	73.95	4.45	0.813 0.080	3.71 0.36
<3.5>	1.563 0.007	0.149 0.016	0.002 0.104	0.003 0.035	0.006	0.031	50.23	17.16	0.730 0.030	3.33 0.14
<4>	1.219 0.006	0.147 0.011	0.002 0.077	0.002 0.032	0.004	0.03	36.66	33.05	0.730 0.016	3.34 0.07
<4.5>	1.108 0.007	0.145 0.010	0.001 0.078	0.001 0.037	0.003	0.03	29.84	28.51	0.732 0.015	3.34 0.07
<5>	1.088 0.008	0.147 0.013	0.001 0.172	0.001 0.076	0.003	0.03	27.63	15.03	0.726 0.027	3.32 0.12
MR04-58 run#2, biotite, J =0.002535±0.000004; volume $^{39}Ar_K$ = 700.37 x $10^{-13}cm^3$, integrated age = 3.66±0.14 (2σ)										
2	173.421±0.013	0.230±0.052	0.050±0.160	0.585±0.023	0.104	0.024	97.68	0.45	4.023±3.671	18.31±16.62
2.2	25.106 0.014	0.124 0.048	0.037 0.085	0.083 0.038	0.085	0.022	92	0.84	1.960 0.917	8.94 4.17
2.5	6.872 0.010	0.139 0.032	0.018 0.078	0.021 0.058	0.045	0.028	84.53	2.61	1.016 0.365	4.64 1.66
2.8	2.916 0.009	0.150 0.024	0.012 0.069	0.007 0.038	0.033	0.031	66.73	7.33	0.926 0.082	4.23 0.37
<3.1>	1.522 0.032	0.149 0.030	0.006 0.072	0.003 0.060	0.016	0.031	47.66	17.62	0.758 0.061	3.46 0.28
<3.4>	1.258 0.029	0.148 0.028	0.005 0.074	0.002 0.063	0.015	0.031	35.09	24.86	0.779 0.044	3.56 0.20
<4>	1.149 0.028	0.146 0.024	0.004 0.073	0.001 0.058	0.011	0.03	31.91	29.17	0.746 0.037	3.41 0.17
<5>	1.201 0.013	0.150 0.024	0.001 0.140	0.002 0.062	0.003	0.031	34.75	17.12	0.742 0.033	3.39 0.15

[1] "<" indicates step used in plateau age calculations, ">'" indicates step used in inverse correlation calculations.

Neutron flux monitors: 24.36 Ma MAC-83 biotite (Sandeman et al. 1999); 28.02 Ma FCs (Renne et al., 1998)

Isotope production ratios: $(^{40}Ar/^{39}Ar)_K$=0.0302, $(^{37}Ar/^{39}Ar)_{Ca}$=1416.4306, $(^{36}Ar/^{39}Ar)_{Ca}$=0.3952, Ca/K=1.83$(^{37}Ar_{Ca}/^{39}Ar_K)$.

Laser[1] Power (%)	Isotope Ratios									
	$^{40}Ar/^{39}Ar$	$^{38}Ar/^{39}Ar$	$^{37}Ar/^{39}Ar$	$^{36}Ar/^{39}Ar$	Ca/K	Cl/K	$\%^{40}Ar$	$\%^{39}Ar$	$^{40}Ar^*/^{39}Ar_K$	Age±2σ
MR05-73, biotite, J = 0.002537±0.000004; volume $^{39}Ar_K$ = 1233.43 x $10^{-13}cm^3$, integrated age = 3.94±0.32 (2σ)										
<2>	50.921±0.006	0.115±0.032	0.046±0.050	0.171±0.018	0.113	0.016	98.06	2.07	0.953±0.887	4.36±4.05
<2.2>	40.976 0.004	0.121 0.019	0.026 0.054	0.137 0.017	0.065	0.019	97.61	4.12	0.946 0.691	4.32 3.15
<2.4>	26.178 0.006	0.136 0.023	0.022 0.051	0.087 0.018	0.054	0.024	96.51	4.57	0.878 0.440	4.02 2.01
<2.6>	16.225 0.006	0.155 0.020	0.016 0.050	0.052 0.020	0.04	0.03	93.98	5.48	0.939 0.306	4.29 1.40
<2.8>	10.532 0.006	0.166 0.015	0.013 0.042	0.033 0.021	0.032	0.033	91.01	5.41	0.903 0.202	4.13 0.92
<3>	7.830 0.007	0.169 0.017	0.014 0.037	0.024 0.019	0.033	0.035	88.99	7.64	0.821 0.137	3.75 0.63
<3.2>	7.326 0.006	0.173 0.023	0.016 0.050	0.022 0.020	0.04	0.036	88.34	4.79	0.804 0.131	3.68 0.60
<3.4>	7.730 0.007	0.175 0.018	0.019 0.036	0.023 0.027	0.046	0.036	87.99	5.52	0.880 0.191	4.03 0.87
<3.7>	8.215 0.004	0.175 0.015	0.024 0.024	0.025 0.017	0.059	0.036	89.56	17.29	0.824 0.129	3.77 0.59
<4>	8.253 0.004	0.179 0.012	0.026 0.025	0.025 0.019	0.066	0.037	89.94	15.37	0.796 0.142	3.64 0.65
<4.3>	8.602 0.004	0.185 0.012	0.032 0.022	0.026 0.017	0.079	0.038	89.71	11.38	0.849 0.134	3.88 0.61
<4.6>	9.112 0.005	0.192 0.013	0.037 0.037	0.028 0.019	0.093	0.04	89.6	7.36	0.907 0.157	4.15 0.72
<4.9>	8.615 0.005	0.200 0.017	0.049 0.028	0.026 0.022	0.121	0.042	88.8	4.34	0.913 0.172	4.17 0.79
<5.5>	7.083 0.005	0.224 0.026	0.084 0.035	0.021 0.024	0.209	0.047	85.58	4.65	0.966 0.151	4.41 0.69
MR05-73 run#2, biotite, J = 0.002537±0.000004; volume $^{39}Ar_K$ = 1332.42 x $10^{-13}cm^3$, integrated age = 3.88±0.38 (2σ)										
<2>	51.424±0.004	0.126±0.024	0.030±0.044	0.174±0.017	0.085	0.018	98.85	2.89	0.560±0.843	2.56±3.85
<2.2>	28.017 0.007	0.139 0.019	0.018 0.037	0.093 0.019	0.051	0.025	96.97	6.26	0.819 0.514	3.74 2.35
<2.3>	19.266 0.005	0.154 0.020	0.014 0.044	0.063 0.017	0.038	0.029	95.65	6.24	0.808 0.314	3.69 1.43
<2.4>	15.701 0.011	0.165 0.025	0.013 0.046	0.051 0.020	0.037	0.032	94.3	5.53	0.865 0.303	3.95 1.39
<2.5>	12.581 0.009	0.167 0.018	0.012 0.062	0.040 0.024	0.034	0.033	92.13	5.57	0.960 0.281	4.39 1.28
<2.6>	10.470 0.013	0.170 0.020	0.013 0.073	0.033 0.025	0.035	0.035	90.43	5.25	0.971 0.233	4.44 1.06
<2.7>	10.602 0.017	0.170 0.026	0.014 0.068	0.033 0.027	0.04	0.034	90.21	5.69	1.008 0.259	4.61 1.18
<2.9>	9.676 0.009	0.170 0.015	0.017 0.028	0.030 0.021	0.047	0.035	90.65	11.33	0.875 0.182	4.00 0.83
<3.1>	9.338 0.013	0.174 0.015	0.018 0.032	0.029 0.022	0.049	0.036	90.85	13.06	0.825 0.193	3.77 0.88
<3.3>	8.849 0.012	0.176 0.020	0.018 0.028	0.028 0.020	0.051	0.036	91.14	15.87	0.755 0.154	3.45 0.70
<3.8>	9.511 0.005	0.182 0.012	0.023 0.030	0.030 0.018	0.066	0.037	90.89	13.09	0.837 0.152	3.83 0.69
<4.2>	9.293 0.005	0.204 0.014	0.051 0.018	0.029 0.022	0.143	0.042	89.77	9.24	0.921 0.183	4.21 0.84

[1] "<" indicates step used in plateau age calculations, ">" indicates step used in inverse correlation calculations.

Neutron flux monitors: 24.36 Ma MAC-83 biotite (Sandeman et al. 1999); 28.02 Ma FCs (Renne et al., 1998)

Isotope production ratios: $(^{40}Ar/^{39}Ar)_K$=0.0302, $(^{37}Ar/^{39}Ar)_{Ca}$=1416.4306, $(^{36}Ar/^{39}Ar)_{Ca}$=0.3952, Ca/K=1.83$(^{37}Ar_{Ca}/^{39}Ar_K)$.

Laser[1] Power (%)	Isotope Ratios									
	$^{40}Ar/^{39}Ar$	$^{38}Ar/^{39}Ar$	$^{37}Ar/^{39}Ar$	$^{36}Ar/^{39}Ar$	Ca/K	Cl/K	$\%^{40}Ar$	$\%^{39}Ar$	$^{40}Ar^*/^{39}Ar_K$	Age±2σ
MR05-54, plagioclase, J =0.002538±0.000004; volume $^{39}Ar_K$ = 25.33 x $10^{-13}cm^3$, integrated age = 11.66±2.26 (2σ)										
2	104.684±0.016	0.310±0.062	14.875±0.022	0.356±0.027	44.33	0.054	95.19	9.89	5.126±2.622	23.32±11.85
<2.4>	36.913 0.011	0.170 0.059	18.846 0.017	0.129 0.028	55.921	0.031	93.24	27.04	2.511 1.048	11.46 4.77
<2.8>	12.344 0.008	0.130 0.055	16.301 0.015	0.048 0.061	48.241	0.025	87.89	25.74	1.457 0.880	6.66 4.01
<3.2>	9.022 0.009	0.142 0.091	16.568 0.017	0.035 0.069	49.219	0.028	69.8	15.62	2.583 0.734	11.79 3.34
<3.6>	9.264 0.015	0.152 0.127	15.131 0.021	0.038 0.103	45.158	0.031	63.15	9.13	3.100 1.171	14.14 5.32
<4>	6.938 0.010	0.107 0.098	20.898 0.016	0.032 0.109	63.074	0.02	61.55	12.59	2.430 1.061	11.09 4.83
MR05-75 run#1, adularia, J =0.002538±0.000006; volume $^{39}Ar_K$ = 162.49 x $10^{-13}cm^3$, integrated age = 5.05±1.06 (2σ)										
2	357.953±0.006	0.307±0.055	0.028±0.152	1.208±0.018	0.072	0.015	98.76	2.82	4.410±6.229	20.08±28.21
<2.3>	106.625 0.008	0.117 0.038	0.022 0.068	0.360 0.020	0.058	0.008	98.64	5.59	1.417 1.958	6.48 8.93
<2.6>	24.205 0.007	0.040 0.037	0.044 0.065	0.077 0.022	0.117	0.002	92.97	11.52	1.651 0.485	7.54 2.21
<2.9>	6.462 0.007	0.020 0.101	0.275 0.025	0.019 0.037	0.728	0	84.66	15.6	0.925 0.209	4.23 0.95
<3.2>	6.865 0.006	0.019 0.060	0.291 0.025	0.021 0.048	0.77	0	85.78	11.45	0.900 0.294	4.11 1.34
<3.7>	2.188 0.006	0.014 0.082	0.036 0.037	0.005 0.061	0.096	0	54.08	19.12	0.882 0.082	4.04 0.38
<4.2>	2.281 0.006	0.015 0.081	0.010 0.082	0.005 0.090	0.026	0	60.93	18.67	0.781 0.139	3.57 0.64
<5>	8.199 0.008	0.025 0.064	0.084 0.027	0.025 0.036	0.221	0.001	87.57	11.59	0.949 0.263	4.34 1.20
<6>	17.839 0.007	0.035 0.145	0.206 0.079	0.058 0.029	0.544	0.002	93.58	3.64	1.048 0.487	4.79 2.22

[1] "<" indicates step used in plateau age calculations, ">" indicates step used in inverse correlation calculations.

Neutron flux monitors: 24.36 Ma MAC-83 biotite (Sandeman et al. 1999); 28.02 Ma FCs (Renne et al., 1998)

Isotope production ratios: $(^{40}Ar/^{39}Ar)_K$=0.0302, $(^{37}Ar/^{39}Ar)_{Ca}$=1416.4306, $(^{36}Ar/^{39}Ar)_{Ca}$=0.3952, Ca/K=1.83$(^{37}Ar_{Ca}/^{39}Ar_K)$.

Laser[1] Power (%)	Isotope Ratios									
	$^{40}Ar/^{39}Ar$	$^{38}Ar/^{39}Ar$	$^{37}Ar/^{39}Ar$	$^{36}Ar/^{39}Ar$	Ca/K	Cl/K	$\%^{40}Ar$	$\%^{39}Ar$	$^{40}Ar^*/^{39}Ar_K$	Age±2σ
MR05-75 run#2, adularia, J = 0.002538±0.000006; volume $^{39}Ar_K$ = 120.18 x $10^{-13}cm^3$, integrated age = 4.92±0.72 (2σ)										
2	24.675±0.005	0.045±0.034	0.167±0.028	0.079±0.021	0.437	0.004	93.98	24.71	1.446±0.481	6.61± 2.19
2.2	9.957 0.014	0.029 0.076	0.503 0.026	0.031 0.040	1.318	0.002	88.22	13.05	1.098 0.358	5.02 1.63
2.5	7.442 0.015	0.020 0.070	0.460 0.024	0.022 0.038	1.204	0	83.44	17.86	1.156 0.247	5.29 1.13
2.8	4.963 0.005	0.019 0.094	0.647 0.019	0.015 0.036	1.694	0	83.65	16.22	0.730 0.157	3.34 0.72
<3.3>	5.526 0.006	0.018 0.097	0.311 0.020	0.016 0.069	0.815	0	81.02	15.28	0.955 0.324	4.37 1.48
<3.8>	7.880 0.006	0.022 0.137	0.097 0.031	0.025 0.040	0.254	0.001	89.86	9.94	0.717 0.292	3.28 1.33
<4.5>	19.749 0.012	0.029 0.204	0.145 0.078	0.063 0.072	0.377	0	89.43	2.63	1.852 1.318	8.46 6.01
5.5	39.934 0.044	0.081 0.440	0.230 0.156	0.167 0.171	0.59	0.005	120.48	0.31	-4.768 8.267	-21.97 38.32
MR05-75 run#3, adularia, J = 0.002538±0.000006; volume $^{39}Ar_K$ = 409.22 x $10^{-13}cm^3$, integrated age = 4.65±0.46 (2σ)										
2	317.123±0.008	0.315±0.024	0.238±0.039	1.073±0.019	0.677	0.023	98.78	1.52	3.880±5.660	17.68±25.66
2.1	9.371 0.010	0.039 0.037	0.067 0.053	0.028 0.040	0.188	0.005	82.27	3.54	1.608 0.335	7.35 1.53
<2.4>	8.916 0.012	0.026 0.057	0.044 0.038	0.028 0.025	0.125	0.002	89.12	9.15	0.936 0.206	4.28 0.94
<2.7>	10.399 0.011	0.021 0.032	0.016 0.085	0.033 0.022	0.042	0	90.17	9.64	0.989 0.211	4.52 0.96
<3>	6.413 0.008	0.017 0.092	0.013 0.046	0.019 0.028	0.035	0	84.25	12.31	0.975 0.157	4.46 0.72
<3.3>	3.841 0.011	0.016 0.052	0.014 0.054	0.010 0.030	0.04	0	74.36	20.01	0.949 0.088	4.34 0.40
<3.6>	3.861 0.009	0.017 0.052	0.041 0.036	0.010 0.032	0.117	0	75.23	14.05	0.918 0.096	4.20 0.44
<4>	2.998 0.014	0.017 0.033	0.016 0.039	0.007 0.030	0.046	0	67.45	18.57	0.937 0.068	4.29 0.31
<4.5>	2.386 0.009	0.014 0.076	0.041 0.029	0.005 0.095	0.116	0	57.72	11.21	0.958 0.150	4.38 0.68

[1] "<" indicates step used in plateau age calculations, ">'" indicates step used in inverse correlation calculations.

Neutron flux monitors: 24.36 Ma MAC-83 biotite (Sandeman et al. 1999); 28.02 Ma FCs (Renne et al., 1998)

Isotope production ratios: $(^{40}Ar/^{39}Ar)_K$=0.0302, $(^{37}Ar/^{39}Ar)_{Ca}$=1416.4306, $(^{36}Ar/^{39}Ar)_{Ca}$=0.3952, Ca/K=1.83$(^{37}Ar_{Ca}/^{39}Ar_K)$.

APPENDIX B

PETROGRAPHY OF SELECTED VOLCANIC ROCKS

Basement rocks: lower lava sequence

MR04-53

South El Dorado andesite lava flow

This rock is a porphyritic andesite lava flow (Figure B.1a). It contains ~20% subhedral to anhedral zoned plagioclase phenocrysts up to 2.2 mm across, ~5% subhedral to anhedral clinopyroxene phenocrysts up to 3 mm across, ~1-2% subhedral orthopyroxene phenocrysts <1 mm across, and ~5% magnetite grains up to 0.5 mm across.

The rock groundmass contains ~30% plagioclase microlites <40 μm long, and 15-20% <10 μm disseminated magnetite grains.

MR04-92

North El Dorado andesite lava flow (drill hole)

This rock is a porphyritic andesite lava flow (Figure B.1b). It contains ~20% subhedral, partly altered (mainly sericite) plagioclase phenocrysts up to 3.5 mm across. Crystals are synneused in aggregates of up to 8 grains. Partly to completely chloritized subhedral pyroxene phenocrysts up to 1.8 mm across represent 5-8% of the rock. Magnetite grains up to 0.6 mm across represent ~5% of the rock.

The groundmass contains ~30% up to 80 μm long plagioclase microlites, and ~10% disseminated magnetite <20μm across. The groundmass is strongly altered to a mixture of clay minerals and chlorite. The rock sample is cut by three sinuous 0.1 to 0.6 mm-wide, calcite + quartz microveinlets.

Basement rocks: porphyritic domes and dikes

MR04-06

North Minita andesite dome

This rock is a porphyritic andesite. It contains ~10% subhedral, partly sericitized plagioclase phenocrysts up to 4 mm across, ~3-5% subhedral, completely chloritized pyroxene micro-phenocrysts <0.5 mm across, and ~3% magnetite up to 0.5 mm across.

The clay and K-feldspar altered groundmass contains 20-30% plagioclase microlites <30 μm long, 7-10% disseminated magnetite grains <10 μm across, and 7-10% calcite filling pore space.

MR04-03

Central El Dorado andesite porphyry (drill hole)

This rock is a strongly altered andesite porphyry (Figure B.1c). The section contains 20-25% subhedral plagioclase phenocrysts up to 4 mm across. Phenocrysts are commonly synneused in aggregates of several grains. They are partially to completely replaced by sericite and calcite. Pseudomorphs of euhedral pyroxene phenocrysts up to 0.5 mm across represent about 2% of the rock. They have been replaced by an assemblage of chlorite and clay minerals. The section contains about 7% subhedral prismatic magnetite up to 0.4 mm across. The rock groundmass contains about 50% plagioclase flow aligned microlites less than 0.2 mm in length. Alteration of the groundmass consists of disseminated calcite, chlorite and clay minerals.

MR04-95

Central El Dorado andesite (drill hole)

This thin section represents the style of alteration associated with a deep zone of strong silicification, and vein stockworks in the mafic basement rock of the Hacienda Vieja area (Figure B.1d). The section is obliquely cut by a 1.5 cm wide crustiform banded veinlet and less than half of the section consists of strongly altered, light green andesite. The andesite appears to have been brecciated and cemented by 10 μm to 150 μm size granular quartz, prior to having been cut by a later generation of veinlets. Where preserved, the original texture in the andesite reveal partly to completely sericitized and calcite-replaced subhedral to euhedral plagioclase phenocrysts up to about 0.7 mm in length. Former subhedral pyroxene phenocrysts up to 0.6 mm across have been completely replaced by chlorite, calcite and clay minerals. They locally form aggregates of a few grains welded together. Subhedral magnetite phenocrysts up to 0.25 mm across represent about 1% of the andesite.

The crustiform banded veinlet is composed of at least ten distinct bands that range in width from 0.2 to about 1.5 mm across. The bands consist of alternating very fine (4-20μm) and slightly coarser grained (25-150 μm) granular quartz. Grains are anhedral and form tight mosaics. The central portion of the veinlet includes druzy quartz. Opaque minerals represent a very small fraction (<<0.1%) of the quartz veinlet and appear to be principally pyrite (?) grains up to about 5μm across. A late calcite microveinlet up to 0.25 mm across, cuts irregularly across the quartz veinlet.

Plan de Minas volcaniclastic sequence

MR04-96

Plan de Minas epiclastic rock (drill hole)

This rock is a highly altered heterolithic conglomerate (Figure B.1e). It contains over 50% rounded porphyritic andesite fragments ranging in size between 0.1 and 5 mm (up to a few centimeters in hand sample). The section contains about 10% subhedral to anhedral plagioclase phenocrysts fragments less than 1.5 mm long, partially replaced by calcite and sericite. It contains one quartz crystal fragment 0.15 mm across, and 1-2% chlorite crystal fragments up to 1 mm across.

A fine-grained matrix forms the remaining of the rock and is completely recrystallized to a mosaic of quartz and K-feldspar crystals. The sample is cut by a ~1 centimeter-wide crustiform banded quartz veinlet.

Cerro Caballo dome facies

MR04-42

Cerro Caballo summit

This rock is a coarse-grained porphyritic dacite (Figure B.1f). It contains 7-10% euhedral zoned plagioclase phenocrysts up to 5 mm across. Crystals are synneused in aggregates up to 5 grains. Subhedral orthopyroxene phenocrysts up to 1.5 mm across represent 2-3% of the rock. Completely replaced hornblende pseudomorphs up to 1.2 mm long represent ~2% of the rock. The crystals are replaced by a combination of clays and

Fe-oxides that produces a smoky appearance. Magnetite crystals up to 0.5 mm across represent 1-2% of the rock. Glomerophyric inclusions up to ~5 mm across represent a few percent of the rock.

The rock groundmass is composed of at least 50% of plagioclase microlites <140 μm long. Up to 1-2% rusty red rutitle/titanite (?) is found disseminated in the groundmass, in phenocrysts, and along microfractures. Fine-grained Fe-oxides less than 20 μm across represent ~2-5% of the groundmass. Accessory apatite is also found in the groundmass.

MM29

North base of Cerro Caballo

This rock is a coarse porphyritic andesite. It contains ~7% euhedral zoned plagioclase phenocrysts up to 5 mm across that form synneused aggregates up to 5 grains. Subhedral orthopyroxene phenocrysts up to 1 mm across represent ~5% of the rock. They are partly to completely replaced by "smoky" reaction rims as described in the previous sample. Smoky hornblende pseudomorphs up to ~0.5 mm across represent ~1% of the rock. Magnetite crystals up to ~0.5 mm across represent ~1% of the rock. The thin section contains a large glomerophyric inclusion a few centimeters across. The inclusion contains the above phenocryst assemblage in a microcrystalline groundmass composed of plagioclase and magnetite laths 50-250 μm long.

The rock groundmass is composed of a finer-grained assemblage (crystals up to ~80 μm) similar to that of the glomerophyric inclusion.

MR04-43

Cerro Flor intrusive dacite

This rock is a strongly altered flow-banded (vertically in outcrop) dacite that hosts the Cerro Flor vein (see attached geological map). The rock contains ~10% subhedral to anhedral zoned plagioclase phenocrysts up to 3 mm across, ≤1% anhedral quartz crystals up to 0.5 mm across. Completely replaced (clays and oxides) subhedral hornblende phenocrysts up to ~1.5 mm across represent ~1% of the rock.

The groundmass is strongly replaced by a patchy texture of quartz and feldspar that form mosaics of crystals up to 0.1 mm across. The rock is strongly stained by red hematite. Discontinuous micro-veinlets <1 mm follow the flow banding.

Cerro Caballo lava flow facies

MR04-75

Plan de Minas dacite lava flow

This rock is a strongly foliated (thin section), flow folded and brecciated (outcrop scale) dacite/rhyolite (geochem) (Figure B.1g). It contains 7-10% strongly zoned subhedral plagioclase phenocrysts up to 3 mm across, ~1% up to 2 mm long subhedral hornblende phenocrysts, and ~1% magnetite crystals up to 0.5 mm across. The rock groundmass is strongly recrystallized (feldspar + quartz + clay), with a patchy texture, and forms continuous flow bands. The rock contains one glomerophyric inclusion ~1 cm across.

The alteration and texture are very similar to MR04-94 and could possibly be part of the same unit.

MR04-79

Plan de Minas dacite lava flow

This rock is a strongly altered spherulitic dacite/rhyolite (geochem) that forms part of the NW end of the Nance Dulce ridge (Figure B.1h). Subhedral zoned plagioclase phenocrysts (up to 3 mm) represent ~7% of the rock. Synneused plagioclase crystals are found in aggregates of 2-4 grains. Rare broken quartz phenocrysts represent less than ~1% of the rock. Remnant subhedral hornblende phenocrysts up to 1 mm long represent 1-2% of the rock. These crystals are completely replaced by clays (?), feldspar and rimed by opaque oxides. Magnetite crystals up to 0.5 mm across represent 1-2% of the rock.

The rock groundmass is silicified and recrystallized to a combination of quartz and feldspar (?). The groundmass is entirely masked by spherulites. Lithophysae filled with mosaics of quartz and K-feldspar (the rock was readily stained by acid) crystals up to 0.15 mm across represent ~10% of the thin section.

The rock could potentially represent a tuff or a lava flow. It is impossible to make any interpretation with this sample alone.

MR04-94

Dacite breccia (drill hole)

This rock is a strongly altered, flow-banded dacite (geochem) breccia. The rock contains ~5% strongly replaced plagioclase phenocrysts and rare quartz phenocryst fragments. The rock groundmass is completely recrystallized (feldspars + clay?) with a patchy texture.

The breccia matrix represents 10-20% of the rock and consists of a fine-grained aggregate of crystals fragments and recrystallized groundmass. The sample is cut by several discontinuous quartz micro-veinlets <1 mm across.

MR04-23

Dacite breccia ridge

This rock sample represents a flow banded dacite fragment that forms part of a chaotic breccia. The rock contains 5-7% subhedral, strongly zoned plagioclase phenocrysts reaching 3.5 mm across. Minor sericite replaces the phenocrysts along microfractures. Angular fragments of quartz crystals reaching 3.5 mm across represent less than 1% of the rock. Pseudomorphs of hornblende phenocrysts up to 1.6 mm across represent less than 1% of the rock. They have been completely replaced by a combination of clay, quartz and K-feldspar crystals. Subhedral to anhedral opaque oxides up to 0.6 mm across represent 1% of the rock.

The flow banded groundmass has been partly to completely replaced by a mosaic of equant quartz and K-feldspar crystals that reach up to 0.15 mm across. Plagioclase microlites up to about 50 μm in length, where visible, represent most of the groundmass. Remnant spherulites are found locally. Rounded domains up to 3 mm across, partly filled with equant quartz and K-feldspar crystals, represent up to 5% of the rock. They possibly represent lithophysal cavities or replaced spherulites. Hematite is found along micro-fractures.

Platy andesites

MM13

South Avila platy andesite

This rock is a porphyritic andesite. It contains ~20% euhedral to subhedral plagioclase phenocrysts up to 4.5 mm across. Plagioclase crystals are synneused with pyroxene in aggregates up to 12 grains. Subhedral pyroxene phenocrysts up to ~1 mm across represent ~7% of the rock. Magnetite crystals up to 0.4 mm across represent ~3% of the rock.

The rock groundmass consist of randomly orientated <40 μm long plagioclase microlites and ~20% magnetite grains up to ~20 μm.

MR04-19

Plan de Minas platy andesite

This rock is a crystal-rich andesite (Figure B.1i). Euhedral to subhedral plagioclase phenocrysts up to 2 mm across represent 15-20% of the rock and gradually decrease in size to the groundmass (microlite size). Grains are found individually or in synneused aggregates of several crystals. The rock contains ~7% subhedral pyroxene phenocrysts up to ~1.5 mm across that are occasionally found in synneused aggregates with plagioclase phenocrysts. Magnetite crystals up to 0.6 mm across represent ~2% of the rock.

The rock groundmass is crowded with plagioclase micro-phenocrysts and microlites with a gradation in crystal size. The groundmass contains up to ~10% pyroxene micro-phenocrysts and equal amounts of magnetite grains. Crystals are randomly orientated.

Pliocene felsic rocks

MR04-24

Cerro Avila dacite dome

This rock is a porphyritic dacite. The rock contains 10-15% subhedral plagioclase phenocrysts up to 4 mm across, 2-3% anhedral, resorbed quartz crystals up to 1 mm across, 2-3% fresh, subhedral prismatic hornblende up to 7 mm long, <1% subhedral biotite flakes up to 0.6 mm long, and 2-3% subhedral magnetite up to 1.2 mm across.

The partly devitrified glass groundmass contains 10-15% plagioclase microlites up to 20 μm in length.

LC19

San Matias rhyolite dike

This rock is a finely flow-banded rhyolite dike (Figure B.1j). It contains about 5% euhedral to subhedral zoned plagioclase phenocrysts up to up to ~2 mm across, 1-2% anhedral quartz up to ~1 mm across, 3-4% subhedral biotite phenocrysts up to 2 mm long, and <1% equant magnetite crystals up to ~0.2 mm across.

The rock groundmass is consists of recrystallized volcanic glass (mainly feldspar), and contains ~10% primary plagioclase microlites up to ~0.1 mm long.

MR04-37

Cerro Alto rhyolite dome

This rock is a porphyritic rhyolite. It contains 10-15% plagioclase phenocrysts up to 6 mm across. Grains are synneused in aggregates of 5 of more crystals. Partially resorbed quartz eyes up to 2 mm across represent ~2% of the rock. Euhedral to subhedral hornblende phenocrysts up to 6 mm long represent ~5% of the rock.

The partly recrystallized groundmass (quartz and feldspar) contains 10-20% plagioclase microlites <80 μm long, and ~10% disseminated grains of rusty red hematite replaced (?) magnetite. Mosaic quartz fills ~5% pore space (original vesicles?).

MR04-16

Cerro Los Jesuses rhyolite plugs

This rock is a massive to subtly flow-banded rhyolite. It contains 7-10% subhedral to highly resorbed quartz crystals up to 2 mm across, ~2% subhedral zoned plagioclase phenocrysts up to 2 mm across, ~5% subhedral biotite phenocrysts up to ~1 mm long, and <1% magnetite up to 0.3 mm across.

The rock groundmass is slightly recrystallized (mainly feldspar?) volcanic glass which preserved a spherulitic texture.

MR04-01

Central El Dorado rhyolite dike (drill hole)

This rock is a glassy rhyolite dike. It contains ~2% subhedral to anhedral commonly resorbed quartz crystals <3 mm across, ~5-7% euhedral to subhedral plagioclase phenocrysts up to 4 mm across, <1% euhedral to subhedral K-feldspar phenocrysts <1 mm across, ~1-2% euhedral hornblende phenocrysts <2 mm across, <1% subhedral orthopyroxene phenocrysts <1 mm across, <1% subhedral biotite flakes <1 mm long, ~1% magnetite <0.5 mm across, accessory apatite and zircons.

The rock groundmass is fresh glass, with a prominent cleavage following subtle flow banding. Feldspar microlites up to ~100 μm long represent ~10% of the groundmass. Sericitization of the groundmass locally occurs along fractures.

MR04-50

Cerro La Tabla rhyolite lava flow

This rock is a glassy rhyolite lava flow (Figure B.1k). It contains 2-3% anhedral commonly resorbed quartz crystals up to 4 mm across, ~7% euhedral to anhedral plagioclase phenocrysts up to 6 mm across, <1% subhedral K-feldspar <1mm across, 2-3% euhedral hornblende phenocrysts up to 6 mm across, ~1-2% euhedral to subhedral orthopyroxene phenocrysts <1mm across, <1% biotite flakes <0.6 mm across, ~1% magnetite up to 0.5 mm across, accessory apatite and zircons.

The rock groundmass is fresh glass, with a subtle flow banding and locally perlitic texture. Feldspar microlites up to ~100 μm long represent ~10% of the groundmass.

MR04-58

Cerro Alto summit rhyolite tuff

This rock is a finely foliated rhyolite crystal tuff (Figure B.1 l). The rock contains 5-7% partly resorbed anhedral quartz phenocrysts up to 1.5 mm across, ~3-5% subhedral zoned plagioclase phenocrysts (synneused in aggregates of 3-4 grains or as individual crystals) up to ~2 mm across, ~3% biotite flakes up to ~1 mm long, and <1% equant magnetite up to ~0.2 mm across. Accessory minerals include apatite.

The rock groundmass is strongly recrystallized to mosaics of quartz and feldspar crystals ranging from sub-micron to 60 μm across. The groundmass preserves spherulitic textures and up to ~1 mm long glass shards.

Veins and hydrothermal breccias

MR04-39

Hydrothermal breccia South El Dorado

This rock is a fragment supported breccia. The breccia is confined to a meter wide zone hosted in rhyolite dome rock. It contains at least 70% angular to sub-rounded fragments reaching up to 1 cm across. Fragments boundaries are generally sharp but locally blend with interstitial material. The section contains about 5% broken angular, resorbed to subhedral quartz crystals that reach up to about 1.2 mm across. These crystals are mostly found inside fine-grained rhyolite fragments, but are also found as individual fragments.

The breccia matrix consists of finely laminated, up to 20 μm-size particles that have been recrystallized to equant quartz crystals. Some fragments reveal faint shapes that may represent their original fragmented nature, possibly as pyroclastic rocks. The fragment wraps around the edges larger clasts possibly suggesting that the material was not entirely consolidated at the time it was incorporated in the breccia, possibly as a fine sediment that filled pore spaces.

Interstices to fragments are coated by druzy, euhedral quartz crystal that reach up to 0.2 mm in length. Locally, voids were subsequently filled by a mosaic of equant quartz crystals up to about 50 μm across. A few percent of goethite/jarosite fill interstices.

MR04-60

El Porvenir hydrothermal breccia

This rock is a fragment supported hydrothermal breccia (Figure B.1m). It contains one large finely banded quartz vein fragment a few centimeters across, about 30-40% sub-rounded strongly altered and silicified plagioclase-phyric andesite fragments up to 2 mm across, ~7-10% angular quartz crystal fragments <0.5 mm across, and 10-15% clay replaced and locally silicified spherulitic tuff (?) fragments.

The breccia cement represents up to 40-50% of the rock and consists of mosaic and druzy quartz crystals up to 300 μm across. Pore spaces make up <5% of the breccia. A 2 mm wide quartz micro-veinlet cross-cuts the breccia.

MR04-97

Nance Dulce vein

This sample is a crustiform banded quartz/adularia vein that yielded good gold grades (Figure B.1n and o). The thin section is composed of multiple, sub-millimeter parallel bands. In hand specimen, the bands vary from opaque milky white/grey to translucent grey. The former are distinctly stained by the acid solution for K-feldspar.

Ore minerals represent a minor portion of the vein (<1%) and are generally very fine grained (<50 μm). Fine-grained, adularia rich bands tend to contain more sulfides and other ore minerals (up to ~1-2%), including pyrite, chalcopyrite, acanthite and gold.

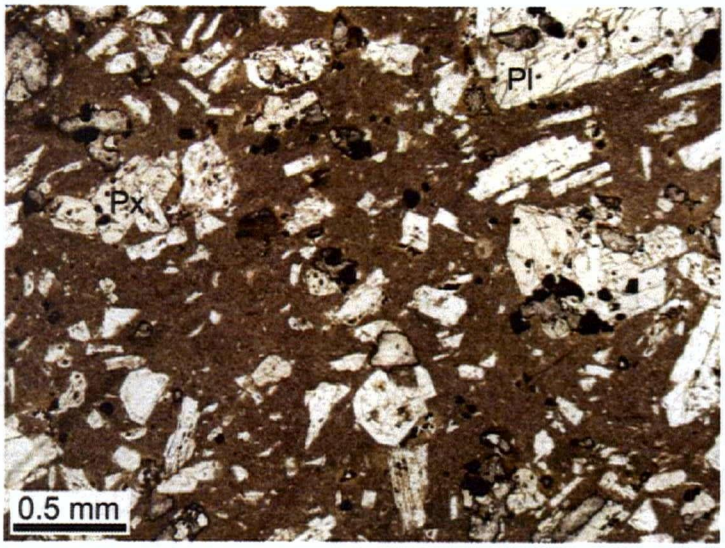

A) MR04-53. South El Dorado andesite lava flow. Px = pyroxene; Pl = plagioclase. Plane-polarized light.

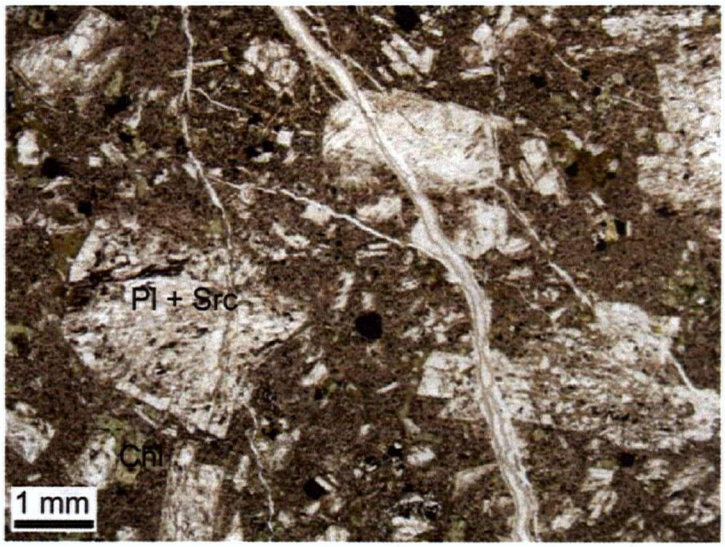

B) MR04-92. North El Dorado andesite lava flow (drill hole). Plagioclase (Pl) alters to sericite (Src). Plane-

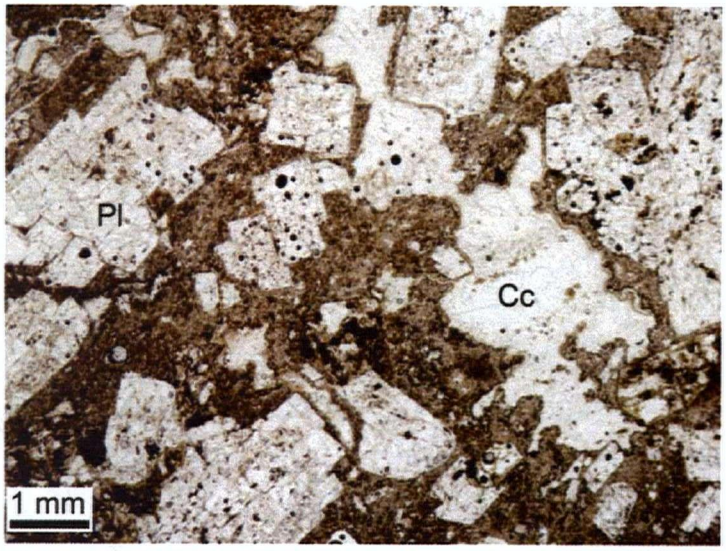

C) MR04-03. Central El Dorado andesite porphyry dome (drill hole). Cc = calcite. Plane-polarized light.

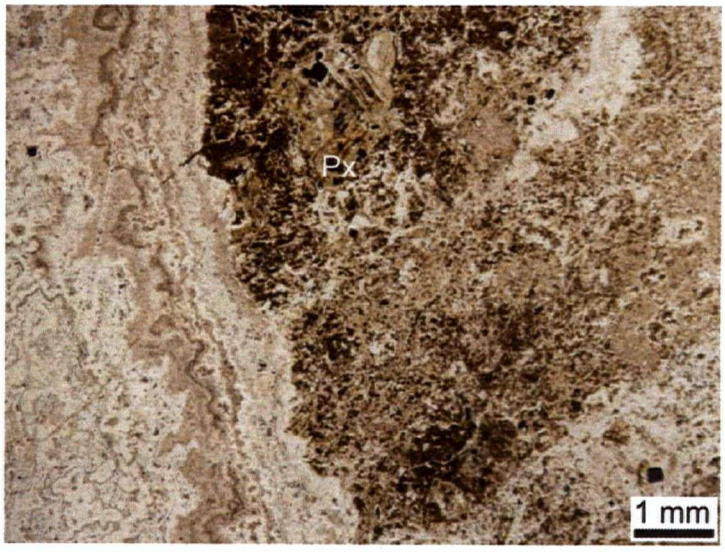

D) MR04-95. Central El Dorado silicified andesite lava flow. Plane-polarized light.

Figure B.1. Photomicrograhps of the El Dorado volcanic rocks under plane-polarized light.

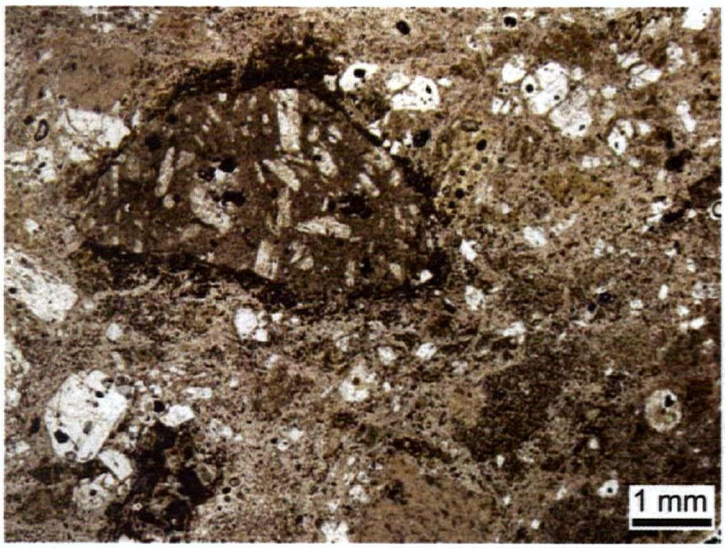

E) MR04-96. Plan de Minas epiclastic rock (drill hole). Plane-polarized light.

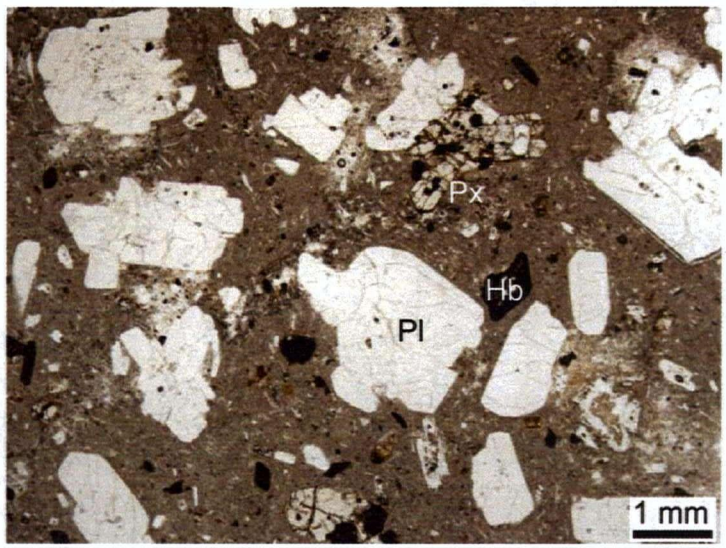

F) MR04-42. Cerro Caballo dome rock. Plane-polarized light.

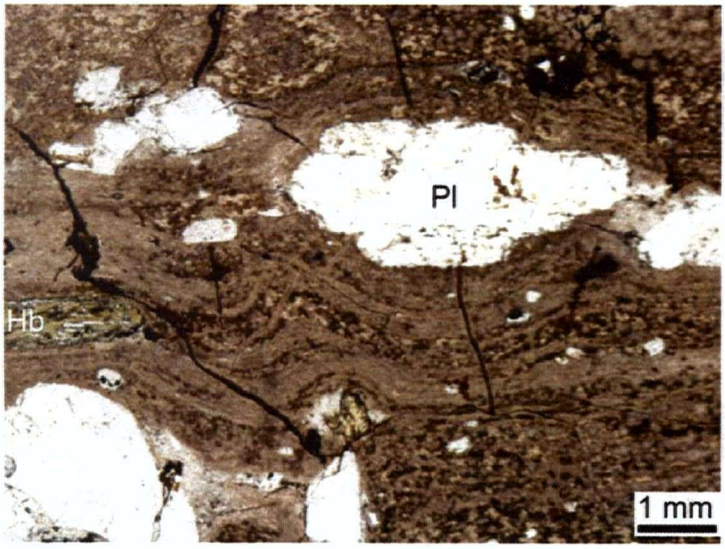

G) MR04-75. Cerro Caballo lava flow facies. Plane-polarized

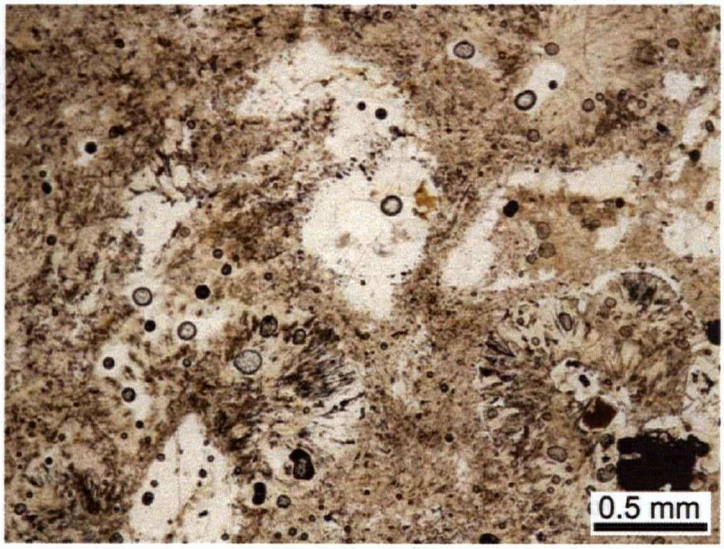

H) MR04-79. Plan de Minas spherulitic dacite lava flow. Plane-polarized light.

Figure B.1. Cont'd.

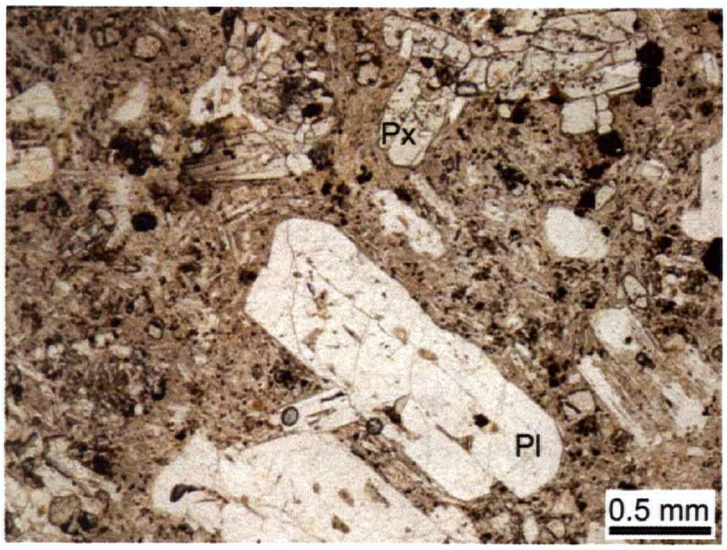

I) MR04-19. Cerro La Tablita platy andesite. Plane-polarized light.

J) LC-19. San Matias rhyolite dike. Plane-polarized light.

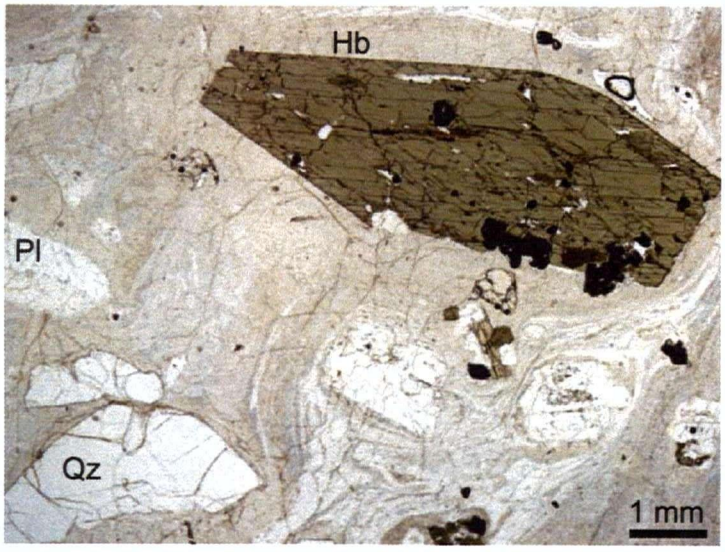

K) MR04-50. Cerro La Tabla rhyolite lava flow. Plane-polarized light.

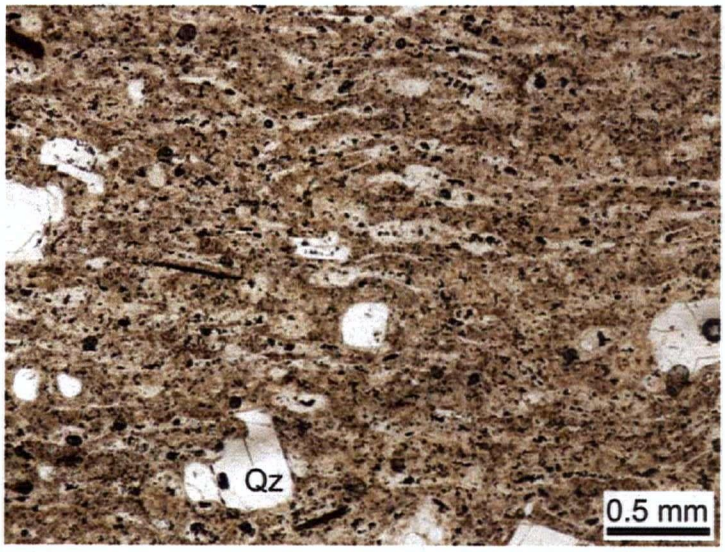

L) MR04-58. Cerro Alto summit rhyolite tuff. Plane-polarized light.

Figure B.1. Cont'd.

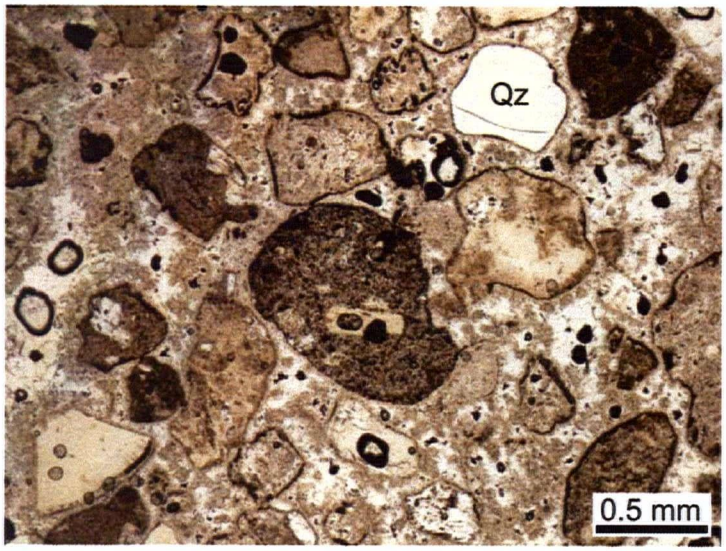

M) MR04-60. South El Dorado hydrothermal breccia. Plane-polarized light.

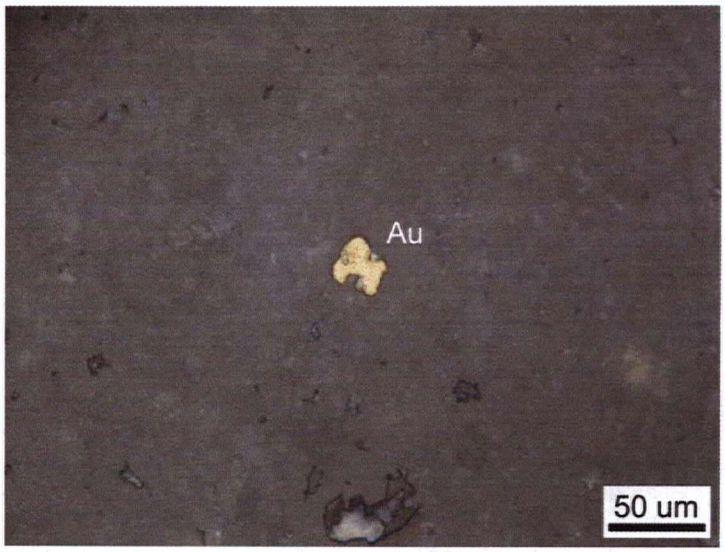

N) MR04-97. South El Dorado Nance Dulce vein. Gold grain in reflected light.

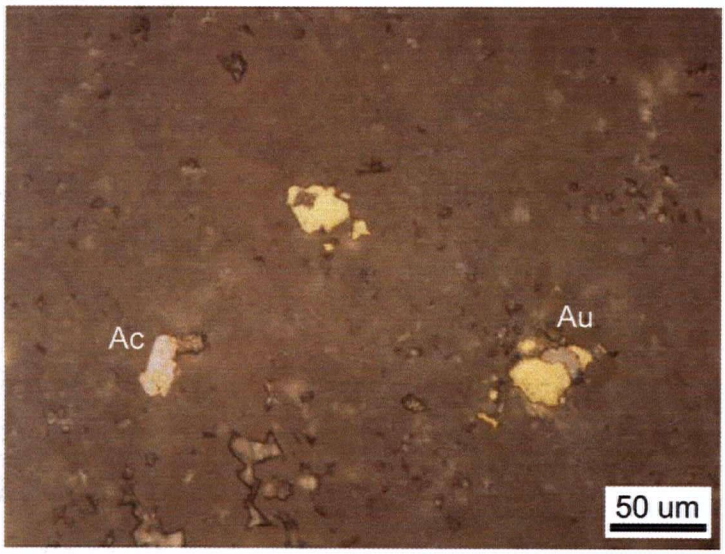

O) MR04-97. South El Dorado Nance Dulce vein. Gold (Au) and acanthite (Ac) in fine-grained adularia/quartz band. Reflected light.

Figure B.1. Cont'd.

APPENDIX C

WHOLE ROCK GEOCHEMICAL ANALYSES

METHOD SAMPLE	Rock Unit	Surface/ Drill hole #	Easting/ From	Northing/ To	ME-XRF06 SiO2 (wt%)	ME-XRF06 Al2O3	ME-XRF06 Fe2O3	ME-XRF06 CaO	ME-XRF06 MgO	ME-XRF06 Na2O
MR04-01	Tr	P03-272	457.23	457.50	70.52	13.46	1.71	1.94	0.37	3.9
MR04-02	Tap	P04-296	167.10	167.39	64.75	14.45	4.67	3.23	1.48	3.66
MR04-03	Tap	P04-273	221.85	222.95	53.12	18.18	7.19	6.42	2.81	3.93
MR04-06	Tap	P04-295	40.25	40.73	55.8	18.37	6.92	5.73	1.64	4.04
MR04-08	Tma	P04-295	309.10	309.90	50.15	18.38	9.14	7.51	3.66	3.29
M08	Tma	P04-295	309.10	309.90	50.44	18.66	8.59	7.31	3.76	3.41
MR04-09	Tap	P04-295	325.74	326.60	50.55	17.92	7.52	6.93	3.02	2.64
MR04-10	Tap	P04-298	328.33	328.86	57.41	16.3	6.48	3.9	1.61	4.02
M10	Tap	P04-298	328.33	328.86	56.76	16.1	6.05	3.95	1.95	2.45
MR04-15	Tr	surface	533962	296917	68.88	14.54	2.91	0.15	0.08	0.43
MR04-16	Tr	surface	533648	297165	72.37	12.36	1.53	0.82	0.51	2.01
MR04-19	Ta	surface	533611	297694	57.45	16.7	6.92	6.11	2.84	3.59
MR04-21	Tap	surface	534161	297458	60.28	17.24	5.54	4.2	0.89	3.39
MR04-24	Tr	surface	533430	301230	66.07	16.64	3.28	2.87	0.51	4.06
MR04-31	Tr	surface	534660	298555	70.15	15.01	2.27	2.14	0.15	4.15
MR04-34	Tr	surface	534990	299279	72.85	14.74	1.26	0.58	0.18	2.54
MR04-37	Tr	surface	534463	296385	68.45	14.3	3.38	2.61	0.64	3.24
MR04-40	Tr	surface	534801	296095	73.85	13.77	1.42	1.23	0.29	3.76
MR04-42	Tdd	surface	533326	299391	64.25	16.93	4.93	4.2	1.29	3.97
MR04-42a	Tdd	surface	533326	299391	64.04	17.07	5	4.16	1.35	4.16
MR04-42b	Tdd	surface	533326	299391	64.07	17.01	4.95	4.07	1.34	4.14
MR04-42c	Tdd	surface	533326	299391	64.3	16.98	4.89	4.1	1.32	4.13
MR04-50	Tr	surface	534986	303001	71.48	13.87	1.82	1.87	0.39	3.53
MR04-50a	Tr	surface	534986	303001	71.79	13.95	1.85	1.86	0.46	3.66
MR04-50b	Tr	surface	534986	303001	71.48	13.95	1.89	1.88	0.46	3.62
MR04-53	Tma	surface	535627	298277	55.3	18.01	7.63	7.03	3.22	3.48
MR04-58	Tr	surface	535626	297698	75.9	13.1	0.78	1.05	0.05	3.75
MR04-61	Tap	surface	536187	297731	50.25	20.5	8.18	9.01	2.69	3.37
MR04-62	Tma	surface	536430	296992	52.06	18.78	9.3	8.13	4.1	3.27
MR04-63	Tap	surface	536498	297047	47.71	18.17	8.71	7.79	4.14	2.67
MR04-64	Tma	surface	533875	304620	64.21	15.46	4.85	3.4	1.5	4.46
MR04-70	Tma	surface	531841	297799	54.75	17	5.93	4.88	2.62	2.17
M70	Tma	surface	531841	297799	57	16.86	5.8	4.31	2.29	2.16
MR04-75	Tdf	surface	533373	297673	72.2	13.7	2.35	1.3	0.24	3.08
MR04-76	Tdd	P04-305	269.50	270.55	64.19	14.94	3.12	3.2	0.82	2.77
MR04-79	Tdf	surface	533045	297960	68.96	14.77	2.25	2.18	0.37	3.12
MR04-79a	Tdf	surface	533045	297960	70.29	14.36	2.23	1.97	0.43	2.8
MR04-79b	Tdf	surface	533045	297960	70.25	14.26	2.21	1.97	0.41	2.87
MR04-79c	Tdf	surface	533045	297960	70.56	14.25	2.25	1.97	0.42	2.82
MR04-83	Tb	surface	532623	298267	51.4	19.69	8.88	9.88	3.17	2.87
MR04-83a	Tb	surface	532623	298267	51	19.66	9.02	10.01	3.41	3.05
MR04-83b	Tb	surface	532623	298267	51.23	19.61	9.05	10.01	3.43	3.08
MR04-83c	Tb	surface	532623	298267	50.95	19.79	9.07	10.02	3.4	3.07
MR04-84	Tma	P04-280	296.68	297.07	51.75	17.55	7.83	4.78	3.33	2.79
MR04-85	Tma	P04-284	56.61	56.83	50.85	17.66	8.61	8.19	4.84	3.04
MR04-86	Tma	P04-284	53.45	53.75	56.24	13.16	6.22	5.27	3.27	0.64
MR04-87	Tdd	PLC03-11	275.19	277.17	63.79	15.65	3.39	3.81	1.17	2.91
M87	Tdd	PLC03-11	275.19	277.17	63.62	14.58	3.44	3.74	1.1	3.07
MR04-88	Tap	PLC03-27	137.20	138.30	55	16.1	5.57	6.62	1.52	2
MR04-89	Tr	P03-269	178.95	180.18	70.55	13.63	1.6	1.63	0.33	4.34
MR04-91	Tr	P03-269	317.00	317.60	72.88	12.41	1.53	0.27	0.24	0.46
MR04-92	Tma	P03-269	325.85	326.11	54.96	16.26	7.33	3.08	3.57	1.38
MR04-94	Tr	P04-303	60.90	61.50	68.25	14.35	2.66	0.97	0.6	1.56
MR04-98	Tap	P04-301	349.60	350.20	59.44	17.3	5.27	4.88	1.22	4.38
MR04-99	Tma	P04-307	390.70	391.15	55.6	15.91	7.95	5.47	2.42	2.88
MR04-101	Tb	surface	533671	302380	60.01	15.95	5.51	5.29	2.55	3.6
MM01	Tma	surface	534709	299924	52.45	17.55	9.3	8.15	4	3.05
MM01a	Tma	surface	534709	299924	51.68	18.7	9.72	8.55	4.3	3.25
MM01b	Tma	surface	534709	299924	51.59	18.65	9.76	8.51	4.3	3.26
MM13	Ta	surface	533625	300518	58.24	16.08	6.52	6.02	3.18	3.65
MM23	Ta	surface	533274	301383	58.75	17.05	6.62	6.11	2.99	3.71
MM29	Tdd	surface	533605	300339	62.55	17.66	5.15	3.87	1.7	4.09
LC-19	Tr	surface	532620	306210	68.95	15.85	1.73	1.23	0.2	4.36
BAS-1	std	MDRU lab	-	-	51.27	15.45	11.14	8.4	7.3	3.25
BAS-1a	std	MDRU lab	-	-	51.76	15.56	11.43	8.29	7.34	3.26
P-1	std	MDRU lab	-	-	68.01	15.57	3.97	3.7	1.1	4
P-1a	std	MDRU lab	-	-	69.77	14.82	3.87	3.4	1.04	3.84

ALS/Chemex analyses for major oxides (ME-XRF06) are given in wt (%) and trace elements (ME-MS81) in ppm.

Duplicate analyses are indicated by the letter a,b or c following the original sample number.

Samples M08, M10, M70 and M87 are field replicate analyses of samples MR04-08, MR04-10, MR04-70 and MR04-87 respectively.

Refer to chapters 2 and 3 for rock unit descriptions and symbol explaination.

METHOD SAMPLE	ME-XRF06 K2O	ME-XRF06 Cr2O3	ME-XRF06 TiO2	ME-XRF06 MnO	ME-XRF06 P2O5	ME-XRF06 SrO	ME-XRF06 BaO	ME-XRF06 LOI	ME-XRF06 Total	ME-MS81 Ag (ppm)
MR04-01	2.64	<0.01	0.22	0.06	0.04	0.03	0.12	3.56	98.57	<1
MR04-02	1.51	<0.01	0.66	0.12	0.24	0.04	0.05	4.35	99.22	<1
MR04-03	1.38	<0.01	0.77	0.17	0.19	0.06	0.06	5.6	99.88	4
MR04-06	0.95	<0.01	0.84	0.18	0.29	0.08	0.11	4.98	99.93	<1
MR04-08	1.11	<0.01	0.91	0.15	0.18	0.06	0.05	4.93	99.52	<1
M08	0.84	<0.01	0.93	0.15	0.17	0.08	0.04	4.29	98.69	<1
MR04-09	1.86	<0.01	0.86	0.17	0.25	0.04	0.06	6.85	98.65	<1
MR04-10	3.02	<0.01	0.78	0.12	0.29	0.02	0.06	4.72	98.72	<1
M10	5.3	0.01	0.84	0.13	0.31	0.04	0.16	4.51	98.56	<1
MR04-15	9.82	<0.01	0.6	0.03	0.06	0.02	0.11	1.49	99.11	1
MR04-16	4.58	<0.01	0.2	0.04	0.04	0.01	0.14	3.58	98.18	<1
MR04-19	1.65	<0.01	0.69	0.13	0.16	0.06	0.09	2.02	98.41	<1
MR04-21	2.37	<0.01	0.66	0.08	0.18	0.03	0.08	4.27	99.22	<1
MR04-24	2.74	<0.01	0.33	0.08	0.02	0.03	0.13	2.54	99.29	<1
MR04-31	2.9	<0.01	0.28	0.03	0.04	0.02	0.13	1.57	98.85	<1
MR04-34	3.64	<0.01	0.19	0.03	0.01	<0.01	0.13	3.39	99.55	<1
MR04-37	2.67	<0.01	0.36	0.05	0.09	0.03	0.12	2.65	98.58	<1
MR04-40	3.8	<0.01	0.18	0.04	0.05	0.02	0.15	1.09	99.64	<1
MR04-42	2.07	0.01	0.52	0.09	0.14	0.05	0.1	1.31	99.87	<1
MR04-42a	2.19	<0.01	0.47	0.09	0.13	0.04	0.11	1	99.81	<1
MR04-42b	2.26	<0.01	0.5	0.09	0.13	0.05	0.11	0.99	99.7	<1
MR04-42c	2.21	<0.01	0.49	0.08	0.13	0.05	0.11	0.99	99.78	<1
MR04-50	3.08	<0.01	0.23	0.07	0.05	0.03	0.13	2.8	99.34	<1
MR04-50a	3.2	0.01	0.18	0.07	0.05	0.03	0.14	2.75	99.99	<1
MR04-50b	3.25	<0.01	0.17	0.07	0.05	0.03	0.15	2.75	99.74	<1
MR04-53	1.5	<0.01	0.87	0.13	0.24	0.05	0.06	2.23	99.74	<1
MR04-58	3.59	<0.01	0.19	<0.01	0.03	0.02	0.14	1.17	99.77	<1
MR04-61	1.03	<0.01	0.93	0.16	0.19	0.07	0.05	3	99.43	<1
MR04-62	1	0.03	0.99	0.15	0.22	0.06	0.05	1.63	99.78	<1
MR04-63	0.92	<0.01	0.86	0.14	0.19	0.05	0.06	7.63	99.03	<1
MR04-64	1.9	<0.01	0.69	0.1	0.26	0.04	0.09	2.82	99.77	<1
MR04-70	4.71	<0.01	0.63	0.15	0.14	0.04	0.09	6.16	99.27	<1
M70	4.62	<0.01	0.64	0.14	0.15	0.03	0.1	5.81	99.91	<1
MR04-75	3.29	<0.01	0.27	0.02	0.05	0.02	0.13	2.29	98.94	<1
MR04-76	2.82	<0.01	0.43	0.09	0.13	0.05	0.11	5.96	98.63	<1
MR04-79	3.55	<0.01	0.27	0.06	0.08	0.05	0.17	3.85	99.67	<1
MR04-79a	3.63	<0.01	0.23	0.06	0.08	0.05	0.18	3.35	99.66	<1
MR04-79b	3.61	<0.01	0.23	0.06	0.08	0.05	0.18	3.35	99.53	<1
MR04-79c	3.66	<0.01	0.24	0.06	0.08	0.05	0.18	3.32	99.86	<1
MR04-83	0.94	<0.01	0.91	0.17	0.2	0.08	0.05	1.22	99.47	<1
MR04-83a	1.01	<0.01	0.96	0.19	0.18	0.07	0.07	1.06	99.69	<1
MR04-83b	1.01	0.01	0.98	0.19	0.18	0.07	0.07	1.05	99.96	<1
MR04-83c	0.98	<0.01	0.95	0.18	0.18	0.07	0.06	1.04	99.77	<1
MR04-84	3.43	<0.01	0.84	0.13	0.2	0.03	0.04	7.07	99.77	<1
MR04-85	1.11	0.01	0.89	0.14	0.28	0.07	0.06	2.94	98.69	<1
MR04-86	6.5	<0.01	0.7	0.15	0.21	0.03	0.05	6.54	98.98	<1
MR04-87	3.36	<0.01	0.39	0.09	0.1	0.03	0.13	5.06	99.87	<1
M87	2.99	<0.01	0.4	0.08	0.12	0.04	0.09	5.26	98.52	<1
MR04-88	2.81	<0.01	0.64	0.16	0.17	0.04	0.07	9.08	99.78	<1
MR04-89	3.33	0.04	0.26	0.08	0.05	0.04	0.11	2.39	98.38	<1
MR04-91	9.46	<0.01	0.24	0.06	0.04	0.01	0.11	0.84	98.55	<1
MR04-92	7.27	<0.01	0.8	0.19	0.2	0.03	0.07	3.4	98.53	1
MR04-94	5.61	<0.01	0.33	0.09	0.09	0.02	0.11	3.93	98.57	<1
MR04-98	2.18	<0.01	0.65	0.07	0.18	0.04	0.08	2.67	98.37	<1
MR04-99	2.51	<0.01	0.82	0.11	0.23	0.05	0.09	5.15	99.19	<1
MR04-101	1.69	<0.01	0.58	0.1	0.16	0.06	0.08	2.79	98.38	<1
MM01	0.86	<0.01	0.91	0.15	0.17	0.06	0.06	1.5	98.2	<1
MM01a	0.81	<0.01	1.09	0.17	0.17	0.06	0.05	1.2	99.76	<1
MM01b	0.81	<0.01	1.1	0.17	0.17	0.05	0.05	1.21	99.65	<1
MM13	1.54	0.01	0.64	0.11	0.17	0.06	0.08	1.93	98.22	<1
MM23	1.58	0.01	0.64	0.12	0.18	0.05	0.08	1.75	99.64	<1
MM29	1.85	<0.01	0.5	0.1	0.1	0.05	0.11	1.75	99.48	<1
LC-19	3.76	<0.01	0.3	0.07	0.04	0.03	0.13	1.79	98.44	<1
BAS-1	0.56	0.02	1.3	0.14	0.27	0.06	0.02	-0.07	99.11	<1
BAS-1a	0.54	0.03	1.41	0.15	0.21	0.05	0.03	-0.11	99.94	<1
P-1	2.1	0.01	0.4	0.07	0.07	0.02	0.08	0.48	99.58	<1
P-1a	2.07	0.02	0.4	0.07	0.08	0.03	0.08	0.45	99.94	<1

METHOD	ME-MS81	ME-MS81	ME-MS81	ME-MS81	ME-MS81	ME-MS81	ME-MS81	ME-MS81	ME-MS81	ME-MS81
SAMPLE	Ba	Ce	Co	Cr	Cs	Cu	Dy	Er	Eu	Ga
MR04-01	1220	22.9	2.9	30	4.7	5	1.2	0.8	0.4	14
MR04-02	416	32.1	7.9	30	1.5	22	5.8	3.7	1.2	17
MR04-03	526	22.7	20	20	2.8	42	3.5	2.2	1.1	20
MR04-06	1145	26.6	16	10	1.9	64	4.4	2.6	1.3	21
MR04-08	372	15.8	32.6	50	1.7	88	3.2	2	1	19
M08	346	16.6	32.5	60	1.2	104	3.3	1.9	1	20
MR04-09	480	20.4	19.6	20	8.7	77	3.7	2.1	1.1	20
MR04-10	552	37.9	12.6	10	3.3	52	5.1	3.2	1.3	20
M10	1600	36.9	13.2	10	3.3	55	5.7	3.5	1.3	17
MR04-15	954	46.4	5	30	2.7	9	9.3	5.2	2.4	12
MR04-16	1345	29.6	2.5	20	1.2	5	1.4	1	0.4	12
MR04-19	859	22.2	21.5	60	0.3	47	4.5	2.8	1.3	18
MR04-21	783	26.5	11.9	20	1.8	8	3.6	2.4	0.9	15
MR04-24	1150	22.9	5.8	30	2.4	9	1.4	0.9	0.6	14
MR04-31	1230	29	3.4	20	1.9	6	3.1	1.7	0.9	14
MR04-34	1225	17	1.4	20	2.5	<5	0.9	0.7	0.2	13
MR04-37	1220	27.5	5.6	30	1.3	13	2.3	1.4	0.8	15
MR04-40	1520	28.8	2.2	40	2.1	<5	1.4	1.1	0.4	13
MR04-42	970	24.4	12.7	30	0.5	24	2.7	1.7	0.8	17
MR04-42a	945	23.1	10.4	30	0.8	25	2.7	1.7	0.8	16
MR04-42b	939	22.8	10.2	30	0.8	25	2.7	1.8	0.7	17
MR04-42c	971	23.7	10	30	0.8	25	2.7	1.8	0.8	17
MR04-50	1170	22.4	2.9	30	2.9	<5	1.2	0.9	0.4	12
MR04-50a	1240	22.9	2.8	30	3.4	5	1.4	1	0.4	13
MR04-50b	1175	21.6	2.5	30	3.2	5	1.3	0.9	0.5	12
MR04-53	594	25.1	23.1	30	0.7	62	3.8	2.3	1.1	18
MR04-58	1375	27	1.2	20	1.5	<5	1.3	0.9	0.5	12
MR04-61	485	19	22.5	20	<0.1	47	3.7	2	1	21
MR04-62	480	21.7	26.7	30	0.4	62	3.5	2.1	1.1	19
MR04-63	481	18.9	25.3	30	0.2	70	3.1	1.9	1	19
MR04-64	801	30.5	6.4	20	0.4	19	5	3.2	1.5	18
MR04-70	845	26.5	13	40	3.2	37	2.6	1.7	0.8	17
M70	843	26.2	14	40	3.2	39	2.9	1.9	0.9	17
MR04-75	1185	27.1	3.5	50	3.5	9	1.9	1	0.9	12
MR04-76	978	24.7	6.5	20	5.7	23	2.1	1.5	0.7	16
MR04-79	1540	23.5	4.7	30	4.5	12	1.6	1.2	0.6	14
MR04-79a	1595	22.3	4.4	30	4.5	13	1.9	1.2	0.6	13
MR04-79b	1585	22.1	4.3	30	4.5	13	1.8	1.1	0.6	13
MR04-79c	1580	22.1	4.3	30	4.4	14	1.8	1.1	0.6	13
MR04-83	539	18.8	25.3	30	0.7	109	3.3	1.9	1	20
MR04-83a	541	17.5	23.3	30	0.7	110	3.4	2	1.1	21
MR04-83b	578	18.6	24	30	0.7	114	3.6	2.1	1.1	22
MR04-83c	542	17.4	22.8	30	0.7	110	3.4	2	1	21
MR04-84	333	18.6	21.5	30	6.9	106	2.9	1.6	1	17
MR04-85	473	24.2	26.1	90	0.2	75	3.4	2.1	1.2	19
MR04-86	391	17.1	19.5	70	8	43	2.6	1.5	0.9	12
MR04-87	1230	24.8	7.2	10	6.9	13	1.9	1.3	0.7	14
M87	927	24.3	7.9	30	7.3	17	2	1.3	0.6	15
MR04-88	567	26.7	16.6	20	14.9	35	3.3	2	1	18
MR04-89	1110	35.5	1.3	10	2.6	<5	2.8	1.9	0.8	15
MR04-91	1090	33.3	1.3	60	4.5	6	2.5	1.6	0.6	13
MR04-92	525	23	20.4	40	3.2	60	3.4	2.1	1.1	19
MR04-94	1075	23.5	4.8	30	6.1	8	1.5	1	0.6	15
MR04-98	778	29.2	11.4	20	1.7	19	4.2	2.6	1.1	18
MR04-99	874	25	21	30	4	40	3.6	2.2	1	17
MR04-101	809	27.6	15.4	60	0.7	34	3.1	1.9	1	18
MM01	489	19.4	27.3	50	0.1	75	3.4	2	1.1	20
MM01a	475	17.8	24.3	40	0.1	76	3.7	2.2	1.1	20
MM01b	481	18.4	24.5	50	0.1	79	3.7	2.2	1.1	20
MM13	783	24.4	19.9	110	0.5	30	2.9	1.8	0.9	18
MM23	751	22.4	18.4	110	0.7	41	3	1.9	1	18
MM29	1080	26.7	13	40	0.4	28	2.7	1.6	0.9	19
LC-19	1290	44.1	1.9	20	2.1	<5	3.3	2.2	1	16
BAS-1	175.5	19.4	45.2	230	0.1	56	3.1	1.5	1.3	19
BAS-1a	183	18.6	41.9	230	0.1	56	3.2	1.6	1.1	19
P-1	768	25.4	7.2	150	1	9	3.1	1.8	0.7	15
P-1a	771	22.9	6.5	160	1	8	3.2	2.2	0.8	15

METHOD	ME-MS81	ME-MS81	ME-MS81	ME-MS81	ME-MS81	ME-MS81	ME-MS81	ME-MS81	ME-MS81	ME-MS81
SAMPLE	Gd	Hf	Ho	La	Lu	Mo	Nb	Nd	Ni	Pb
MR04-01	1.3	3	0.3	14	0.2	3	4	8.7	<5	8
MR04-02	5.5	6	1.2	14.6	0.6	<2	5	21.4	<5	9
MR04-03	3.6	4	0.7	10.3	0.4	<2	3	14	7	6
MR04-06	4.4	4	0.9	12.1	0.4	<2	4	18.2	7	5
MR04-08	3.2	3	0.7	6.9	0.3	<2	2	10.8	29	<5
M08	3.3	2	0.7	7.3	0.3	<2	2	11.4	27	<5
MR04-09	3.5	3	0.7	9.4	0.3	<2	3	14.2	10	<5
MR04-10	5	6	1.2	16.8	0.5	<2	5	24.1	5	8
M10	5.8	6	1.2	16	0.5	<2	5	23.3	6	7
MR04-15	10	4	2	24.5	0.8	<2	4	33.3	6	7
MR04-16	1.7	4	0.3	18	0.2	2	5	11.7	<5	11
MR04-19	4.6	4	0.9	13.8	0.4	2	3	16.4	19	7
MR04-21	3.8	5	0.8	12.6	0.4	<2	4	16	5	5
MR04-24	1.5	4	0.3	11.4	0.2	3	4	8	<5	9
MR04-31	3.7	4	0.6	34.4	0.3	2	4	22.6	<5	9
MR04-34	0.9	3	0.2	11.5	0.2	2	5	6.4	<5	10
MR04-37	2.8	3	0.5	21.2	0.2	2	4	17.6	7	8
MR04-40	1.6	4	0.3	17.1	0.2	2	5	10.4	<5	9
MR04-42	2.7	5	0.5	13.4	0.3	2	4	12.7	11	8
MR04-42a	2.9	4	0.5	12.4	0.3	<2	4	13.8	11	7
MR04-42b	2.9	4	0.5	12.1	0.3	2	4	13.6	13	7
MR04-42c	2.9	5	0.5	12.6	0.3	<2	4	14.2	12	7
MR04-50	1.5	3	0.2	13.2	0.2	3	3	8.1	<5	8
MR04-50a	1.7	3	0.3	13.2	0.2	3	4	10.2	5	8
MR04-50b	1.7	3	0.3	12.6	0.2	3	4	9.6	<5	8
MR04-53	3.8	4	0.8	11.8	0.4	<2	3	15.8	11	6
MR04-58	1.7	3	0.3	19.4	0.2	<2	4	12	<5	11
MR04-61	3.6	3	0.7	8.8	0.3	<2	2	13	8	<5
MR04-62	3.8	3	0.7	9.6	0.3	2	3	14.6	16	5
MR04-63	3.5	3	0.6	8.3	0.3	<2	2	12.6	16	<5
MR04-64	5.4	5	1.1	13.4	0.5	<2	4	20.1	<5	8
MR04-70	2.8	4	0.6	13	0.3	<2	4	14.1	14	6
M70	3.1	4	0.6	12.7	0.3	<2	4	13.7	11	6
MR04-75	2.9	3	0.3	19.2	0.2	<2	4	17.4	6	9
MR04-76	2.3	5	0.5	12.6	0.2	<2	4	11.8	6	10
MR04-79	2.1	3	0.4	14.6	0.2	<2	4	10.6	<5	8
MR04-79a	2.2	3	0.3	14.2	0.2	<2	4	11.8	<5	8
MR04-79b	2.2	3	0.3	14	0.2	2	4	11.6	5	7
MR04-79c	2.3	3	0.3	14	0.2	2	4	11.7	5	8
MR04-83	3.1	2	0.6	8.8	0.3	<2	2	12.4	10	5
MR04-83a	3.5	2	0.6	8.3	0.3	<2	2	13.2	10	5
MR04-83b	3.7	3	0.7	8.8	0.3	<2	2	14.2	12	5
MR04-83c	3.4	2	0.6	8.4	0.3	2	2	13.6	11	5
MR04-84	3.3	2	0.6	8.5	0.2	<2	2	12.2	13	<5
MR04-85	3.9	4	0.7	10.7	0.3	<2	4	15.3	40	5
MR04-86	3	2	0.5	7.7	0.2	<2	3	11.4	28	<5
MR04-87	2.2	4	0.4	13	0.2	<2	4	10.8	<5	8
M87	2.2	4	0.4	12.5	0.2	<2	4	10.8	5	8
MR04-88	3.4	5	0.7	12.6	0.3	2	4	14.6	11	6
MR04-89	3.1	6	0.6	17.8	0.3	<2	5	16.2	6	11
MR04-91	2.7	6	0.5	16.2	0.3	2	5	14.8	6	10
MR04-92	3.8	4	0.7	10.2	0.3	<2	3	14.2	20	5
MR04-94	1.7	3	0.3	13	0.2	<2	4	9.5	7	7
MR04-98	4.4	6	0.8	13.6	0.4	<2	5	17.2	6	7
MR04-99	3.9	4	0.8	11.5	0.3	<2	4	16	13	<5
MR04-101	3.3	4	0.7	12	0.3	<2	3	13	20	6
MM01	3.6	3	0.7	8.5	0.3	2	3	12.6	13	<5
MM01a	3.5	3	0.7	8.1	0.3	<2	2	13.6	9	<5
MM01b	3.8	3	0.7	8.6	0.3	<2	3	13.9	9	<5
MM13	3.1	4	0.6	11.8	0.3	3	3	13.1	30	7
MM23	3.4	4	0.6	11.7	0.3	<2	3	14	23	31
MM29	2.8	5	0.5	13.8	0.3	<2	4	13	11	8
LC-19	3.9	7	0.7	24.7	0.4	<2	6	21.4	<5	11
BAS-1	3.4	3	0.6	9.2	0.2	2	7	12	172	<5
BAS-1a	3.5	3	0.5	8.9	0.2	3	7	13.4	180	<5
P-1	2.8	4	0.6	13.2	0.3	<2	3	12.6	9	8
P-1a	2.9	4	0.6	12	0.3	<2	3	12.6	7	9

METHOD	ME-MS81	ME-MS81	ME-MS81	ME-MS81	ME-MS81	ME-MS81	ME-MS81	ME-MS81	ME-MS81	ME-MS81
SAMPLE	Pr	Rb	Sm	Sn	Sr	Ta	Tb	Th	Tl	Tm
MR04-01	2.6	67.8	1.6	1	287	<0.5	0.2	6	<0.5	0.2
MR04-02	4.8	28.8	5.3	2	287	<0.5	1	2	<0.5	0.6
MR04-03	3.1	30.1	3.6	1	518	<0.5	0.6	1	<0.5	0.3
MR04-06	4	19.6	4.7	1	705	<0.5	0.7	1	<0.5	0.4
MR04-08	2.3	35.3	2.9	1	564	<0.5	0.5	1	<0.5	0.3
M08	2.4	26.6	3.1	1	579	<0.5	0.5	1	<0.5	0.3
MR04-09	3.1	67.8	3.6	1	438	<0.5	0.6	1	<0.5	0.3
MR04-10	5.4	103.5	5.9	4	229	0.5	0.9	2	<0.5	0.5
M10	5.2	149.5	5.8	1	328	<0.5	1	2	0.6	0.5
MR04-15	7.6	381	8.5	1	202	<0.5	1.6	2	1.8	0.8
MR04-16	3.5	104.5	1.9	1	115.5	0.5	0.3	7	<0.5	0.2
MR04-19	3.6	29.5	3.7	1	438	<0.5	0.7	2	<0.5	0.4
MR04-21	3.7	50.6	3.8	1	334	<0.5	0.6	2	<0.5	0.4
MR04-24	2.3	60.3	1.5	1	274	<0.5	0.2	5	<0.5	0.2
MR04-31	6.4	67.5	3.8	1	251	<0.5	0.6	5	<0.5	0.3
MR04-34	2	83.8	1	1	70.1	0.5	0.2	8	<0.5	0.1
MR04-37	4.7	64.6	3.2	1	317	<0.5	0.4	4	<0.5	0.2
MR04-40	3.2	94.6	1.9	1	143	0.6	0.3	8	<0.5	0.2
MR04-42	3.3	46.1	2.8	1	392	<0.5	0.5	4	<0.5	0.3
MR04-42a	3	42.6	2.8	1	405	<0.5	0.4	3	<0.5	0.2
MR04-42b	3	42.7	2.8	1	410	<0.5	0.4	3	<0.5	0.2
MR04-42c	3.1	42.9	3	1	407	<0.5	0.4	3	<0.5	0.2
MR04-50	2.5	64	1.4	1	202	<0.5	0.2	6	<0.5	0.1
MR04-50a	2.6	66.5	1.8	1	216	<0.5	0.2	6	<0.5	0.1
MR04-50b	2.4	62.8	1.6	1	203	<0.5	0.2	5	<0.5	0.1
MR04-53	3.6	24.7	3.6	2	463	<0.5	0.6	2	<0.5	0.4
MR04-58	3.8	82.1	1.9	1	127	0.5	0.3	8	<0.5	0.2
MR04-61	2.8	17.6	3.6	1	575	<0.5	0.6	1	<0.5	0.3
MR04-62	3.2	16.1	3.7	1	507	<0.5	0.6	1	<0.5	0.3
MR04-63	2.8	14	3.3	1	485	<0.5	0.5	1	<0.5	0.2
MR04-64	4.6	30.5	5.2	2	311	<0.5	0.9	2	<0.5	0.5
MR04-70	3.5	163	3.2	2	331	<0.5	0.5	3	0.5	0.3
M70	3.3	161	3	1	303	<0.5	0.5	3	0.6	0.3
MR04-75	5.1	112	3.4	1	188.5	<0.5	0.4	3	<0.5	0.1
MR04-76	3.1	88.8	2.4	1	271	<0.5	0.4	4	<0.5	0.2
MR04-79	3	106.5	2	1	392	<0.5	0.3	4	<0.5	0.1
MR04-79a	2.8	107	2.1	1	439	<0.5	0.3	3	<0.5	0.2
MR04-79b	2.8	105.5	2.1	1	437	<0.5	0.3	4	<0.5	0.2
MR04-79c	2.8	105	2.1	1	436	<0.5	0.3	3	<0.5	0.1
MR04-83	2.8	21.7	3.3	1	605	<0.5	0.5	2	<0.5	0.3
MR04-83a	2.5	21.4	3.3	1	658	<0.5	0.5	2	<0.5	0.3
MR04-83b	2.7	22.2	3.6	1	673	<0.5	0.5	2	<0.5	0.3
MR04-83c	2.6	21.2	3.3	1	647	<0.5	0.5	2	<0.5	0.3
MR04-84	2.8	163.5	3.2	1	281	<0.5	0.5	1	<0.5	0.2
MR04-85	3.5	14.4	3.9	1	519	<0.5	0.6	1	<0.5	0.3
MR04-86	2.5	284	2.8	1	262	<0.5	0.4	1	0.8	0.2
MR04-87	2.9	99.1	2.2	1	296	<0.5	0.3	4	<0.5	0.2
M87	2.8	93.4	2.2	1	302	<0.5	0.3	4	<0.5	0.2
MR04-88	3.7	93.7	3.5	1	330	<0.5	0.5	2	<0.5	0.3
MR04-89	4.5	99.7	3.3	1	311	<0.5	0.5	5	<0.5	0.3
MR04-91	4.1	419	3	1	106	<0.5	0.4	4	1.3	0.2
MR04-92	3.4	236	3.7	1	262	<0.5	0.6	1	0.7	0.3
MR04-94	2.8	199	1.8	1	145	<0.5	0.3	4	<0.5	0.1
MR04-98	4.2	46.8	4.1	1	420	<0.5	0.7	2	<0.5	0.3
MR04-99	3.7	60.9	4.1	1	499	<0.5	0.6	1	<0.5	0.3
MR04-101	3.2	30.4	2.9	1	427	<0.5	0.5	2	<0.5	0.3
MM01	2.9	7.4	3.3	1	509	<0.5	0.6	1	<0.5	0.3
MM01a	2.6	6.9	3.5	1	525	<0.5	0.6	1	<0.5	0.3
MM01b	2.6	7.1	3.5	1	534	<0.5	0.6	1	<0.5	0.3
MM13	3.3	27	3.2	1	470	<0.5	0.5	2	<0.5	0.3
MM23	3.3	27.4	3.2	1	463	<0.5	0.5	2	<0.5	0.3
MM29	3.5	25	3	1	386	<0.5	0.4	3	<0.5	0.2
LC-19	6.1	92.8	4	1	185	0.5	0.6	5	<0.5	0.3
BAS-1	2.9	6.1	3.2	1	467	0.5	0.5	1	<0.5	0.2
BAS-1a	2.6	5.8	3.4	1	491	<0.5	0.5	1	<0.5	0.2
P-1	3.2	44.9	2.5	2	217	<0.5	0.4	4	<0.5	0.3
P-1a	2.7	43.2	2.8	2	212	<0.5	0.5	4	<0.5	0.3

METHOD	ME-MS81	ME-MS81	ME-MS81	ME-MS81	ME-MS81	ME-MS81	ME-MS81
SAMPLE	U	V	W	Y	Yb	Zn	Zr
MR04-01	2.4	23	2	8.6	1.1	32	96
MR04-02	1.1	47	4	34.6	3.5	77	187.5
MR04-03	0.6	194	1	22.4	2.1	82	114
MR04-06	0.5	122	2	27.4	2.5	90	119.5
MR04-08	<0.5	263	7	18.4	1.8	86	82.5
M08	<0.5	262	1	18.9	1.8	89	68.7
MR04-09	<0.5	243	2	22	1.9	83	86.2
MR04-10	1	104	34	32.4	3.4	78	181.5
M10	1.1	108	1	33.9	3.3	88	184.5
MR04-15	0.9	70	2	64.3	4.7	34	266
MR04-16	2.5	19	2	10.6	1.1	28	105
MR04-19	1	175	1	33	2.5	67	132.5
MR04-21	0.9	102	3	21.9	2.3	57	154
MR04-24	2	51	2	9	1.2	44	131
MR04-31	2.1	30	2	19.3	1.7	32	104.5
MR04-34	2.7	13	2	6.7	0.9	21	87.5
MR04-37	1.7	58	3	16	1.4	42	110.5
MR04-40	3.3	15	4	11.4	1.3	26	161
MR04-42	1.4	96	3	17.2	1.8	64	153
MR04-42a	1.2	106	2	16.3	1.9	75	134.5
MR04-42b	1.2	106	2	16.7	2	72	139
MR04-42c	1.2	106	1	16.5	1.9	76	144
MR04-50	2.2	22	3	8.2	1	30	77.8
MR04-50a	2.2	29	2	9.2	1.2	45	85.8
MR04-50b	2.1	28	2	8.8	1.2	43	76.2
MR04-53	0.7	201	1	23	2.3	79	144
MR04-58	3	12	2	9	1.1	21	80.3
MR04-61	0.5	240	1	21.2	1.8	83	90.6
MR04-62	0.5	253	2	21.2	2	83	103.5
MR04-63	0.5	249	2	19	1.7	99	81.1
MR04-64	0.8	52	1	30.9	3.1	90	161.5
MR04-70	1	108	2	17.1	1.8	57	129.5
M70	1	112	10	18.3	1.8	65	136
MR04-75	1.6	32	2	9.6	1.1	43	86.5
MR04-76	1.5	67	2	13.2	1.6	51	140.5
MR04-79	1.6	34	3	13.5	1.1	40	85.4
MR04-79a	1.4	45	2	13.2	1.2	44	84
MR04-79b	1.5	47	1	13	1.2	41	83.2
MR04-79c	1.4	48	2	13.4	1.1	44	95.8
MR04-83	0.7	309	2	18.9	1.8	87	68
MR04-83a	0.7	333	1	18	1.9	96	59.6
MR04-83b	0.7	347	2	18.8	2	99	71.2
MR04-83c	0.7	334	1	18.2	1.9	94	60.3
MR04-84	<0.5	239	3	16.4	1.5	70	70.4
MR04-85	<0.5	219	3	21.3	2.1	84	126
MR04-86	<0.5	144	5	14.4	1.4	64	76.7
MR04-87	1.6	64	1	12.4	1.4	50	141.5
M87	1.6	72	2	13.2	1.4	53	136.5
MR04-88	1	128	5	20.3	2.1	63	161
MR04-89	2	13	3	18.8	2.3	50	192
MR04-91	1.9	13	2	16.9	2	47	186
MR04-92	0.6	160	2	21.3	2.1	84	128
MR04-94	1.6	50	3	10	1	48	108.5
MR04-98	1	117	2	23.6	2.4	68	160
MR04-99	0.5	201	3	21.6	2.2	80	122.5
MR04-101	1	126	2	21.7	2	69	132
MM01	0.5	297	3	21	2	92	86.9
MM01a	0.5	318	1	19.6	2.1	95	81.5
MM01b	0.5	323	2	19.6	2.1	95	85.4
MM13	0.9	146	2	20.9	1.8	69	127
MM23	1	139	3	18.8	1.9	74	138
MM29	1.1	66	3	15.4	1.7	66	143.5
LC-19	2.3	14	2	21.6	2.4	45	206
BAS-1	<0.5	164	2	15.9	1.3	91	85.4
BAS-1a	<0.5	184	1	14.8	1.3	103	74.7
P-1	1.3	60	3	20.1	2.2	41	111.5
P-1a	1.2	77	2	18.4	2.3	47	110

APPENDIX D

ELEMENT MOBILITY DUE TO HYDROTHERMAL ALTERATION: DISCRIMINATING "FRESH" FROM "ALTERED" SAMPLES FROM THE SUITE OF VOLCANIC ROCKS AT EL DORADO

D.1 Introduction

The rock samples from the current study were chosen to best represent all levels of the volcanic stratigraphy and those showing the least signs of visible hydrothermal alteration were preferably selected. However, the mineralized volcanic basement rocks and some Pliocene volcanic rocks have experienced variable degrees of alteration, visible or cryptic, and many of these samples show geochemical patterns suggesting that some major and trace elements were mobile during alteration. During weathering or hydrothermal alteration, certain elements may be added or lost from the parent rock, hence changing the original rock composition (e.g., Price et al., 1991; Darce et al., 1991). The following section briefly describes the effect of hydrothermal alteration on element mobility, and discriminate "fresh" from "altered" samples. Any sample suspected to have experienced significant degrees of hydrothermal alteration and element gain or loss have been taken out of the suite of samples used in chapter 3 entitled "Geochemical evolution of Tertiary volcanic rocks along the developing plate margin of Central America: the El Dorado gold district, El Salvador".

D.2 Analytical methods, data and quality control

Thirty-nine rock samples representing all major stratigraphic levels were analyzed by X-ray fluorescence spectroscopy (XRF) and inductively coupled plasma mass spectrometry (ICP-MS) methods for major and trace elements at the ALS/Chemex laboratories, North Vancouver. The samples were crushed and pulverized by chrome steel plates and digested using a lithium metaborate fusion followed by dissolution in trace acid. To assess data quality, five rock samples were split into three to four aliquots and sent under different tag names to ALS/Chemex. Two aliquots of two MDRU standards, P-1 and BAS-1, a rhyolite and a basalt respectively, were also included. The analytical precision (expressed as a percentage standard deviation) typically ranges from 0.2% to ~10% for major oxides, ~1% to ~5% for LILE, and below 10-15% for HFSE and REE. The standard deviation for all elements calculated from replicate analyses is shown in Table 3.2 of chapter 3. The full geochemical data set for the thirty-nine rock samples and the seven replicate samples is included in the Appendix C.

The following exercise makes use of the full geochemical dataset. Different techniques have been used to discriminate samples that have experienced the effects of element mobility during hydrothermal alteration.

D.3 Hydrothermal alteration

Alteration patterns from the regional to mining district scale were established by Darce et al. (1989) in Nicaragua, and similar types of alteration are also observed at El Dorado. All mafic to intermediate volcanic basement rocks have experienced a regional burial diagenesis or low-grade zeolite facies metamorphism characterized by a chlorite/clay/zeolite mineral assemblage. At the district scale and in vein selvages, the rock is weakly to strongly chloritized with mixed clay minerals, calcite and pyrite. Sericite has been observed to replace plagioclase phenocrysts to variable degrees. Replacement of the rock groundmass by fine-grained adularia and quartz characterizes the most altered rocks.

D.3.1 Major oxides

The volcanic rocks at El Dorado are mainly calc-alkaline, bordering the high-K series, and range in composition from basaltic andesites to rhyolites (Figure D.1a & b). A striking feature observed on the K_2O vs. SiO_2 diagram is a strong departure of volcanic basement rocks (*Tma* and *Tap*) and some of the Cerro Caballo lava flow facies (*Tdf*) from the main calc-alkaline trend to high-K and even shoshonitic series (Figure D.2a). In this case, the altered samples appear to have gained potassium. This interpretation is supported by the positive (acid) staining of rock samples for K-feldspar and the presence of sericite replacing plagioclase phenocrysts and groundmass.

One more observation is the apparent lack of basaltic volcanic rocks as displayed on the total alkali vs. silica diagram (Figure D.1b). This effect is likely the result of normalizing hydrothermally altered or weathered rocks to an anhydrous composition. Many of the mafic rock samples contain up to 7.6 wt% volatiles-LOI (e.g., sample MR04-63; see Figure D.3b), possibly due to the presence of chlorite, calcite and clays as alteration minerals. When normalizing to an anhydrous composition, this causes a significant shift of the geochemical analyses to higher SiO_2 and alkali content, hence the

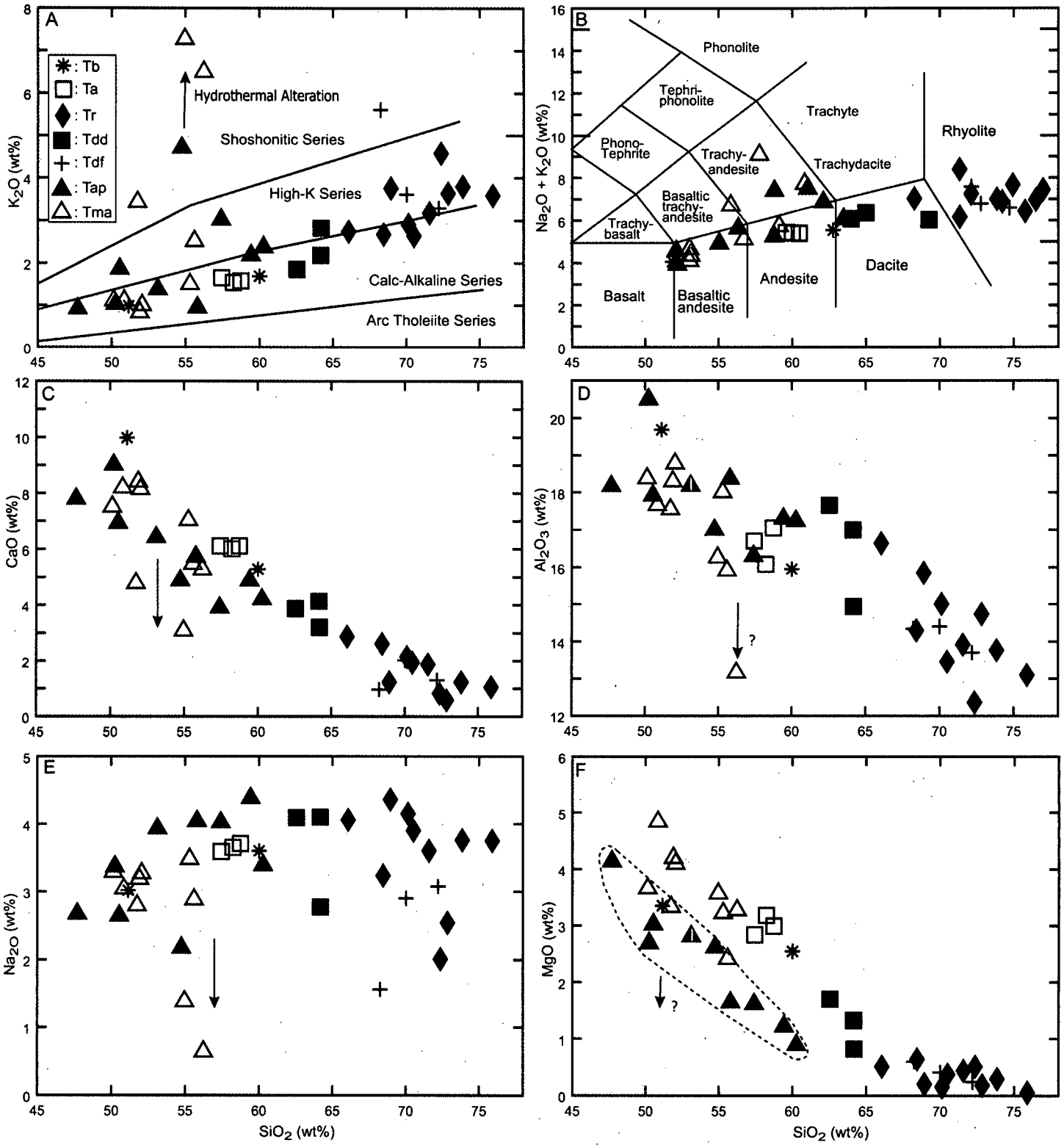

Figure D.1. Bivariate plots of major oxides for the suites of rocks of the El Dorado district. A) Potassium vs. silica displaying the rock type divisions after Peccerillo and Taylor (1976). B) Alkali vs. silica diagram (TAS) from LeBas et al. (1986) using data normalized to 100% on a volatile-free basis. C) through F) Calcium, auminum, magnesium and sodium oxides vs. silica respectively. The arrows point the effect of hydrothermal alteration on rock geochemistry, mainly observed on basement rock samples (triangles). Symbols: Tma = lower basement lava sequence; Tap = basement porphyritic dikes and domes; Tdf = Cerro Caballo lava flow facies; Tdd = Cerro Caballo dome facies; Tr = rhyolite domes, flows and tuffs; Ta = post-mineral (?) platy andesites; Tb = post-mineral lava flows. A 1-sigma analytical uncertainty is smaller than the symbols size on all diagrams.

apparent lack of basaltic rocks. Based on mineralogy and color index, some rocks are still referred to as basalts despite their classification as basaltic andesites on the TAS diagram.

Bivariate plots c) though f) on Figure D.1 display the major oxides trends of calcium, aluminum, sodium and magnesium oxides vs. SiO_2 as a measure of differentiation. Volcanic basement rock samples show variable degree of departure from the main trends for calcium and sodium, and to a lesser extent aluminum and magnesium. In the case of MgO, the porphyritic domes and dikes of the volcanic basement systematically plot at lower values relative to other mafic to intermediate volcanic rocks. This trend is observed among fresh rocks and must therefore reflect a different magmatic fractionation trend for this genetically related group of rocks (see chapter 3).

D.3.2 Trace elements

Three large ion lithophile elements (Ba, Rb and Sr) were plotted against SiO_2 (Figure D.2a, b and c respectively). Barium and Rubidium (Figure D.2a and b) show similar trends, with progressive enrichment from mafic to felsic rocks. Volcanic basement rock samples again show some degree of departure from the main trend, in both cases to higher Ba and Rb concentrations. Strontium shows a negative relationship against SiO_2, and volcanic basement rock samples show a clear depletion in Sr relative to the main trend. A plot of Rb vs. Sr further illustrates the effect of element mobility (Figure D.2d). A well constrained negative trend is observed from felsic to mafic samples. Anomalous volcanic basement rock samples and lava flows associated with the Cerro Caballo dome complex (+ sign) plot well above that trend. The most altered samples have the greatest enrichment in Rb and a depletion in Sr.

On a K_2O vs. Rb/K_2O diagram (Figure D.3a), the alteration space is again defined by a group of volcanic basement rock samples and rocks of the Cerro Caballo dome and flow complex. The altered samples, outlined by the dashed, line fall well outside the trend defined by most mafic to felsic volcanic rocks. The five most altered samples in Rb vs. Sr space (outlined by the dashed line) also represent the most altered samples in K_2O vs. Rb/K_2O space (compare with Figure D.2d). The same samples have some of the lowest Na_2O and CaO concentrations (Figure D.2c and e).

Many of the altered rock samples on figure D.3a show an enrichment in volatiles (probably mainly H_2O and CO_2) as seen by their LOI content (Figure D.3b). Curiously, a

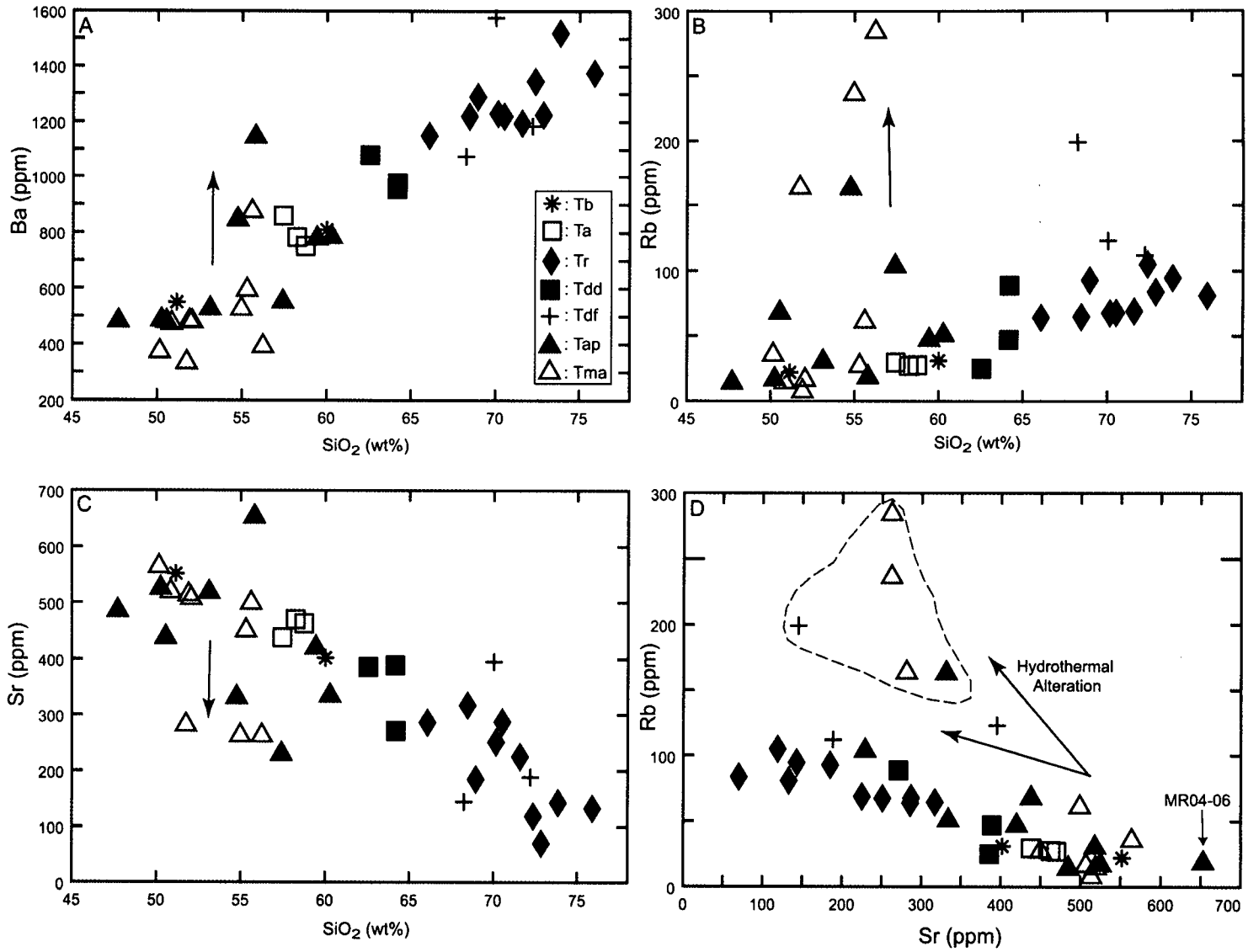

Figure D.2. Large ion lithophile elements vs. SiO_2 A) and B) Barium and rubidium respectively showing similar patterns with progressive enrichement with increasing silica content. The effect of hydrothermal alteration is observed on both diagrams with basement rocks samples strongly departing from the main trend, especially Rb. C) Strontium vs. silica showing a negative relationship. Altered basement rock samples show a clear depletion with respect to the main trend. D) Rb vs. Sr (ppm) showing the effect of hydrothermal alteration on the concentration of these trace elements. The most altered samples (outlined by the dashed line) show the greatest Rb enrichment and Sr depletion. Sample MR04-06, an apparently unaltered basement rock sample shows a contrasting type of alteration not discerned on those trace element plots (see next figures). See figure D.1 for symbols explanation. A 1-sigma analytical uncertainty is smaller than the symbols size on all diagrams.

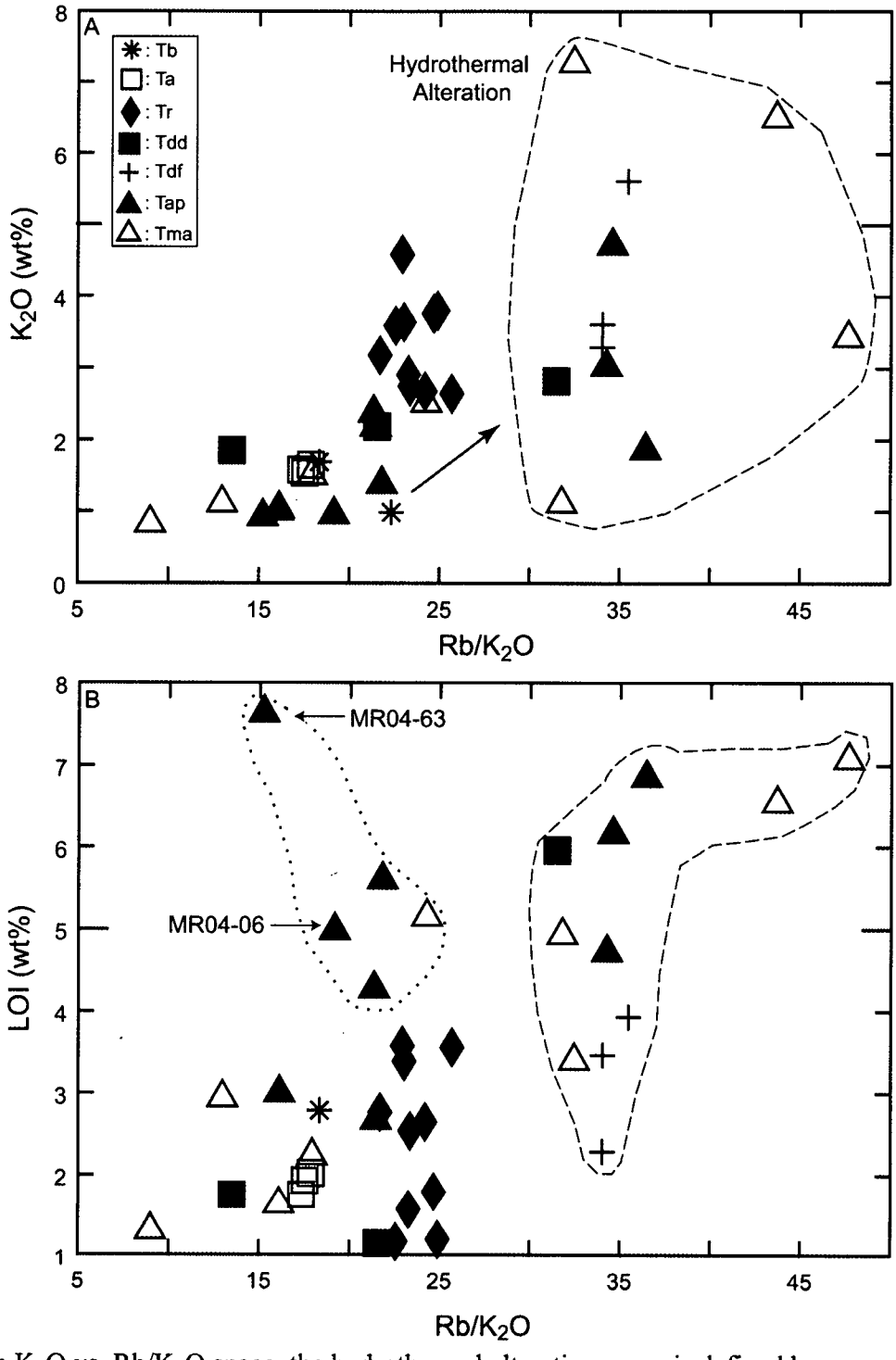

Figure D.3. A) In K_2O vs. Rb/K_2O space, the hydrothermal alteration space is defined by a group of outlying basement rock samples and samples from the Cerro Caballo dome and flow complex. B) The LOI (wt%) content of the El Dorado rocks ploted agaisnt Rb/K_2O (same axis as in A). Some rocks identified as fresh in A have unusually high LOI contents as outlined by the dotted line. Sample MR04-06 represents one of those samples. On the previous diagram (Rb vs. Sr.; Figure D.2d), this sample shows no sign of departure from the main trend. Those samples represent a different type of alteration than the first suite identified on A and B (dashed line). See figure D.1 for symbols explanation. A 1-sigma analytical uncertainty is smaller than the symbols size on all diagrams.

sub-set of five basement rock samples that fall within the "unaltered" field in K_2O vs. Rb/K_2O space, have anomalous contents of volatiles as outlined by the dotted line on Figure D.3b (compare with Figure D.3a). Some of those samples (e.g. MR04-06) show no sign of hydrothermal alteration when plotted on a Rb vs. Sr diagram (Figure D.2d). Rock sample MR04-06 contains abundant chlorite replacing pyroxene phenocrysts, and little sericite replacing plagioclase phenocrysts (see Appendix B). Chloritization can be a simple hydration process that may occur with no cation exchange (G. Dipple, pers. comm., 2006). This could explain the anomalously high LOI content, but the alteration did not disturb the major and trace elements concentrations.

The rare earth elements are the least soluble trace elements, and are generally considered immobile, even in slightly altered rocks (Rollinson, 1993). In some cases of weathering or hydrothermally alteration, however, rare-earth elements have been demonstrated to be mobile (e.g. Price et al., 1991). LREE, especially lanthanum, are the most likely to be affected by alteration and mobility generally decreases towards the HREE (Gifkins et al., 2005). This may cause a positive or negative shift in LREE concentrations. In some cases of alteration, the slope of the REE patterns are retained, but changes are recorded in the magnitude of the y-axis, with elevated patterns representing mass loss and depression of the pattern mass gain (Gifkins, 2005). This effect could potentially be represented by a volcanic basement rock sample on Figure D.4b. The upper-most pattern, representing a chlorite-sericite-clay altered porphyritic andesite dike, has a REE pattern sub-parallel to most samples within its group, but it has elevated abundances with respect to other samples (70x chondrite versus 30x-50x for most samples). This sample was amongst the most altered rocks on all previous diagrams (Figure D.1-D.3). The altered lava flow samples from the Cerro Caballo dome complex (Figure D.4c), shows an enrichment in LREE relative to the volcanic basement rocks (see shaded area for reference). Most felsic rock samples (Figure D.4d) also show this positive LREE pattern. This enrichment pattern however probably represents the effect of magmatic fractionation (see chapter 3).

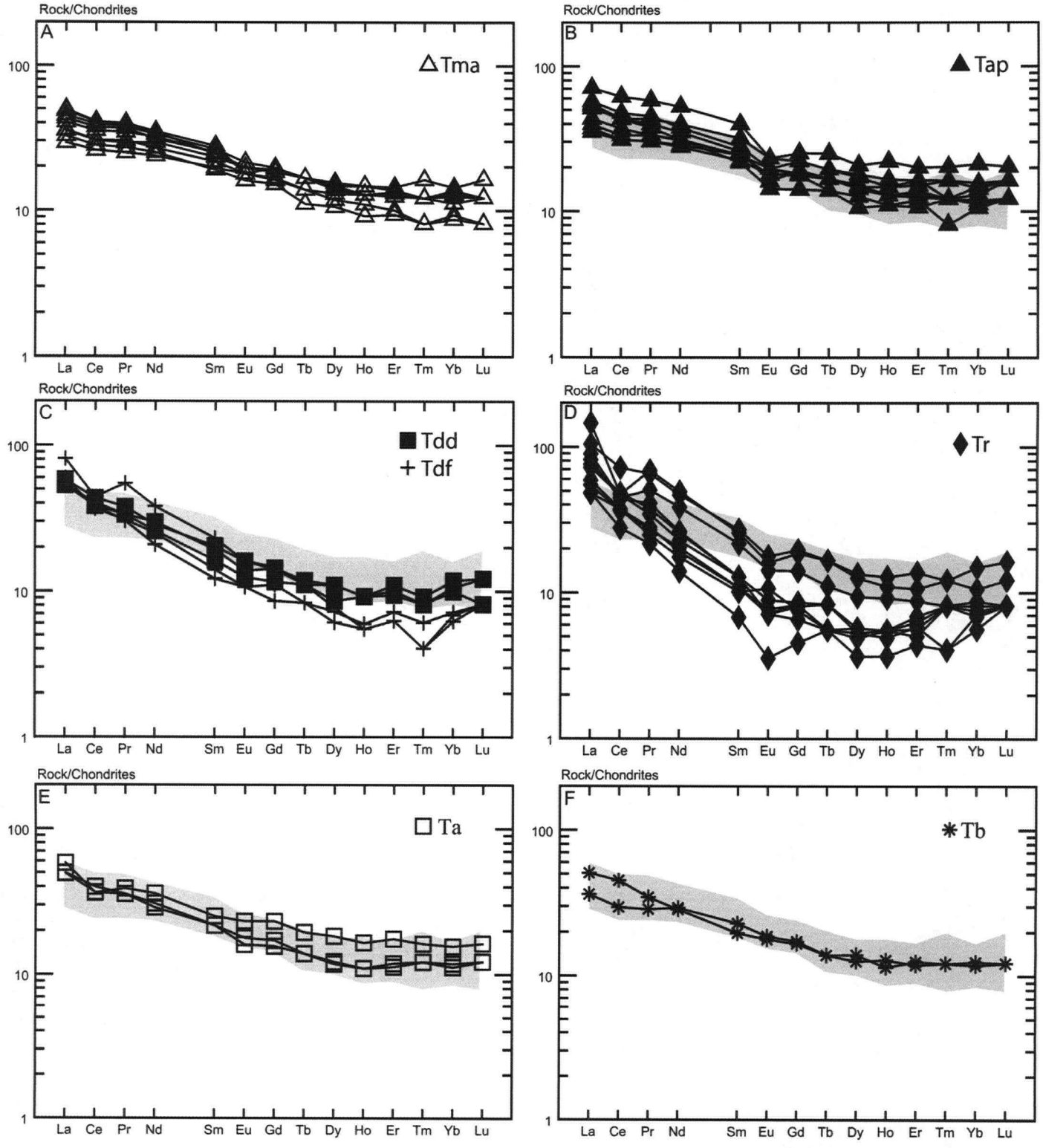

Figure D.4. Rare earth element patterns normalized to chondritic values from McDonough and Sun (1995). A) Lower mafic to intermediate lava sequence; B) Mafic to intermediate porphyritic domes and dikes; C) Cerro Caballo dome and flow complex; D) Rhyolite domes, dikes, lava flows, and tuffs. E) Platy andesite lava flows; F) Basaltic lava flows. The grey shaded area outlines on diagram B) to F) the pattern produced by the lower lava sequence (Tma) on diagram A). Rocks of the Cerro Caballo dome and flow complex show a slight LREE enrichment and MREE depletion relative to Tma samples. Rhyolitic units on diagram D) show a marked enrichment in LREE and a depletion in MREE. Post-mineral andesitic and basaltic lava flows shown on diagram E) and F) show identical patterns to the mafic to intermediate lava flows forming the basement rocks.

D.3.3 Alteration Indices

Alteration indices are useful and visual ways to reflect multi-component geochemical changes within suites of volcanic rocks. The Ishikawa Alteration Index (AI; Ishikawa et al., 1976), and the chlorite-pyrite-carbonate index (CCPI; Large et al., 2001) have been designed to describe the intensity of chlorite-sericite and chlorite-carbonate-pyrite alteration in rocks from different volcanic-hosted massive sulfide deposits.

$$AI = \frac{100\,(MgO + K_2O)}{MgO + K_2O + CaO + Na_2O} \qquad CCPI = \frac{100\,(FeO + MgO)}{FeO + MgO + Na_2O + K_2O}$$

The AI is useful to characterize plagioclase-destructive alteration and is more widely used with felsic rocks (Gifkins, 2005). The CCPI is useful since it considers the addition of calcite and Fe-Mg carbonate, common in many alteration assemblages, but has limitations with mafic rocks, since they inherently have higher FeO and MgO contents (Gifkins, 2005). The suite of rocks from El Dorado was plotted in an alteration box-plot (Figure D.5), which uses both AI and CCPI to identify alteration trends (Large et al., 2001). Most rock samples plot within the least-altered field represented by the box. Four volcanic basement rock samples depart from the cluster of samples defining a trend toward a combination of the sericite and chlorite vectors (Figure D.5a). The same samples show the greatest enrichment in K_2O vs. Rb/K_2O and form part of the alteration space on the Rb vs. Sr diagram (Figure D.2d; Figure D.3a).

Some felsic samples (+ sign and diamond) plot outside of the least-altered box, and could include a combination of the sericite and K-feldspar alteration vectors. The lava flow sample from the Cerro Caballo dome complex has anomalously high contents of K_2O and low Na_2O (Figure D.1a, e). This sample also shows the greatest enrichment in Rb and depletion in Sr relative to the other Cerro Caballo dome and lava samples (Figure D.2d).

The chloritized sample MR04-06 with anomalous volatile content (see above; figure D.3b) shows no indication of a chlorite vector when plotted on the box-plot (Figure D.5). Again this shows how chloritization can be a simple hydration process with no sign of cation exchange. This situation shows the limitation of using one alteration discriminant alone (e.g., the box-plot), where altered samples could go undetected.

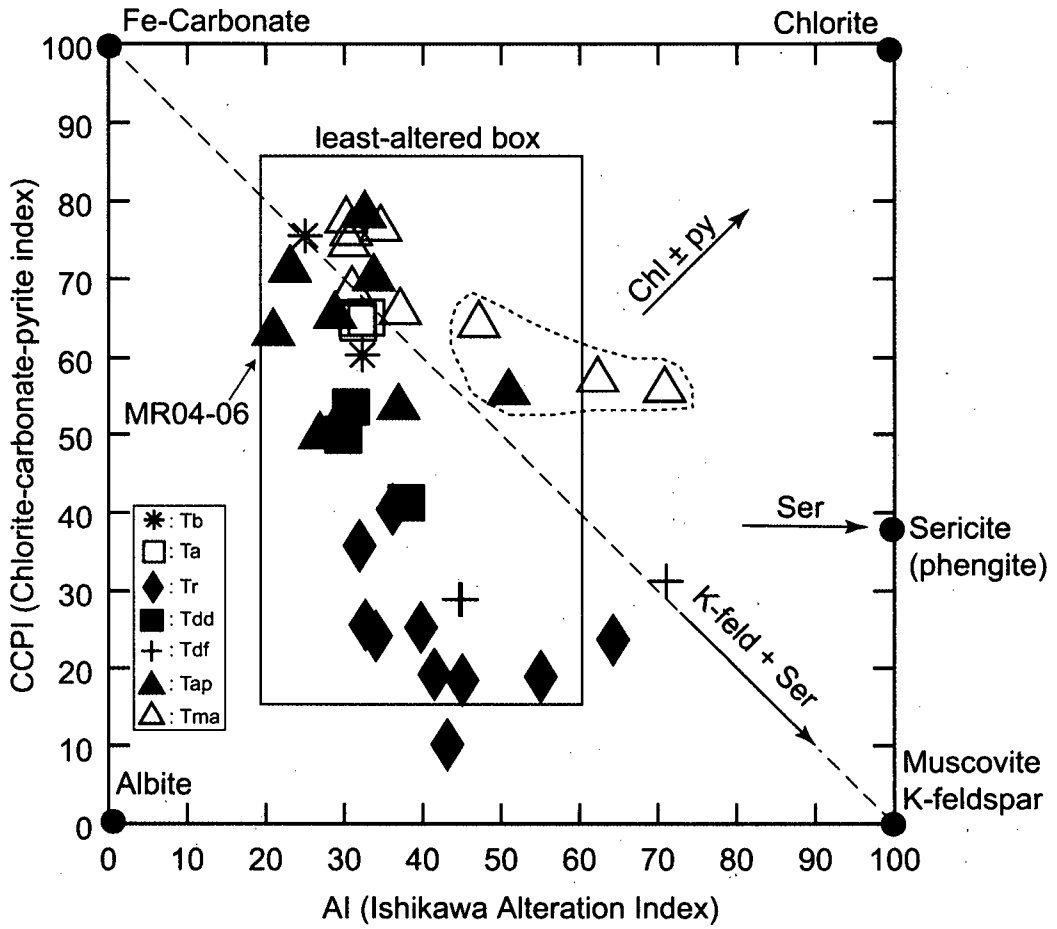

Figure D.5. Alteration box-plot of Large et al. (2001) modified from Gifkins (2005). The box-plot uses the Ishikawa Alteration Index on the y-axis and the chlorite-carbonate-pyrite index on the x-axis. The suite of rocks from El Dorado show a mixed influence from the chlorite, sericite and K-feldspar alteration vectors. Those alteration patterns agree with the observed trends on figures D.1-D.3. See figure D.1 for symbols explanation. A 1-sigma analytical uncertainty is smaller than the symbols size.

D.3.4 The isocon method

The isocon diagram is a useful and simple method to assess element mobility in a genetically related suite of altered rocks (Grant, 1986). The technique requires a parent sample, representing the unaltered composition of a rock unit, and is plotted against other rocks of the same unit. Elements that are immobile will plot on a 1:1 reference line (ideally), whereas elements that were either added or lost during metasomatic alteration will plot above or below that line respectively. In the case of the suite of rocks from El Dorado, since all rock samples represent individual rock units (e.g. lava flows or intrusive bodies), the parent composition was approximated by the average composition of two of the least altered mafic samples (MR04-62, and MM01). A suite of apparently "altered" basement rock samples were then plotted against the hypothetical parent (Figure D.6). SiO_2 and Al_2O_3 were scaled by factors of 1/16 and 1/2 respectively in order to increase the resolution of the diagram. Although the effect of primary geochemical variations between rock samples cannot be discarded, certain elements show unusual variations relative to the hypothetical parent rock (Figure D.6). For all rock samples, TiO_2 and SiO_2 form clusters of data close to the 1:1 reference dashed line, and are therefore considered immobile. On the other hand, K_2O and LOI plot well above the line, and the other major oxides below the line. This observation suggests that K and LOI were added during hydrothermal alteration, while Na, Ca, Mg, Fe and to a lesser extent Al, were possibly lost to variable degrees. As seen previously, in the case of MgO the apparent loss could be a primary magmatic characteristic of some of the volcanic basement rocks (see Figure D.1f).

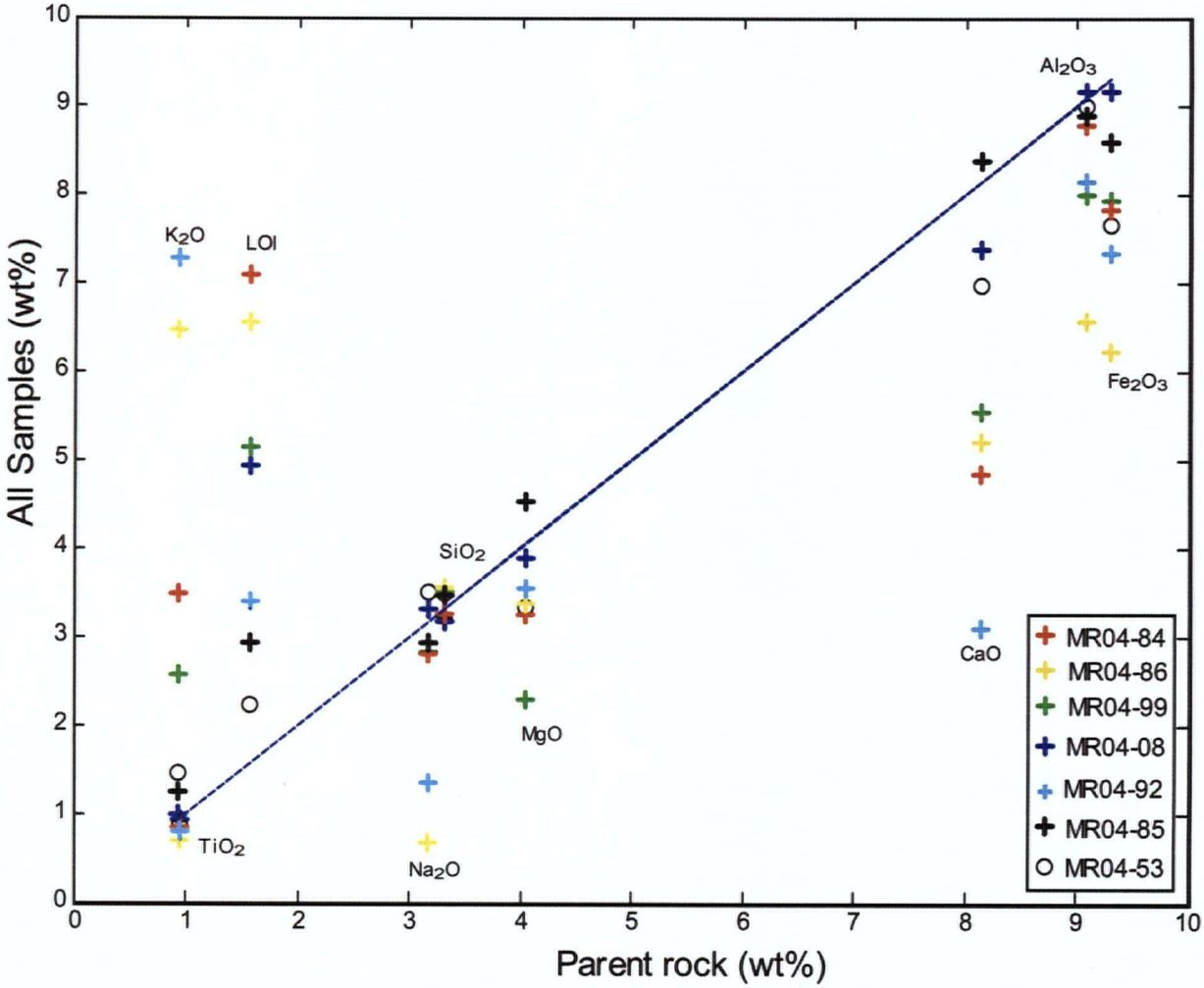

Figure D.6. Isocon diagram (Grant, 1986) of selected mafic basement rocks (Tma) of the El Dorado district plotted against an hypothetical "unaltered" parent rock (average of MM01 and MR04-62). From this diagram, immobile elements include Si, and Ti clustering around the 1:1 reference line of no net change for all samples. K and LOI were gained whereas Na, Ca, Al, Mg, and Fe were possibly lost to variable extent. Silica and aluminum concentrations have been scaled by factors of 0.0625 and 0.5 respectively in order to fit them on the diagram.

D.3.5 TiO_2—Zr plot

One last example to test element mobility is the TiO_2 vs. Zr plot used by Barrett and MacLean (1994) (Figure D.7). Zirconium is an incompatible elements while Ti behaves compatibly in rocks with composition more evolved than basaltic andesite, thus defining a negative correlation referred to as the magmatic "fractionation curve" (Gifkins, 2005). Fresh volcanic rocks should plot along the fractionation curve, while altered rocks depart from the magmatic trend along alteration lines that project towards the origin. Rocks that plot on the origin side of the magmatic fractionation curve represent net mass gain during alteration, and those that plot above the curve represent net mass loss (Gifkins, 2005). The El Dorado volcanic rocks show the limitations associated with this type of diagram with calc-alkaline suites (Figure D.7). Most samples plot below the fractionation curve although this could be an effect of primary composition, with samples having relatively low Ti and Zr content. The felsic samples however show a strong departure from the magmatic fractionation path, and project towards the origin along an alteration line. Based on this criteria, one could easily classify all felsic rocks at El Dorado as "altered". When taking a closer look at the zirconium content of the suite of rocks (Figure D.8), one realizes that the zirconium of mafic rocks increases with increasing SiO_2 up to dacitic composition at which point the trend becomes negative and the zirconium content of the most felsic samples drops to values similar to the most mafic rocks (~75 ppm). This trend, also supported by REE patterns, appears consistent with hornblende and zircon fractionation (see chapter 3). This example shows again the importance of using appropriate tools to identify mobile elements during alteration.

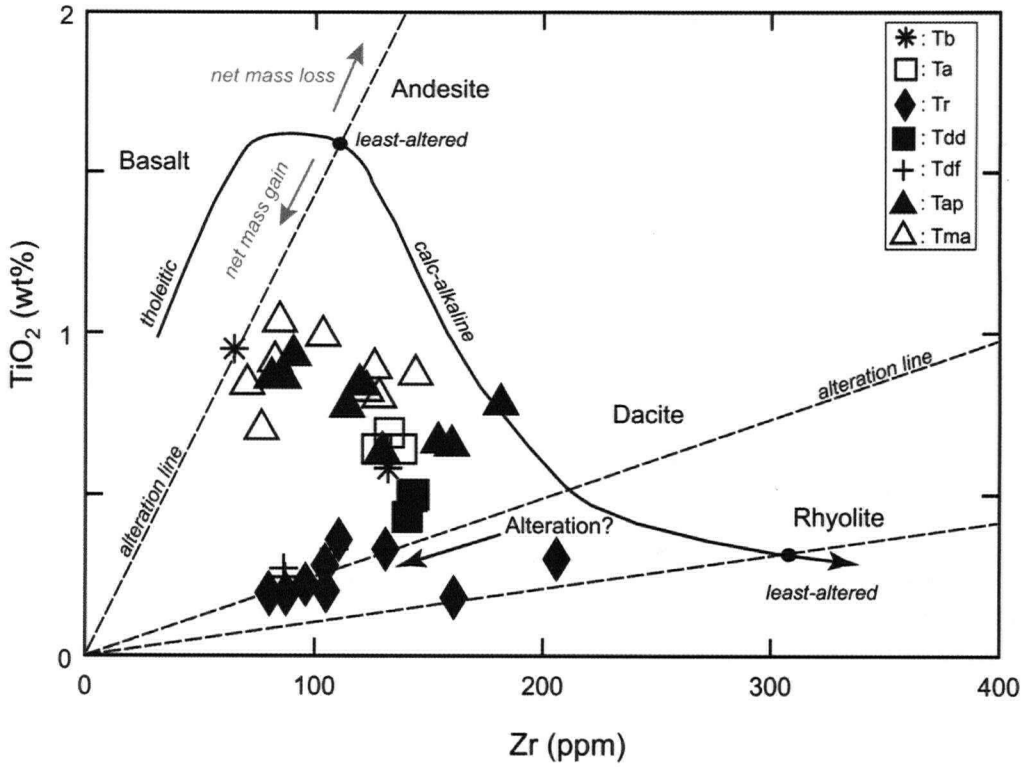

Figure D.7. TiO2 vs. Zr (ppm) plot modified from Gifkins et al., (2005) (after Barrett and MacLean (1994). Fresh volcanic rocks define a magmatic "fractionation curve" and altered rocks plot along alteration lines projecting towards the origin (Gifkins, 2005). See figure D.1 for symbols explanation. A 1-sigma analytical uncertainty is smaller than the symbols size.

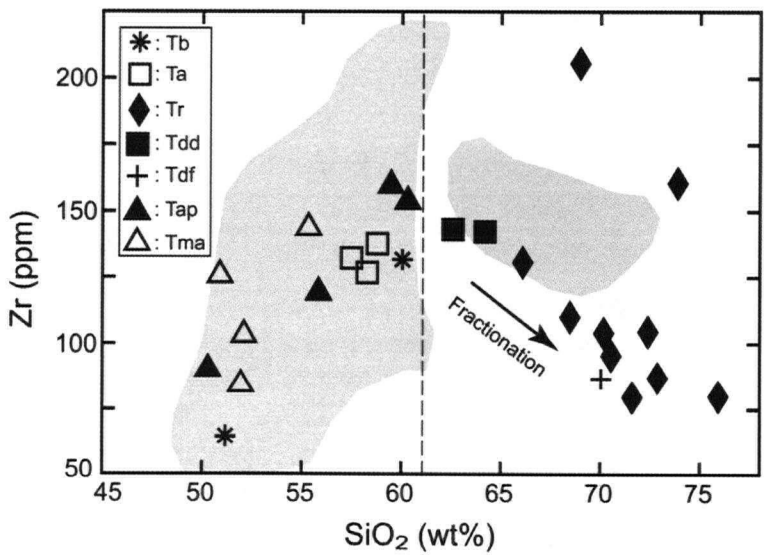

Figure D.8. Zr (ppm) vs. SiO_2 (wt%) for the El Dorado volcanic rocks and Quaternary lavas and tephras from the Central American volcanic arc. The observed trend appears consistent with magmatic fractionation with samples more evolved than dacitic composition defining a negative correlation. Felsic samples are glassy rhyolites that do not show signs of hydrothermal alteration. See figure D.1 for symbols explanation. A 1-sigma analytical uncertainty is smaller than the symbols size.

D.4 Summary

Combining all observations and anomalous trends on Figure D.1-D.6, a suite of altered rocks was identified. Those include ten volcanic basement rock samples (MR04-03, MR04-99, MR04-08, MR04-09, MR04-10, MR04-86, MR04-84, MR04-63, MR04-70, and MR04-92), and samples from the Cerro Caballo dome and flow complex (solid squares and plus signs; MR04-94, MR04-75, MR04-79 and MR04-76). These samples were removed for the purpose of chapter 3, with the exception of sample MR04-79. This sample has been included as the "least altered" in order to represent the outflow facies associated with the Cerro Caballo dome complex.

To summarize, silica and titanium appear to have been immobile during hydrothermal alteration. Major elements that appear to have been gained during hydrothermal alteration are volatiles (LOI, probably mainly H_2O and CO_2), potassium, and rubidium. Elements that were lost include sodium, calcium, and strontium to variable extents, and arguably aluminum, magnesium, and iron. The mobility of these elements is interpreted to be mainly controlled by the sericitization of groundmass plagioclase and phenocrysts, by the replacement of pyroxene phenocrysts and groundmass by chlorite and/or mixed clays, and by K-feldspar (adularia) and quartz replacement in the more extreme cases, as revealed by petrography. Chloritization is a common alteration product at El Dorado, but is not necessarily associated with element mobility as revealed by the geochemistry of sample MR04-06.

D.5 References

Barrett, T.J., and MacLean, W.H., 1994, Chemostratigraphy and hydrothermal alteration in exploration for VHMS deposits in greenstone and younger volcanic rocks, *in* Lentz, D.R., ed., Alteration and alteration processes associated with ore forming systems, Geological Society of Canada short course notes, v. 11, p. 433-467.

Darce, M., Levi, B., Nystrom, J.O., and Troeng, B., 1989, Alteration patterns in volcanic rocks within an east-west traverse through central Nicaragua, J. of South Am. Earth Sc., vol. 2, p. 155-161.

Darce, M. Levi, B., and Nystrom, J.O., 1991, Chemical changes during alteration of volcanic rocks and gold ore formation, La Libertad, Nicaragua, J. of South Am. Earth Sc., vol. 4, no. 1-2, p. 87-97.

Gifkins, C., Herrmann, W., and Large, R, 2005, Altered Volcanic Rocks: a guide to description and interpretation, CODES special publications, pp.

Grant, J.A., 1986, The Isocon Diagram: A Simple Solution to Gressen's Equation for Metasomatic Alteration, Economic Geology, vol. 81, p. 1976-1982.

Ishikawa, Y., Sawaguchi, T., Iwaya, S., and Horiuchi, M., 1976, Delineation of prospecting targets for Kuroko deposits based on modes of volcanism of underlying dacite and alteration halos, Mining Geology, v. 26, p.105-117.

Large, R.R., Gemmell, J.B., and Paulick, H., 2001, The Alteration box plot – a simple approach to understanding the relationship between alteration mineralogy and lithogeochemistry associated with volcanic-hosted massive sulfide deposits, Economic Geology, v. 96, p. 1055-1072.

Le Bas, M .J., Le Maitre, R .W., Streckeisen, A., and Zanettin, B.A., 1986, Chemical classification of volcanic rocks based on the total alkali-silica diagram, Journal of Petrology, vol. 27, no. 3, p.745-750.

McDonough, W.F. and Sun, S.-s., 1995, Composition of the Earth. Chemical Geology, vol.120, p.223-253.

Peccerillo, A., and Taylor, S.R., 1976, Geochemistry of Eocene calc-alkaline volcanic rocks from the Kastamonu area, northern Turkey, Contributions to Mineralogy and Petrology, vol. 58, no. 1, p.63-81.

Price, R.C., Gray, C.M., Wilson, R.E., Frey, F.A., and Taylor, S.R., 1991, The effect of weathering on rare-earth element, Y, and Ba abundances in Tertiary basalts from southeastern Australia, Chemical Geology, vol. 93, p. 245-265.

Rollinson, H., 1993, Using geochemical data: evaluation, presentation, interpretation. Longman group UK limited, 352 pp.